

The structure of detonation waves in supernovae revisited

Doron Kushnir¹★

¹*Dept. of Particle Phys. & Astrophys., Weizmann Institute of Science, Rehovot 76100, Israel*

Accepted XXX. Received YYY; in original form ZZZ

ABSTRACT

The structure of a thermonuclear detonation wave can be solved accurately and, thus, may serve as a testbed for studying different approximations that are included in multi-dimensional hydrodynamical simulations of supernova. We present the structure of thermonuclear detonations for the equal mass fraction of ^{12}C and ^{16}O (CO) and for pure ^4He (He) over a wide range of upstream plasma conditions. The lists of isotopes we constructed allow us to determine the detonation speeds, as well as the final states for these detonations, with an uncertainty of the percent level (obtained here for the first time). We provide our results with a numerical accuracy of $\sim 0.1\%$, which provides an efficient benchmark for future studies.

We further show that CO detonations are pathological for all upstream density values, which differs from previous studies, which concluded that for low upstream densities CO detonations are of the Chapman-Jouget (CJ) type. We postulate that these claims were probably due to low numerical accuracy. We provide an approximate condition, independent of reaction rates, that allows to estimate whether arbitrary upstream values will support a detonation wave of the CJ type. Using this argument, we are able to show that CO detonations are pathological and to verify that He detonations are of the CJ type, as was previously claimed for He. Our analysis of the reactions that control the approach to nuclear statistical equilibrium, which determines the length scale of this stage, reveals that at high densities, the reactions $^{11}\text{B}+p \leftrightarrow ^3\text{He}$ plays a significant role, which was previously unknown. We also demonstrate that the study of thermonuclear detonation waves is very efficient in exposing numerical bugs, and report on dozens of numerical bugs in the *Helmholtz* equation of state and in the MESA code, some of them quite severe.

Key words: hydrodynamics – shock waves – supernovae: general

1 INTRODUCTION

Thermonuclear detonation waves are believed to play a key role in supernovae (Hoyle & Fowler 1960; Fowler & Hoyle 1964). The detonation wave structure is important for the energy release and for the nucleosynthesis during the explosion, and it is therefore a crucial ingredient for supernovae modelling (see Seitenzahl & Townsley 2017, for a recent review). However, resolving the detonation wave structure in a multi-dimensional hydrodynamical simulation of a supernova is currently impossible. This is because the fast thermonuclear burning dictates a burning length scale that is much smaller than the size of the star, and because the number of isotopes participating in the thermonuclear burning is very large. These problems led to the introduction of various approximations that allow multi-dimensional hydrodynamical simulations of full stars. The error introduced by these approximations, however, is not well understood. Most notably, a small number (10 – 20) of isotopes is usually included in the multi-dimensional hydrodynamical simulations, and the method for choosing these isotopes has not yet been firmly established.

A relevant, much simpler, problem to analyze is the structure of a steady-state, planar detonation wave, given by the ZND theory (Zel'Dovich 1940; von Neumann 1947; Döring 1943), on which we concentrate in this work. This problem can be solved accurately for the case of a thermonuclear detonation wave, and thus can serve as a testbed for studying different approximations that are included in multi-dimensional hydrodynamical simulations. For example, we can calibrate lists of isotopes that allow the calculation of a thermonuclear detonation wave with some prescribed accuracy. We assume that the reader is familiar with the basic physics of thermonuclear detonation waves, as this topic has been heavily discussed over the past several decades. The theory of detonation waves in general is described in the text book of Fickett & Davis (1979) and the fundamental physics of thermonuclear detonation waves is discussed by Khokhlov (1989, although it contains some errors and inaccuracies that are discussed in detail below).

We consider two compositions for the upstream plasma that show dramatic differences in the structure of the detonation wave and are both relevant for supernova modelling. The first one is the equal mass fraction of ^{12}C and ^{16}O (CO) and the second is pure ^4He (He). Other variants of the initial composition can be handled with the same tools described in this work.

★ E-mail: doron.kushnir@weizmann.ac.il

The structure of steady-state, planar, thermonuclear detonation waves has been studied by numerous authors. [Imshennik & Khokhlov \(1984\)](#) studied detonation waves in pure ^{12}C , [Khokhlov \(1989\)](#) studied detonation waves in CO and He, and [Townesley et al. \(2016\)](#) presented solutions for detonation waves in CO (with a small initial mass fraction of ^{20}Ne). Other studies employed a simplified reaction network (usually an α -net composed of 13 isotopes) to calculate steady-state, planar detonation waves in different mixtures ([Bruenn & Marroquin 1975](#); [Sharpe 1999](#); [Gamezo et al. 1999](#); [Dursi & Timmes 2006](#); [Noël et al. 2007](#); [Domínguez & Khokhlov 2011](#); [Townesley et al. 2012](#); [Dunkley et al. 2013](#)). Since the final state of thermonuclear detonation waves can be dominated by isotopes that are not α -elements, the uncertainty with using α -net can be significant. [Sharpe \(1999\)](#) studied detonation waves in CO with a specific emphasis on a method to traverse the pathological point. This method builds on a numerical extrapolation with a claimed degree of accuracy of $\sim 10^{-15}$, which seems unrealistic (see discussion below).

One of our objective here is to calculate Chapman-Jouget (CJ) detonations with an uncertainty in the order of the percent level over a wide range of upstream plasma conditions that are relevant for supernovae. The parameters of CJ detonations have been already calculated for CO ([Bruenn 1971](#); [Khokhlov 1988](#)) and for He ([Mazurek 1973b](#); [Khokhlov 1988](#)). By comparing our results to those of previous works, we demonstrate that we are the first to reach an uncertainty level of one percent. In fact, we show that the equation of state (EOS) used of [Mazurek \(1973b\)](#) is not accurate enough, and that [Khokhlov \(1988\)](#) used an erroneous EOS. [Timmes & Niemeyer \(2000\)](#) calculated a few properties for CJ detonations in He, and they claim to agree with the results obtained by [Mazurek \(1973b\)](#) and [Khokhlov \(1988\)](#). It is somewhat confusing, as the results obtained by [Mazurek \(1973b\)](#) and [Khokhlov \(1988\)](#) are both erroneous, and in different ways. [Timmes & Niemeyer \(2000\)](#) does not provide the required information to reproduce their results.

We further calculate the structure of the detonation waves for both CO and He. Our determination of the pathological detonation speed for CO, as well as the final state of these detonations, is with a level of uncertainty of the percent level. We show that previous studies of the detonation wave structure with a detailed reaction network for both CO ([Khokhlov 1989](#); [Townesley et al. 2016](#)) and for He ([Khokhlov 1989](#)) are less accurate. Our results for the detonation wave speeds and for the final states are reported with a numerical accuracy of $\sim 0.1\%$, representing an efficient benchmark for future studies. We provide all the relevant information needed to fully reproduce our results.

Besides providing accurate results and highlighting a few errors and inaccuracies in previous works, we present here a few new insights into the structure of thermonuclear detonation waves. We show that CO detonations are pathological for all upstream densities values, as far as our numerical accuracy allows us to test this. This is different from previous studies ([Imshennik & Khokhlov 1984](#); [Khokhlov 1989](#); [Sharpe 1999](#); [Gamezo et al. 1999](#); [Dunkley et al. 2013](#)), which concluded that for low upstream densities, CO detonations are of the CJ type. We explain why these claims were probably due to low numerical accuracy. We provide an approximate condition, independent of reaction rates, that allows to estimate whether arbitrary upstream values (including composition) will support a detonation of the CJ type. Using this argument, we are able to show that CO detonations are pathological for all upstream densities and to verify that

He detonations are of the CJ type, as was previously claimed for He ([Khokhlov 1989](#)). We show that in the case of CO detonations, the sonic point changes position in a discontinuous manner from $x \sim 100$ cm to $x \sim 10^4$ cm around the upstream density of $\approx 2.7 \times 10^7$ g cm $^{-3}$ (This behaviour has already been observed, but was misinterpreted, [Dunkley et al. 2013](#)).

The calculations in this work were performed with a modified version of the MESA code¹ ([Paxton et al. 2011, 2013, 2015](#)). We find that the study of thermonuclear detonation waves is a very efficient method for exposing numerical bugs. We report here dozens of such numerical bugs, some of them quite severe.

The definition of the problem to be solved is described in Section 2. The required input physics for an accurate calculation of the detonation wave structure is described in Section 3. We study CJ detonations in Section 4 and the full structure of the detonation waves in Section 5. We discuss the approximate condition needed in order to estimate whether arbitrary upstream values will support a detonation of the CJ type in Section 6 and the role of weak reactions in Section 7. We summarise our results in Section 8. The numerical bugs that we found are reported in Appendices B and C.

2 DEFINITION OF THE PROBLEM

The structure of a detonation wave can be found by integration, where the initial conditions are the downstream values of the leading shock. We assume that the pressure, P , and the internal energy per unit mass, ε , are given as a function of the independent variables: density, ρ , temperature, T , and the mass fraction of the isotopes, X_i ($\sum_i X_i = 1$ and, unless stated otherwise, the sum goes over all isotopes). For planar, steady-state, non-relativistic hydrodynamics, the equations to integrate are:

$$\begin{aligned} d\rho &= \frac{\frac{\partial P}{\partial T} \left(\frac{\partial \varepsilon}{\partial T} \right)^{-1} \left(dq - \sum_i \frac{\partial \varepsilon}{\partial X_i} dX_i \right) + \sum_i \frac{\partial P}{\partial X_i} dX_i}{u^2 - c_s^2}, \\ dT &= \left(\frac{\partial P}{\partial T} \right)^{-1} \left[\left(u^2 - \frac{\partial P}{\partial \rho} \right) d\rho - \sum_i \frac{\partial P}{\partial X_i} dX_i \right], \end{aligned} \quad (1)$$

where c_s is the frozen (constant composition), non-relativistic speed of sound, u is the velocity in the shock rest frame

$$u = \frac{\rho_0}{\rho} D, \quad (2)$$

ρ_0 is the upstream density, D is the shock velocity in the lab frame, q is the nuclear energy release:

$$q = N_A \sum_i Q_i Y_i, \quad (3)$$

Q_i are the binding energies of the nuclei, $Y_i \approx X_i/A_i$ are the molar fractions of the nuclei (see discussion in Section 2.1), A_i are the nucleon numbers and N_A is Avogadro's number. Upstream values will be denoted with subscript 0, CJ values with subscript CJ and pathological values with subscript *. We further define the equilibrium speed of sound, c_s^e . Unless stated otherwise, the partial derivatives are taken with the rest of the independent variables remaining constant. [Sharpe \(1999\)](#) pointed out that since $\sum_i X_i = 1$, not all X_i are independent, and he consequently eliminated from the integration the mass fraction of one isotope and instead determined it from $\sum_i X_i = 1$. In this paper, we choose to treat all X_i as independent

¹ version r7624; <https://sourceforge.net/projects/mesa/files/releases/>

variables, while using $\sum_i X_i = 1$ only for the initial conditions. This approach is valid, since the equations that determine dX_i must satisfy $\sum_i dX_i = 0$, leading to $\sum_i X_i = 1$ throughout the integration, up to a numerical error that can be controlled. Equations (1) are accurate as long as there is no heat transfer nor particle exchange with the environment. Specifically, these equations assume the absence of weak reactions.

The form of Equations (1) demonstrate that following some change in composition dX_i (that determines some nuclear energy release dq) the changes in $d\rho$ and dT are independent of the rate in which this change took place. It follows that if all reaction rates are slower by some factor, then the fluid reaches the exact same state but over a time longer by the same factor. The burning limiter for hydrodynamical simulation suggested by Kushnir et al. (2013) multiplies all reaction rates by some factor to prevent unstable numerical burning and, therefore, accurately describes detonation waves over scales larger than those in which the limiter operates. In contrast, the burning limiter recently suggested by Shen et al. (2017) multiplies each reaction rate by a different factor (and also unnecessarily in regions where the burning is numerically stable), which suggests that the structure of the detonation wave over scales larger than those in which the limiter operates would be numerically distorted.

In order to calculate the structure of the detonation wave, a full derivative in time of Equations (1) is taken:

$$\begin{aligned} \frac{d\rho}{dt} &= \frac{\frac{\partial P}{\partial T} \left(\frac{\partial \varepsilon}{\partial T} \right)^{-1} \left(\frac{dq}{dt} - \sum_i \frac{\partial \varepsilon}{\partial X_i} \frac{dX_i}{dt} \right) + \sum_i \frac{\partial P}{\partial X_i} \frac{dX_i}{dt}}{u^2 - c_s^2} \\ &\equiv \frac{\phi}{u^2 - c_s^2}, \\ \frac{dT}{dt} &= \left(\frac{\partial P}{\partial T} \right)^{-1} \left[\left(u^2 - \frac{\partial P}{\partial \rho} \right) \frac{d\rho}{dt} - \sum_i \frac{\partial P}{\partial X_i} \frac{dX_i}{dt} \right]. \end{aligned} \quad (4)$$

The integration of Equations (4) yields the state of a fluid element as a function of the time since it was shocked, given the reaction rates

$$dX_i/dt = f_i(\rho, T, \{X_j\}). \quad (5)$$

Equation (5) includes the complexity of the problem, as many isotopes have to be included in the integration with many reactions. We present our results as a function of the distance behind the shock wave, x , connected to the time through $u = dx/dt$.

We use the following definitions for the average nucleon number and proton number:

$$\bar{A} = \frac{1}{\sum_i X_i/A_i}, \quad \bar{Z} = \bar{A} \sum_i Z_i X_i/A_i, \quad (6)$$

where Z_i is the proton number of isotope i . We also define for the heavy isotopes:

$$\bar{Y} = \sum_{i,i \neq n,p,\alpha} Y_i, \quad \bar{X} = \frac{1}{\bar{Y}} \sum_{i,i \neq n,p,\alpha} X_i. \quad (7)$$

It is convenient to normalise densities, $\rho_7 = \rho[\text{g}/\text{cm}^3]/10^7$, and temperatures, $T_9 = T[\text{K}]/10^9$.

2.1 The level of accuracy

We differentiate between the numerical accuracy (or convergence) of the results, which depends on the numerical scheme, and their uncertainty, which depends on the level of approximations that we

introduce, as well as on the uncertainty of the input physics. Our aim, for a given set of input physics, is to reach a numerical accuracy of $\sim 10^{-3}$. This degree of numerical accuracy is appropriate for benchmarking and code checking. This numerical accuracy can be (and for many cases is) much higher than the uncertainty of the EOS and of the reaction rates that dominate the uncertainty budget.

The approximation of non-relativistic hydrodynamics is expected to introduce an error of $\text{MeV}/m_p c^2 \sim 10^{-3}$ for thermonuclear detonation waves. We further approximate the nuclear masses as $m_i \approx A_i m_u$, where m_u is the atomic mass unit, unless stated otherwise. This approximation is always better than 1% for each isotope, and the relevant isotopes with significant errors are: n (error of $\approx 8.6 \times 10^{-3}$), p ($\approx 7.8 \times 10^{-3}$), ^2H ($\approx 7.0 \times 10^{-3}$), ^3H ($\approx 5.3 \times 10^{-3}$), ^3He ($\approx 5.3 \times 10^{-3}$), ^6Li ($\approx 2.5 \times 10^{-3}$), ^7Li ($\approx 2.3 \times 10^{-3}$) and ^7Be ($\approx 2.4 \times 10^{-3}$). Since the total mass fraction of these isotopes is at most a few percent under the conditions relevant for thermonuclear detonation waves, the approximation of $m_i \approx A_i m_u$ introduces an error smaller than $\sim 10^{-3}$. The total mass fraction of other isotopes with a similar significant deviation from $m_i \approx A_i m_u$ is always small. The level of error introduced by the absence of weak reactions is discussed in Section 7.

3 INPUT PHYSICS

3.1 Nuclear statistical equilibrium (NSE)

NSE is the unique nuclear composition of a system when strong and electromagnetic interactions are in a state of detailed balance for a given set of thermodynamic state variables and electron fraction. Applying a detailed balance to the reaction that breaks up a nucleus with a nucleon number A_i and a proton number Z_i into free nucleons (A_i, Z_i) $\leftrightarrow Z_i p + N_i n$, where $N_i = A_i - Z_i$, yields a relation between the chemical potential of the nucleus μ_i and the chemical potential of free protons μ_p and neutrons μ_n : $\mu_i = Z_i \mu_p + N_i \mu_n$ (Clifford & Taylor 1965). The last relation can be written as

$$Z_i \mu_p + N_i \mu_n = m_i c^2 + k_B T \ln \left[\frac{n_i}{w_i(T)} \left(\frac{h^2}{2\pi m_i k_B T} \right)^{3/2} \right] + \mu_i^{\text{coul}}, \quad (8)$$

where k_B is Boltzmann's constant, h is Planck's constant, n_i is the number density and μ_i^{coul} is a Coulomb interaction term (Calder et al. 2007). The coulomb term and the conditions under which Equation (8) is valid are discussed in Section 3.4. The mass fractions of all nuclei in a NSE can therefore be expressed in terms of the chemical potential of the protons and the neutrons and the nuclear binding energies $Q_i = (Z_i m_p + N_i m_n - m_i) c^2$:

$$\begin{aligned} X_i &= \frac{m_i}{\rho} w_i(T) \left(\frac{2\pi m_i k_B T}{h^2} \right)^{3/2} \\ &\times \exp \left[\frac{Z_i (\mu_p + \mu_p^{\text{coul}}) + N_i \mu_n - \mu_i^{\text{coul}} + Q_i}{k_B T} \right], \end{aligned} \quad (9)$$

where $w_i(T)$ are the nuclear partition functions. Since the mass fractions of all nuclei must sum to one, $\sum_i X_i = 1$, and the nuclear composition has the prescribed electron fraction, $Y_e \approx \sum_i X_i Z_i/A_i$, for a given ρ , T , and Y_e , the mass fractions of all the isotopes can be found by solving for the neutron and proton chemical potentials that satisfy the two constraints. The NSE state is found in this work by using a modified version of the NSE routine of Frank Timmes².

² <http://cococubed.asu.edu/>

Specifically, we include in Eq. (9) the ion-ion Coulomb interaction terms of Chabrier & Potekhin (1998) (see detailed discussion in Section 3.4) and we use the accurate nuclear masses, m_i .

The nuclear masses and partition functions were taken from the file WINVNV_2.0.DAT, which is available through the JINA reaclib database³ (Cyburt et al. 2010, JINA). For those isotopes whose m_i values in WINVNV_2.0.DAT differed from the most updated values given in the ENSDF database⁴, \tilde{m}_i , we used the latter values instead. The list of isotopes for which m_i and \tilde{m}_i differ is given in Table A1 of Appendix A, together with their mass values. The file WINVNV_2.0.DAT provides the values of $w_i(T)$ over some specified temperature grid in the $[10^8, 10^{10}]$ K range. For numerical stability it is better to fit the $w_i(T)$ values to some function rather than interpolate. We use the functional form suggested by Woosley et al. (1978):

$$w_i(T) = (2J_{i,0} + 1) \left(1 + \sum_k E_{i,k} \exp(-F_{i,k}/T_9) \right) \times \exp\left(a_i/T_9 + b_i + c_i T_9 + d_i T_9^2\right), \quad (10)$$

where $(2J_{i,0} + 1)$ is the statistical weight for the ground state of isotope i and a_i is negative. We initially used an extended list of 581 isotopes (see Table 1) to find suitable sets of isotopes for the integration of Eqs. (4) (see Section 3.2). We could usually fit the nuclear partition function for the extended list of isotopes with $E_{i,k}$ being equal to zero to better than 10% over the relevant temperature range $[1.5 \times 10^9, 10^{10}]$ K. In the case that such a fit was not possible, low-lying excited levels with $J_{i,k}$ and the excitation energy $\varepsilon_{i,k}$ [MeV] were added, where $E_{i,k} = (2J_{i,k} + 1)/(2J_{i,0} + 1)$ and $F_{i,k} = 11.6045\varepsilon_{i,k}$. The addition of, at most, three low-lying excited levels typically sufficed to fit to better than 10%. For two isotopes the fit was slightly worse: ^{78}As ($\sim 12.7\%$) and ^{89}Kr ($\sim 19.6\%$). The inaccuracies of the fit functions negligibly effect the results (see discussion in Section 4). We make the fit parameters for all isotopes publicly available⁵. We note that for some isotopes, the values of $J_{i,0}$ in WINVNV_2.0.DAT differ from the most updated values given in the ENSDF database. In these cases, we used the values of ENSDF, $\tilde{J}_{i,0}$, and normalised the $w_i(T)$ values from WINVNV_2.0.DAT to $\tilde{w}_i(T)$ as follows:

$$\tilde{w}_i(T) = 1 + \frac{2\tilde{J}_{i,0} + 1}{2J_{i,0} + 1} (w_i(T) - 1). \quad (11)$$

The list of isotopes for which $J_{i,0}$ and $\tilde{J}_{i,0}$ differ is given in Table A2 of Appendix A, together with their spin values.

When nearing a state of NSE, the plasma may be in an intermediate state of nuclear-statistical-quasi-equilibrium (NSQE; Bodansky et al. 1968), in which a group of heavy isotopes are in detailed balance. We assume that at NSQE there is an equilibrium of neutrons, protons, and α -particles, and that the state of NSQE is determined by specifying ρ , T , Y_e and \tilde{Y} (for a detailed discussion, see Khokhlov 1989).

3.2 Nuclear reaction network

Previous studies of thermonuclear detonation waves employed lists of isotopes that were considered extensive enough. However, this assumption was not backed up by any quantitative calculation, so one cannot estimate the error introduced by these lists of isotopes. Moreover, inclusion of irrelevant isotopes can decrease the numerical accuracy. We, therefore, aim at finding a reasonably short list of isotopes that allows the calculation of a thermonuclear detonation wave with some prescribed degree of accuracy.

Given some minimal abundance Y_{\min} , we include in the list every isotope that has a NSE number abundance that is $Y_i > Y_{\min}$ for some ρ , T and Y_e within our range of interest. These lists have to be supplemented with other isotopes that, while not represented in the NSE state, are significant for the burning process. Specifically, the relaxation to a NSE state is controlled by slow reactions between low- Z isotopes (Khokhlov 1989, who suggested that $^{12}\text{C} \leftrightarrow 3\ ^4\text{He}$ is the most important one; see the discussion in Sections 5.1.3 and 5.2.2). We, therefore, add to the list of isotopes obtained from the NSE condition more isotopes, in several stages, which are described below.

For the NSE condition, we scan the ranges $T \in [2 \times 10^9, 3 \times 10^{10}]$ K, $\rho \in [100, 10 \times 10^{10}]$ g/cm³ and $Y_e \in [0.495, 0.5]$ with our extended list of 581 isotopes (see Table 1). The extended list includes all the available isotopes with $Z \leq 14$ from the file WINVNV_2.0.DAT that satisfy the following two conditions:

- (i) JINA includes strong reactions that connect the isotope to the bulk of the isotopes (say to ^{56}Ni). In other words, a subnet of a few isotopes is not allowed.
- (ii) The isotope's decay time is longer than the Carbon burning time scale in CO detonations (~ 1 ns).

We further add to our list of isotopes an extended pool of isotopes with $Z > 14$ that is sufficient in terms of the conditions described below. In the first stage, we obtained lists for a few values of $Y_{\min} = 10^{-y}$; we name these lists NSE y ($y = 4, 5, 6, 7$). Next, we add to these lists isotopes that describe burning through α -elements; we call this isotope list α -ext and it includes:

- (i) n , p and the α -isotopes ^4He , ^{12}C , ^{16}O , ^{20}Ne , ^{24}Mg , ^{28}Si , ^{32}S , ^{36}Ar , ^{40}Ca , ^{44}Ti , ^{48}Cr , ^{52}Fe and ^{56}Ni .
- (ii) All isotopes that differ from α -isotopes by n , p or α .
- (iii) ^{22}Ne , since it has a significant mass fraction for some initial conditions.
- (iv) All isotopes of an element between the minimal and the maximal nucleon numbers determined from the previous steps.
- (v) We exclude ^5He and ^9B from the list, see below.

The obtained α -ext list includes 78 isotopes and is presented in Table 1. For example, the list NSE7 contains all the isotopes in the α -ext list except for ^{19}Ne , so we add this isotope to NSE7. Next, we include all NSE7 isotopes with a $Z \leq 14$ in NSE4 – 6. This increases only slightly the sizes of these nets and improves the calculation of the low- Z isotopes. The obtained lists are presented in Table 1. One can verify that the extended list includes for each element at least one additional isotope with a smaller (larger) nucleon number compared to our most detailed NSE7 list, or that there are no more isotopes with smaller or larger nucleon numbers (bold numbers in Table 1). Furthermore, the extended list contains isotopes of Br and Kr, none of which survive in NSE7. Unless otherwise stated, the NSE7 net is the one used from this point on in the text.

Finally, in order to verify that we are not missing any impor-

³ <https://groups.nslc.msu.edu/jina/reaclib/db/index.php>

⁴ <https://www.nndc.bnl.gov/ensdf/>

⁵ The file ISOTOPES_PFIT.DATA available through <https://www.dropbox.com/sh/t6js2c0i96j8vvgg/AACrk93NR8i2LyDyYO91Eu4ma?dl=0>

tant low- Z isotopes, we add to the NSE7 list all the isotopes with a $Z \leq 14$ from the extended list that have a measured mass and ground-state spin (not calculated)⁶. We call this list NSE7Si and it is presented in Table 1.

The forward reaction rates are taken from JINA (the default library of October 20, 2017). All strong reactions that connect between isotopes from the list are included (this requires some modification of the relevant subroutines of MESA). To allow the plasma to reach a NSE, inverse reaction rates were determined according to a detailed balance. We modified the relevant subroutine of MESA so as to be exactly compatible with Equation (9), including the correction of a few bugs (see Appendix C). Enhancement of the reaction rates due to screening corrections and their compatibility with Equation (9) are described in Section 3.4.

We note that the total cross-sections for the reactions $^{12}\text{C}+^{16}\text{O}$ and $^{16}\text{O}+^{16}\text{O}$ given by JINA seem to be erroneous. According to JINA, these rates are taken from Caughlan & Fowler (1988, CF88). Caughlan & Fowler (1988) provide the total cross-section for these reactions, as well as the yields of n , p , and α for these reactions. They note that the sum of these yields can exceed unity because of reactions such as $^{16}\text{O}(^{16}\text{O}, np)^{30}\text{P}$ and $^{16}\text{O}(^{16}\text{O}, 2p)^{30}\text{Si}$. This should not be confused with branching ratios for different channels that always sums up to unity. Since the branching ratios are not given by Caughlan & Fowler (1988) for the $^{12}\text{C}+^{16}\text{O}$ and $^{16}\text{O}+^{16}\text{O}$ reactions, it is not clear how the branching ratios were determined for the n , p , and α channels provided by JINA for these reactions (other channels, such as np and $2p$, are not provided). Nevertheless, the total cross-section for these reactions (sum over all channels) should equal the one given by Caughlan & Fowler (1988). As shown in Figure 1, this is not the case, and the total cross-sections⁷ provided by JINA are significantly larger. The total cross sections provided by JINA are larger by factors that roughly equal the total yields (dashed lines in Figure 1), which suggests that the reason for the discrepancy is the use of yields as branching ratios (which is erroneous, since the total yields can exceed unity). For comparison, we also present in Figure 1 the reaction $^{12}\text{C}+^{12}\text{C}$, where the total yields sum up to unity. We also present in Figure 1 the total cross-sections provided by v65A_090817 of STARLIB⁸ (Sallaska et al. 2013), which are similarly erroneous. This is probably because these rates were copied from JINA to STARLIB (see Section 3.7 of Sallaska et al. 2013). Recently, Fields et al. (2017) used STARLIB to study the impact of uncertainties in the thermonuclear reaction rates on the properties of core-collapse supernova progenitors. Despite the extensive discussion presented by Fields et al. (2017) regarding uncertainties in the $^{12}\text{C}+^{16}\text{O}$ and $^{16}\text{O}+^{16}\text{O}$ rates, they seem to be unaware of the discrepancies presented here. In this work, we normalised all the channels of the $^{12}\text{C}+^{16}\text{O}$ and $^{16}\text{O}+^{16}\text{O}$ reactions such that the total cross-sections are identical to the ones provided by Caughlan & Fowler (1988) while keeping the branching ratios provided by JINA.

3.3 Equation of state

The EOS is composed of contributions from electron-positron plasma, radiation, ideal gas for the nuclei, Coulomb corrections and

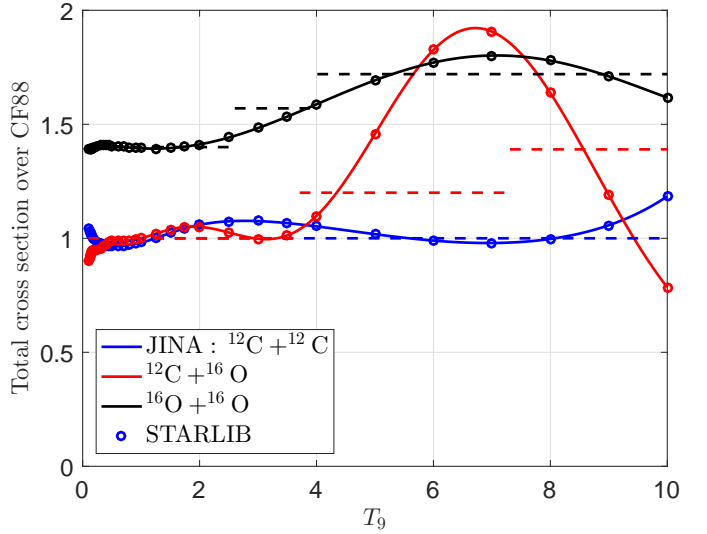


Figure 1. Total cross-sections of $^{12}\text{C}+^{12}\text{C}$ (blue), $^{12}\text{C}+^{16}\text{O}$ (red) and $^{16}\text{O}+^{16}\text{O}$ (black) from the JINA reaclib database (solid lines) and from STARLIB (points) divided by the total cross-sections of Caughlan & Fowler (1988). The ratios for $^{12}\text{C}+^{16}\text{O}$ and for $^{16}\text{O}+^{16}\text{O}$ are larger by factors that roughly equal the total yields of the reactions (dashed lines, as given by Caughlan & Fowler 1988), which suggests that the reason for the discrepancy is the use of yields as branching ratios (which is erroneous, since the total yields can exceed unity).

nuclear level excitations:

$$\begin{aligned}
 \varepsilon &= \varepsilon_{ep} + \varepsilon_{\text{rad}} + \varepsilon_{\text{ion}} + \varepsilon_{\text{cou}} + \varepsilon_{\text{ex}}, \\
 p &= p_{ep} + p_{\text{rad}} + p_{\text{ion}} + p_{\text{cou}}, \\
 S &= S_{ep} + S_{\text{rad}} + S_{\text{ion}} + S_{\text{cou}} + S_{\text{ex}}. \quad (12)
 \end{aligned}$$

We use the Timmes EOS⁹ (Timmes & Arnett 1999) for the electron-positron plasma and the EOS provided by MESA for the ideal gas part of the nuclei, for the radiation and for the Coulomb corrections (but based on Chabrier & Potekhin (1998) and not on Yakovlev & Shalybkov (1989), see detailed discussion in Section 3.4). The reason for not using the more efficient *Helmholtz* EOS (Timmes & Swesty 2000) is discussed in Section 3.3.3. We further include the nuclear level excitation energy of the ions and a more accurate expression for the entropy of the ions. As demonstrated in Section 4, the nuclear level excitations can be the most important correction term for an ideal EOS for the relevant thermodynamic states. Although this term was included in Khokhlov (1988) and probably also in Khokhlov (1989, see discussion in Section 5.1.5), it is not part of the EOS routines provided by FLASH (Fryxell et al. 2000) and MESA. In fact, this term is not even mentioned in Fryxell et al. (2000) as a relevant correction for an ideal EOS, who argued that the most important correction is the ion-ion Coulomb interaction term. We show below that nuclear level excitations can be a more important correction to the energy than the Coulomb correction (but since nuclear level excitations do not contribute to the pressure, the Coulomb correction is the most important correction to the pressure). Further modifications, which in-

⁶ ^{10}C is excluded for a reason that is discussed in Section 5.

⁷ the $^{12}\text{C}(^{16}\text{O}, n)^{27}\text{Si}$ rate is calculated as the reverse rate of $^{27}\text{Si}(n, ^{12}\text{C})^{16}\text{O}$.

⁸ <https://starlib.github.io/Rate-Library/>

⁹ <http://cococubed.asu.edu/>

Table 1. The lists of isotopes used in this work. Bold numbers mark the minimal or maximal nucleon numbers available in WINVNV_2.0.DAT.

Element	Extended 581 isotopes	NSE7Si 344 isotopes	NSE7 260 isotopes	NSE6 218 isotopes	NSE5 179 isotopes	NSE4 137 isotopes	α – ext 78 isotopes
n	1	1	1	1	1	1	1
H	1-3	1-3	1-3	1-3	1-3	1-3	1-3
He	3-4, 6	3-4, 6	3-4, 6	3-4, 6	3-4, 6	3-4, 6	3-4
Li	6-9	6-9	6-7	6-7	6-7	6-7	–
Be	7, 9-13	7, 9-13	7, 9-10	7, 9-10	7, 9-10	7, 9-10	–
B	8, 10-14^a	8, 10-14	10-11	10-11	10-11	10-11	11
C	9-17^b	9, 11-16^c	11-14	11-14	11-14	11-14	11-13
N	12-20	12-19	13-15	13-15	13-15	13-15	13-15
O	13-24^d	13-24	15-18	15-18	15-18	15-18	15-17
F	14-27^e	14-27	17-19	17-19	17-19	17-19	17-19
Ne	17-34^f	17-31	19-23	19-23	19-23	19-23	19-22
Na	19-37 ^g	19-33	21-25	21-25	21-25	21-25	21-23
Mg	20-40^h	20-36	23-28	23-28	23-28	23-28	23-25
Al	22-43ⁱ	23-35	25-30	25-30	25-30	25-30	25-27
Si	23-44^j	24-40	27-33	27-33	27-33	27-33	27-29
P	26-40	29-35	29-35	29-34	29-33	29-31	29-31
S	28-45	30-37	30-37	31-37	31-36	31-33	31-33
Cl	31-46	32-39	32-39	33-39	33-37	33-35	33-35
Ar	32-49	34-42	34-42	35-41	35-39	35-37	35-37
K	35-51	37-45	37-45	37-44	37-41	37-39	37-39
Ca	36-54	38-48	38-48	39-47	39-45	39-41	39-41
Sc	40-56	41-51	41-51	41-50	41-48	41-43	41-43
Ti	40-58	43-53	43-53	43-52	43-51	43-50	43-45
V	42-58	45-55	45-55	45-54	43-53	45-51	45-47
Cr	44-59	47-57	47-57	47-56	47-55	47-54	47-49
Mn	46-60	49-59	49-59	49-58	49-57	49-56	49-51
Fe	48-64	50-62	50-62	51-61	51-59	51-58	51-53
Co	50-65	52-64	52-64	53-63	53-61	53-60	53-55
Ni	52-71	54-66	54-66	55-65	55-64	55-61	55-57
Cu	54-72	56-68	56-68	57-67	57-65	57-61	57
Zn	56-77	58-70	58-70	59-69	60-67	–	–
Ga	58-78	61-72	61-72	62-70	–	–	–
Ge	60-82	64-74	64-74	69-71	–	–	–
As	62-83	69-75	69-75	–	–	–	–
Se	64-86	75	75	–	–	–	–
Br	70-86	–	–	–	–	–	–
Kr	71-91	–	–	–	–	–	–

^a ^{17–18}B form a subnet.

^b ^{20–21}C form a subnet.

^c ¹⁰C is excluded for a reason that is discussed in Section 5.

^d ^{25–28}O is too short lived.

^e ²⁸F is too short lived.

^f ^{35–38}Ne is too short lived.

^g ^{18,38–42}Na is too short lived.

^h ^{41–45}Mg is too short lived.

ⁱ ^{44–48}Al is too short lived.

^j ^{45–51}Si is too short lived.

clude bug corrections, are described in Appendix B. We make our eos publicly available¹⁰.

¹⁰ The files are available through <https://www.dropbox.com/sh/o1walp3f4qoy8lo/AABz7LJC-4fUjnb9OoWG3UvPa?dl=0>

3.3.1 Nuclear level excitations

The nuclear level excitation energy is given by (Landau & Lifshitz 1980):

$$\varepsilon_{ex} = N_A k_B T \sum_i Y_i \frac{\partial \ln w_i(T)}{\partial \ln T}. \quad (13)$$

The nuclear level excitations do not contribute to the pressure, but they do contribute to the entropy:

$$S_{ex} = \varepsilon_{ex}/T. \quad (14)$$

The input parameters for the EOS routines in MESA are ρ , T , \bar{A} and \bar{Z} . In order to calculate ε_{ex} , the routines must be modified to include X_i as input parameters. The routines were further modified to supply partial derivatives with respect to X_i , in order to integrate Equations (4).

3.3.2 A more accurate expression for the entropy of the ions

The entropy of the ions (not including the nuclear level excitations) is given by (see, e.g., Shapiro & Teukolsky 1983):

$$S_{\text{ion}} \approx k_B N_A \sum_i \frac{X_i}{A_i} \ln \left[\frac{e^{5/2} (2\pi k_B T)^{3/2}}{h^3} \frac{(A_i)^{5/2}}{\rho X_i} w_i(T) \right]. \quad (15)$$

This expression can be compared with the one used by MESA:

$$S_{\text{ion}} = \frac{k_B N_A}{\bar{A}} \ln \left[\frac{e^{5/2} (2\pi k_B T)^{3/2}}{h^3} \frac{(\bar{A})^{5/2}}{\rho} \right], \quad (16)$$

which assumes $w_i(T) = 1$ and averages in some sense over the mass fractions. This is a reasonable choice in the case that X_i are not given, but since X_i are required in order to calculate the nuclear level excitations, we use the more accurate expression for the entropy, Equation (15).

3.3.3 The inconsistency of the Helmholtz EOS

Integrating Equations (4) in a highly accurate manner requires a high degree of accuracy for the partial derivatives of the pressure and the internal energy with respect to the independent variables. We have found that the *Helmholtz* EOS does not provide consistent values for $\partial p / \partial \rho$ at high temperatures and low densities. This is demonstrated in Figure 2, which presents the relative difference between the value provided by *Helmholtz* EOS for $\partial p / \partial \rho$ and the value calculated by directly differencing the pressure provided by *Helmholtz* EOS with respect to the density (the relative difference of the density was 10^{-7} for the direct differencing), $(\partial p / \partial \rho)_d$, for CO. Inconsistencies that exceed 10^{-3} are obtained at high temperatures and low densities. In fact, the inconsistency of the electron-positron part of the pressure is much larger (and exceeds unity) but the other (analytical) parts of the pressure dominate at high temperatures and low densities. We, therefore, use the Timmes EOS, for which $\partial p / \partial \rho$ is consistent to better than $\sim 10^{-5}$ (and to better than $\sim 10^{-3}$ just for the electron-positron part of the pressure).

3.4 Coulomb corrections

For the plasma conditions relevant to thermonuclear supernovae, the ion-electron interaction, $\bar{Z} e^2 (4\pi n_e / 3)^{1/3}$, where e is the electron charge and n_e is the electron number density, is weak compared to the kinetic energy of the electrons ($\lesssim 10\%$ at most). Assuming commutativity of the kinetic and potential operators and the separation of the traces of the electronic and ionic parts of the Hamiltonian, the non-ideal corrections to the plasma due to the Coulomb interaction can be divided into exchange-correlation of the electron fluid (electron-electron), ion-electron (polarisation) interaction and ion-ion interaction (see, e.g., Chabrier & Potekhin 1998). The relevant conditions for thermonuclear supernovae include both the relativity parameter, $p_F / m_e c$, where p_F is the zero-temperature Fermi momentum of electrons, and the degeneracy parameter, T / T_F , where T_F is the Fermi temperature, larger or smaller than unity.

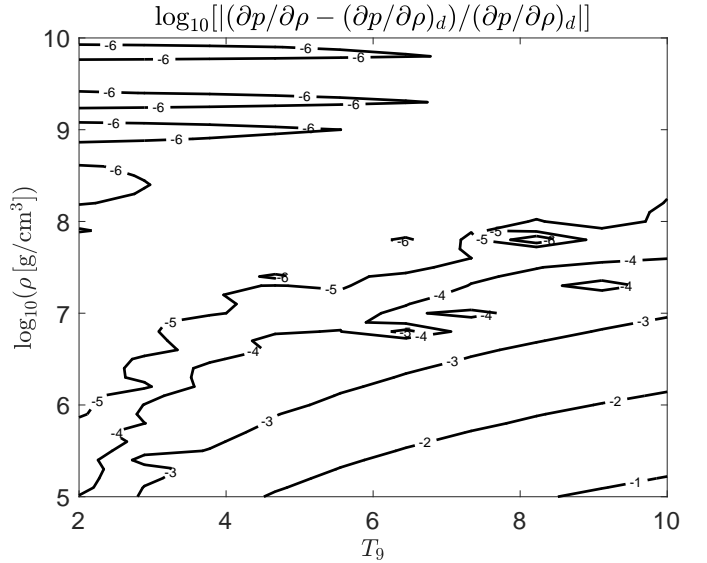


Figure 2. The relative difference between $\partial p / \partial \rho$, as provided by *Helmholtz* EOS, and the value calculated by the direct differencing of the pressure provided by *Helmholtz* EOS with respect to the density (the relative difference of the density was 10^{-7} for the direct differencing), $(\partial p / \partial \rho)_d$, for CO. Inconsistencies that exceed 10^{-3} are obtained at high temperatures and low densities. In fact, the inconsistency of the electron-positron part of the pressure is much larger (and exceeds unity) but the other (analytical) parts of the pressure dominate at high temperatures and low densities.

An analytical parameterisation of the electron-electron term (exchange and correlation) was given for non-relativistic electrons by Ichimaru et al. (1987) and by Stolzmann & Blöcker (2000). For relativistic electrons, the exchange part was given for high degeneracy by Stolzmann & Blöcker (2000)¹¹ and the full term (exchange and correlation) was given by Jancovici (1962) for zero temperature. As far as we know, there is no available parameterisation of the correlation part for relativistic electrons at finite temperatures, nor for the exchange part for relativistic electrons at slight degeneracy, as they are expected to be small. Since these regimes are relevant for thermonuclear supernovae, we inspected the available exchange and correlation terms near these regimes and found them to be a correction smaller than 0.1%. However, we cannot verify that they are on the sub-percent level throughout these regimes. For regimes where a parameterisation of the electron-electron term is available, the correction is larger than 1% only for low densities $\rho_7 \lesssim 0.03$ and low temperatures $T_9 \lesssim 0.2$. We will hereunder avoid these regions (unless stated otherwise), and, therefore, neglect the electron-electron term, which introduces a sub-percent order of uncertainty. We also neglect the ion-electron term, given for arbitrary degeneracy and relativity of the electrons by Potekhin & Chabrier (2000), as it introduces a correction smaller than 3×10^{-3} for the relevant conditions of thermonuclear supernovae.

The ion-ion interaction term for a plasma with only one type of N_i ions is given as the dimensionless Helmholtz free energy $F_i / N_i k_B T \equiv f_i = f(\Gamma_i)$, with an ion coupling parameter $\Gamma_i = Z_i^{5/3} \Gamma_e$ and an electron coupling parameter $\Gamma_e \approx (4\pi \rho N_A Y_e / 3)^{1/3} e^2 / k_B T$. It is useful to note that $\Gamma_i \approx 1.1(T/2 \times$

¹¹ Note that their equation (82) is wrong by a minus sign, and their equation (85) should be $u_{ee}^x = f_{ee}^x (1 + V_\lambda^b / V^b + W_\lambda^b / W^b)$.

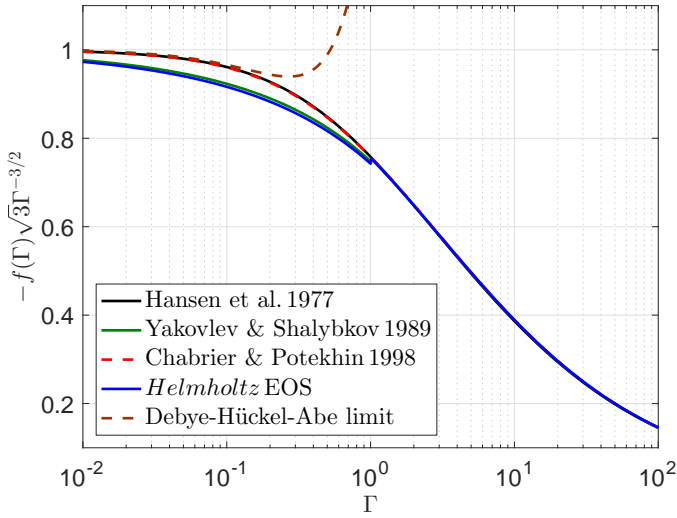


Figure 3. Different fits for $f(\Gamma)$: Hansen et al. (1977, black), Yakovlev & Shalybkov (1989, green), Chabrier & Potekhin (1998, red), the fit implemented in *Helmholtz* EOS (blue) and the Debye-Hückel-Abe (Abe 1959) limit for $\Gamma \ll 1$.

$10^8 \text{ K}^{-1} (Y_e \rho / 10^9 \text{ g cm}^{-3})^{1/3} Z_i^{5/3}$. A useful 4-parameter fit for $f(\Gamma)$ was given by Hansen et al. (1977), which is shown in Figure 3. The fit interpolates between the Debye-Hückel-Abe (Abe 1959) result in the weak coupling limit ($\Gamma \ll 1$) and the strong coupling limit ($\Gamma \gg 1$) that can be simulated. The fit is not valid above the melting point ($\Gamma \approx 175$). Later on, Yakovlev & Shalybkov (1989) provided a fit for $f(\Gamma)$ with a different functional form. Their results do not deviate by more than 4% from the fit of Hansen et al. (1977), but their fit is not continuous at $\Gamma = 1$; see Figure 3. This is because they required continuity only for $\Gamma df/d\Gamma$, but this leads, for example, to a discontinuity in the entropy. The *Helmholtz* EOS uses the same functional form of Yakovlev & Shalybkov (1989) with somewhat different numerical values, and suffers from the same problem. Chabrier & Potekhin (1998) used the fit of Hansen et al. (1977) with 3 parameters, and their results do not deviate by more than 1% from the fit of Hansen et al. (1977). Finally, Potekhin & Chabrier (2000) introduced a 7-parameter fit¹² that deviates from the 3-parameter fit of Chabrier & Potekhin (1998) by less than a percent. We hereunder use the fit for $f(\Gamma)$ of Chabrier & Potekhin (1998) since it is the simplest one and it is accurate to better than a percent.

When the plasma comprises a mixture of different ions, there are situations where the linear mixing rule (LMR), which states that the correction is a number weighted linear sum of one component plasma, is a good approximation (Hansen et al. 1977). If the LMR applies, then the Coulomb correction to the chemical potential of each ion is given by $\mu_i^{\text{Coul}} = k_B T f_i$ and is independent of the other ions. Nevertheless, at the weak coupling regime the LMR fails, as the Debye-Hückel limit is non-linear. Potekhin et al. (2009a) and Potekhin et al. (2009b) studied the transition to the Debye-Hückel limit and showed that the LMR is accurate to better than 10% for $\langle \Gamma \rangle = \langle Z_i^{5/3} \rangle \Gamma_e > 1$, where $\langle Z_i^{5/3} \rangle$ is a number weighted sum. The relevant NSE state of the detonation waves are

in the regime $0.1 \lesssim \langle \Gamma \rangle \lesssim 1$, where the LMR can introduce deviations of up to $\sim 30\%$. Even larger deviations can be obtained for $0.01 \lesssim \langle \Gamma \rangle \lesssim 0.1$, which is typical of the post-shock conditions of Helium detonations (although the plasma includes mainly Helium ions there). Potekhin et al. (2009b) suggested a modification of f_i to accurately describe the transition to the Debye-Hückel limit. This modification makes μ_i^{Coul} dependant on other ions in the plasma, which significantly complicates the calculation of the NSE state (Nadyozhin & Yudin 2005). We show later that the Coulomb correction changes the NSE state by a few percent, which means that the modification of the LMR is usually a sub-percent correction (but could be higher). We, therefore, choose in this work to adopt the LMR.

Once the ion-ion terms are determined, the correction of the EOS, the correction of the NSE relation, Equation (9), and the screening of the thermonuclear reaction can be calculated self-consistently. Usually, however, this is not the case. Sometimes only the corrections to the EOS are considered (e.g., as in Khokhlov 1988, 1989), and sometimes all corrections are considered but not in a consistent way (see below). Here we consider all corrections in a consistent way. Following Khokhlov (1988), the correction of the EOS is approximated by $f(\Gamma)$ for a ‘mean’ nucleus $\Gamma = \bar{Z}^{5/3} \Gamma_e$. This introduces an error of only a few percent compared with summing over all ions and significantly simplifies the calculation of these corrections. For the NSE relation, we use $\mu_i^{\text{Coul}} = k_B T f_i$, and this determines, from detailed balance, the screening factors of all thermonuclear reactions (Kushnir & Waxman 2018). In brief, consider the screening of a reaction with reactants $i = 1, \dots, N$ with charges Z_i . The screening factor for this reaction is identical to the screening factor of a reaction in which all reactants form a single isotope j with a charge $Z_j = \sum_{i=1}^N Z_i$ and a photon. The inverse reaction, photo-disintegration, is not screened, and, therefore, from the detailed balance condition we get for the screening factor:

$$\exp\left(\frac{\sum_{i=1}^N \mu_i^C - \mu_j^C}{k_B T}\right) \quad (17)$$

(same as equation (15) of Dewitt et al. 1973, for the case of $N = 2$). Any other choice would either not satisfy a detailed balance (e.g., the screening routines available in MESA) or would make the photo-disintegration reaction density dependent (as in Calder et al. 2007), which is not physical. We hereunder refer to both the inclusion of the Coulomb correction terms for the NSE and the screening of thermonuclear reaction as the ‘‘Coulomb correction term for the NSE state’’.

4 CJ DETONATIONS

In this section, we calculate several properties of the CJ detonations. This is useful because CJ detonations are independent of reaction rates, which allows an efficient benchmarking for the EOS and the NSE routines. Furthermore, even for initial conditions where the unsupported detonation is pathological, the final CJ NSE conditions provide a good approximation for the pathological NSE conditions. We numerically determined the CJ detonation speed, D_{CJ} , to an accuracy of $\sim 10^{-6}$, which allows benchmarking to the accuracy level we aimed for, 10^{-3} . In Section 4.1, we consider the initial composition of CO. We further compare our results to Bruenn (1972) (Section 4.1.1), to Khokhlov (1988) (Section 4.1.2) and to Gamezo et al. (1999) (Section 4.1.3). In Section 4.2, we consider the initial composition of pure Helium, and compare our results to Mazurek (1973b) (Section 4.2.1) and to Khokhlov (1988)

¹² Note that the term $-B_2 \ln(1 + \Gamma/B_1)$ in their equation (16) should be replaced with $-B_2 \ln(1 + \Gamma/B_2)$.

(Section 4.2.2). We exploit the comparisons to previous works to highlight the sensitivity of the results to various assumptions.

4.1 CJ detonations of Carbon-Oxygen mixtures

The calculated D_{CJ} for CO is presented in the upper panel of Figure 4 for an upstream temperature of $T_{0,9} = 0.2$ and an upstream density in the relevant range for supernovae, $[10^6, 5 \times 10^9] \text{ g/cm}^3$. Similarly to Gamezo et al. (1999); Dunkley et al. (2013), we find that D_{CJ} is not a monotonic function of ρ_0 and that it has a maximum at $\rho_{0,7} \approx 0.35$ and a minimum at $\rho_{0,7} \approx 4.3$ (the minimum can also be extracted from table IV of Khokhlov (1988)). Key isotopes at the CJ NSE state are presented in the bottom panel of Figure 4 for the same upstream values. We only present the mass fraction of isotopes that have a mass fraction larger than 5×10^{-2} at some ρ_0 within the inspected range. At low densities, the NSE state is dominated by ^{56}Ni (with $\bar{A} \approx 55$, $\bar{A} \approx 56$ at $\rho_{0,7} = 0.1$), while at higher densities the NSE state is mainly a mixture of ^4He , ^{54}Fe , ^{55}Co and ^{58}Ni (with $\bar{A} \approx 12$, $\bar{A} \approx 52$ at $\rho_{0,7} = 500$). A few key parameters of these CJ detonations are given in Table 2. The temperature at the CJ NSE state increases monotonically with ρ_0 , which decreases both the \bar{A} at these states and the released thermonuclear energy compared with the initial states, $q_{01,\text{CJ}}$. It is also demonstrated that the nuclear excitation energy contribution to the energy at the NSE state is slightly greater than a percent for the high densities, and is slightly larger in magnitude than the Coulomb correction.

The results do not depend much on the initial upstream temperature. The D_{CJ} values for $T_{0,9} = 0.04$ (the reason for choosing this temperature is explained in Section 5.1) deviate from the results for $T_{0,9} = 0.2$ by less than 10^{-3} , and the key parameters of Table 2 deviate by less than 0.6%, where the largest deviation is obtained for $q_{01,\text{CJ}}$ at $\rho_{0,7} = 500$.

The results calculated with the NSE4 (NSE5, NSE7Si) isotope list deviate from the results presented above by less than 10^{-3} (3×10^{-4} , 7×10^{-4}), which suggests that our isotope list is converged to better than 10^{-3} . The most uncertain input physics in this calculation is the Coulomb corrections. The contribution of the Coulomb energy to the initial state energy is of the order of a few percent (highest contribution in the lowest densities). A slightly smaller contribution is obtained at the NSE state (see Table 2). The Coulomb interaction terms also change the NSE state by a few percent (see Sections 4.1.1 and 4.1.2). We, therefore, estimate the uncertainty of the results to be on the sub-percent level (see Section 3.4).

4.1.1 Comparing CO CJ detonations to Bruenn (1972)

Bruenn (1972) calculated CJ detonations for an initial composition of $X(^{12}\text{C}) = X(^{16}\text{O}) = 0.49$, $X(^{22}\text{Ne}) = 0.02$, an upstream temperature of $T_{0,9} = 0.3$ and a few values of the upstream density in the range of $[5 \times 10^6, 3 \times 10^{10}] \text{ g/cm}^3$. We calculated the CJ NSE states for the same initial conditions by following the input physics of Bruenn (1972) as closely as possible. The EOS that was used for the CJ NSE values did not include nuclear-level excitation terms and probably did not include Coulomb terms as well. The list of isotopes included 341 isotopes¹³. When possible, the binding ener-

¹³ In figure 1 of (Bruenn 1972), only 337 isotopes are shown; together with n , p and ^4He , one isotope is missing. We assume that ^{44}S is missing from

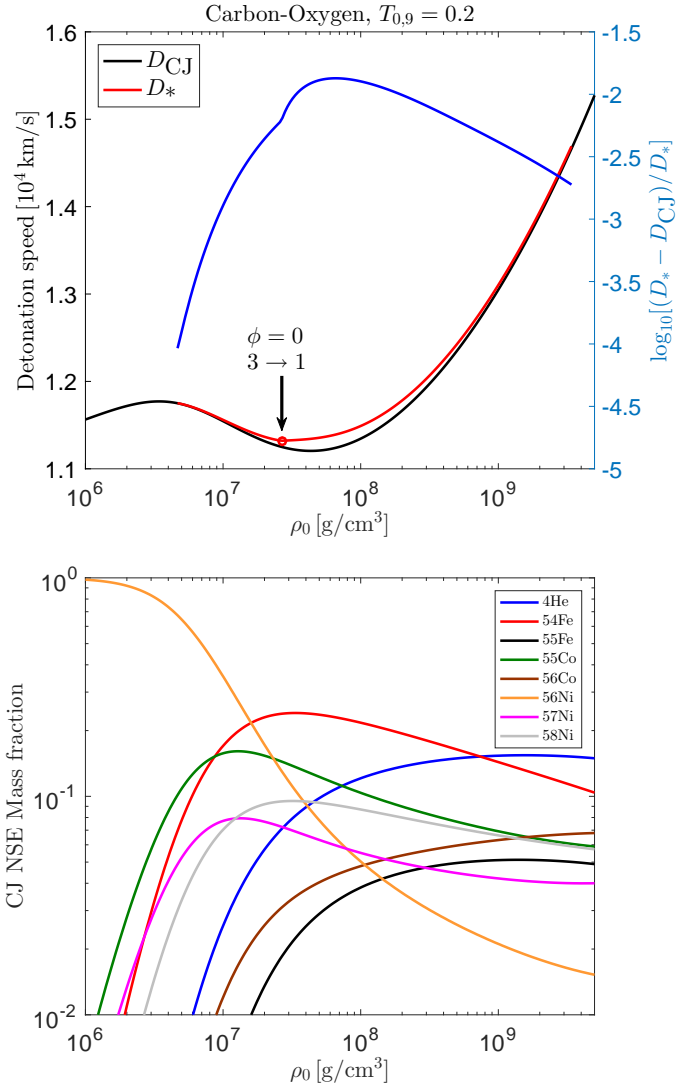


Figure 4. Upper panel: D_{CJ} (black) and D_* (red) for CO and upstream temperature of $T_{0,9} = 0.2$ as a function of the upstream density. The deviation between D_{CJ} and D_* (blue) is always smaller than $\approx 1.4\%$. We are unable to determine D_* with a high enough degree of accuracy for densities above $\rho_{0,7} = 340$ and below $\rho_{0,7} = 0.47$. Nevertheless, at high densities the decrease in the deviation as a function of the upstream density is smaller than exponential, which suggests that even at larger upstream densities the detonation remains pathological. At low densities, the deviation decreases exponentially with $1/\rho_0$ (see Figure 8), which suggests that the detonation remains pathological even at lower upstream densities. The minimum of D_* corresponds to a discontinuous behaviour of the sonic point location (see Section 5.1.3). Bottom panel: Mass fractions of key isotopes at the CJ NSE state for the same upstream conditions. We only present the mass fraction of isotopes that have a mass fraction larger than 5×10^{-2} at some ρ_0 within the inspected range.

gies are taken from Mattauch et al. (1965)¹⁴, and for the remainder,

figure 1 since both ^{43}S and ^{45}S are included, so we add it to the list of isotopes.

¹⁴ Some of the values in page 13 of Mattauch et al. (1965) are not clearly visible in the online scanned version. In these cases, we used the modern values, since the values in this paper are almost identical to the modern ones.

Table 2. Key parameters of CJ (upper rows for each upstream density) and pathological (lower rows for each upstream density, if available) detonations for CO and upstream temperature of $T_{0,9} = 0.2$

ρ_0 [g/cm ³]	P_0/ρ_0 [MeV/ m_p]	γ_0^a	D [10 ⁴ km/s]	P/ρ_0 [MeV/ m_p]	ρ/ρ_0	T [10 ⁹ K]	$\gamma^e b$	q_{01} [MeV/ m_p]	\bar{A}	\bar{A}	f_{coul}^c	f_{ex}^d
1×10^6	0.02958	1.5666	1.1564	0.6103	1.7122	3.140	1.3389	0.8186	55.22	55.96	-2.3	-4.5
3×10^6	0.05065	1.5146	1.1767	0.6522	1.7127	4.010	1.2984	0.7954	46.67	55.67	-2.2	-3.4
1×10^7	0.08847	1.4533	1.1545	0.6784	1.7360	5.058	1.1844	0.6763	25.67	54.56	-2.2	-2.5
			1.1560	0.7124	1.8090	5.107	1.1802	0.6667	24.76	54.49	-2.3	-2.5
3×10^7	0.1402	1.4072	1.1231	0.6706	1.6743	5.866	1.1747	0.5425	17.07	53.75	-2.3	-2.1
			1.1325	0.7585	1.8581	5.979	1.1747	0.5162	16.01	53.65	-2.3	-2.1
1×10^8	0.2224	1.3730	1.1345	0.7049	1.5602	6.637	1.2230	0.4480	13.87	53.28	-2.2	-2.0
			1.1490	0.8169	1.7585	6.763	1.2263	0.4231	13.21	53.22	-2.2	-2.0
3×10^8	0.3302	1.3546	1.1933	0.8038	1.4675	7.362	1.2621	0.4002	12.71	52.97	-2.2	-1.9
			1.2030	0.8963	1.5991	7.456	1.2639	0.3858	12.38	52.94	-2.2	-1.9
1×10^9	0.5010	1.3437	1.3049	0.9954	1.3853	8.265	1.2898	0.3736	12.19	52.70	-2.1	-1.9
			1.3103	1.0688	1.4637	8.333	1.2905	0.3660	12.03	52.68	-2.1	-1.9
3×10^9	0.7274	1.3386	1.4475	1.2651	1.3260	9.247	1.3055	0.3660	12.11	52.51	-2.1	-1.9
			1.4505	1.3240	1.3729	9.297	1.3058	0.3620	12.03	52.50	-2.1	-1.9
5×10^9	0.8639	1.3372	1.5273	1.4288	1.3021	9.769	1.3107	0.3673	12.18	52.46	-2.1	-1.9

$$^a \gamma_0 = c_{s,0}^2 \rho_0 / P_0$$

$$^b \gamma^e = (c_s^e)^2 \rho / P$$

$$^c f_{\text{coul}} = \log_{10} \left(-\frac{\epsilon_{\text{coul}}}{\epsilon} \right)$$

$$^d f_{\text{ex}} = \log_{10} \left(\frac{\epsilon_{\text{ex}}}{\epsilon} \right)$$

the exponential mass formula of [Cameron & Elkin \(1965\)](#) was being used. Actually, the mass formula of [Cameron & Elkin \(1965\)](#) seems to be erroneous, so we apply a few corrections to it (see [Appendix D](#)). We assume that these correction were applied by [Bruenn \(1972\)](#) as well. Finally, the nuclear partition functions of [Clifford & Tayler \(1965\)](#) were used.

The results of our calculations with the same input physics of [Bruenn \(1972\)](#) are compared to the results of [Bruenn \(1972\)](#) in [Table 3](#) for a few representing upstream densities (compare rows ‘B72 setup’ to rows ‘B72’). The obtained P_{CJ} and ρ_{CJ} from our calculations are systematically larger than the results of [Bruenn \(1972\)](#) (by 9 – 22% and 7 – 20%, respectively), while $q_{01,\text{CJ}}$ is systematically lower (by 4 – 6%). We show below that the reason for this discrepancy is the NSE calculation and not the EOS. But first, let us compare the results obtained with the input physics of [Bruenn \(1972\)](#) to the calculation of the same initial conditions with our default input physics (the row ‘Default’), which highlights the sensitivity of the results to various assumptions. We concentrate on the $q_{01,\text{CJ}}$ values for $\rho_{0,7} = 500$ that shows the largest sensitivity. The value for the input physics of [Bruenn \(1972\)](#) deviates from the default input physics value by $\approx 19\%$. The Coulomb term of the NSE reduces the deviation to $\approx 13\%$ and the Coulomb term of the EOS reduces the deviation even further, to $\approx 9\%$. This demonstrates that the sensitivity of the result to the Coulomb corrections can reach as high as ten percent. Including the nuclear level excitations terms in the EOS (with the modern values of the partition functions) reduces the deviation to $\approx 1.6\%$, demonstrating the importance of these terms. The remaining discrepancy is reduced to $\approx 0.2\%$ by using the modern values for the partition functions instead of the nuclear partition functions of [Clifford & Tayler \(1965\)](#) for the calculation of the NSE.

We turn now to analyse the reason for the differences between the ‘B72 setup’ and ‘B72’ results. A somewhat simpler case to study is the NSE state at a some ρ , T , and Y_e with the same in-

put physics of [Bruenn \(1972\)](#), given in [Bruenn \(1971\)](#). We concentrate on the results with a neutron-proton ratio of 1 ($Y_e \approx 0.5$) from [table 1](#) of [Bruenn \(1971\)](#). The results of our calculations with the same input physics of [Bruenn \(1971\)](#) are compared to the results of [Bruenn \(1971\)](#) in [Table 4](#) (compare rows ‘B71 setup’ to rows ‘B71’). Although our pressure calculations agree with those of [Bruenn \(1971\)](#) to better than 0.5%, the obtained \bar{A} deviates at high temperatures by 5 – 10%. If we recalculate the pressure with the \bar{A} values of [Bruenn \(1971\)](#) (this only changes the small contributions of the ions), then the pressures agree to better than 1.5×10^{-3} . This result suggests that our EOS is consistent with the EOS used by [Bruenn \(1971\)](#). However, the different values of \bar{A} demonstrate that the NSE states are different, which lead to different CJ NSE states. As the code that was used to calculate the results of [Bruenn \(1971\)](#) was lost¹⁵, we were unable to identify the cause of this discrepancy.

4.1.2 Comparing CO CJ detonations to [Khokhlov \(1988\)](#)

[Khokhlov \(1988\)](#) calculated CJ detonations for CO, an upstream temperature of $T_{0,9} = 0.2$ and a few values of the upstream density in the range of $[10^7, 5 \times 10^9]$ g/cm³. We calculated the CJ NSE states for the same initial conditions by following the input physics of [Khokhlov \(1988\)](#). The difference between our Coulomb terms and those used by [Khokhlov \(1988\)](#) is smaller than a percent, and since the Coulomb corrections are a few percent at most, this difference can lead to deviations that are smaller than 10^{-3} . The list of isotopes included 83 isotopes, and we used the modern values of the binding energies and partition functions.

Our comparison of the results of our calculations with the same input physics of [Khokhlov \(1988\)](#) to those of [Khokhlov](#)

¹⁵ Stephen Bruenn, private communication.

Table 3. Parameters of CJ detonations for an initial composition of $X(^{12}\text{C}) = X(^{16}\text{O}) = 0.49$, $X(^{22}\text{Ne}) = 0.02$ and an upstream temperature of $T_{0,9} = 0.3$ for a few representing upstream densities. For each upstream density we present the results of Bruenn (1972) (B72), the results of our calculations with the same input physics of Bruenn (1972) (B72 setup), B72 setup with the addition of the Coulomb correction term for the NSE (B72 setup + Coul. NSE), the additional inclusion of the Coulomb correction terms for the EOS (B72 setup + Coul. NSE + Coul. EOS), the additional inclusion of the nuclear level excitations terms in the EOS (using the modern values of the partition functions, B72 setup + Coul. NSE + Coul. EOS + ε_{ex}), and by further using the modern values for the partition functions instead of the nuclear partition functions of Clifford & Taylor (1965) for the calculation of the NSE (B72 setup + Coul. NSE + Coul. EOS + ε_{ex} + part.). The upper rows for each upstream density are the results with our default input physics.

ρ_0 [g/cm ³]	Case	P_{CJ}/P_0	ρ_{CJ}/ρ_0	T_{CJ} [10 ⁹ K]	$q_{01,\text{CJ}}$ [10 ¹⁷ erg/g]
5×10^6	Default	10.23	1.727	4.472	7.290
	B72 setup + Coul. NSE + Coul. EOS + ε_{ex} + part.	10.23	1.726	4.473	7.299
	B72 setup + Coul. NSE + Coul. EOS + ε_{ex}	10.22	1.725	4.471	7.293
	B72 setup + Coul. NSE + Coul. EOS	10.22	1.724	4.472	7.292
	B72 setup + Coul. NSE	10.08	1.723	4.468	7.297
	B72 setup	10.08	1.726	4.467	7.271
	B72	8.058	1.411	4.265	7.720
2×10^8	Default	2.654	1.500	7.107	3.975
	B72 setup + Coul. NSE + Coul. EOS + ε_{ex} + part.	2.653	1.500	7.106	3.974
	B72 setup + Coul. NSE + Coul. EOS + ε_{ex}	2.646	1.499	7.080	3.937
	B72 setup + Coul. NSE + Coul. EOS	2.660	1.500	7.104	3.844
	B72 setup + Coul. NSE	2.633	1.498	7.113	3.800
	B72 setup	2.611	1.496	7.025	3.712
	B72	2.280	1.338	6.970	3.890
5×10^9	Default	1.653	1.302	9.801	3.519
	B72 setup + Coul. NSE + Coul. EOS + ε_{ex} + part.	1.653	1.302	9.799	3.518
	B72 setup + Coul. NSE + Coul. EOS + ε_{ex}	1.650	1.301	9.725	3.462
	B72 setup + Coul. NSE + Coul. EOS	1.666	1.305	9.823	3.213
	B72 setup + Coul. NSE	1.647	1.300	9.868	3.080
	B72 setup	1.628	1.295	9.497	2.902
	B72	1.492	1.210	9.414	3.017

Table 4. The NSE state for a few values of ρ , T , and $Y_e = 0.5$. For each case, we present the results of Bruenn (1971) (B71), the results of our calculations with the same input physics of Bruenn (1971) (B71 setup), and the results of recalculating the pressure with the \bar{A} values of Bruenn (1971) (B71 setup + B71 \bar{A}).

ρ [g/cm ³]	T [10 ⁹ K]	Case	P [erg/cm ³]	\bar{A}
1×10^7	6	B71 setup	9.423×10^{24}	6.963
		B71 setup + B71 \bar{A}	9.459×10^{24}	6.634
		B71	9.461×10^{24}	6.634
1×10^8	3	B71 setup	2.507×10^{25}	55.93
		B71 setup + B71 \bar{A}	2.507×10^{25}	55.98
		B71	2.511×10^{25}	55.98
1×10^8	7	B71 setup	4.972×10^{25}	7.609
		B71 setup + B71 \bar{A}	4.980×10^{25}	7.527
		B71	4.983×10^{25}	7.527
2×10^8	3	B71 setup	1.262×10^{27}	55.97
		B71 setup + B71 \bar{A}	1.262×10^{27}	55.64
		B71	1.262×10^{27}	55.64
2×10^9	8	B71 setup	1.476×10^{27}	14.41
		B71 setup + B71 \bar{A}	1.468×10^{27}	15.69
		B71	1.470×10^{27}	15.69

(1988) in Table 5 (i.e., comparison of rows ‘K88 setup’ to rows ‘K88’) reveals large deviations at low densities (up to 13% in $q_{01,\text{CJ}}$, for example). We show below that the reason for the discrepancy is an erroneous EOS used by Khokhlov (1988). Before we do so, we compare the results obtained with the input physics

of Khokhlov (1988) to the calculation of the same initial conditions with our default input physics (the row ‘Default’). The $q_{01,\text{CJ}}$ values for the input physics of Khokhlov (1988) deviate from the default input physics value by 1 – 6%. The Coulomb term for the NSE reduces the deviation to below 10^{-3} . This once again demon-

strates that the sensitivity of the result to the Coulomb correction is on the order of a few percent.

In order to analyse the reason for the differences between ‘K88 setup’ and the ‘K88’ results, we calculate the pressure $q_{01,CJ}$ at the NSE state for the values of ρ_{CJ} and T_{CJ} as given by Khokhlov (1988). The results of our calculations with the input physics of Khokhlov (1988) are compared to the results of Khokhlov (1988) in Table 6 (compare rows ‘K88 setup’ to ‘K88’). The values of $q_{01,CJ}$ usually deviate by less than $\approx 2\%$ (for $\rho_{0,7} = 300$ a deviation of $\approx 5\%$ is obtained), which suggests that the compositions of the NSE states are similar. However, the deviations in the pressures are large for low densities and reach $\approx 10\%$ for $\rho_{0,7} = 1$. Since the agreement between the Nadyozhin (1988) electron-positron EOS used by Khokhlov (1988) and the EOS by us is better than 0.1% (Timmes & Arnett 1999), the difference is probably because of some numerical bug. In fact, the difference between the pressures is almost exactly the radiation pressure (compare rows ‘K88 setup + twice p_{rad} ’ to rows ‘K88’), which suggests that Khokhlov (1988) erroneously used the radiation term to calculate the pressure. We conclude that the reason for the discrepancy is an error in the EOS used by Khokhlov (1988)¹⁶.

4.1.3 Comparing CO CJ detonations to Gamezo et al. (1999)

Gamezo et al. (1999) calculated CJ detonations for CO, an upstream temperature of $T_{0,9} = 0.2$ and a few values of the upstream density in the range of $[3 \times 10^5, 3 \times 10^9] \text{ g/cm}^3$. The list of isotopes included 13 α -nuclei, and Coulomb corrections were probably not included. We calculate the CJ NSE states for the same initial conditions by following the input physics of Gamezo et al. (1999). We use the modern values of the binding energies and partition functions.

The results of our calculations with the same input physics of Gamezo et al. (1999) are compared to the results of Gamezo et al. (1999) in Figure 5 (compare the black lines to the blue lines) and in Table 7 (compare rows ‘G99 setup’ to rows ‘G99’). The general behaviour of both D_{CJ} and $q_{01,CJ}$ is similar. Deviations of up to $\approx 2\%$ are obtained in D_{CJ} and large deviations are obtained at high densities in $q_{01,CJ}$ ($\approx 7\%$ for $\rho_{0,7} = 100$). Below, we try to analyse the reason for the discrepancy.

First, it is not clear how the CJ values were actually calculated by Gamezo et al. (1999), since they claim to integrate the reaction equations to obtain the CJ values. Besides the fact that this is not required, as the CJ values are independent of reaction rates, it is also not possible for pathological detonations, as the integration hits a sonic point for $D < D_*$. Let us now concentrate on the $\rho_{0,7} = 1$ case, where we obtain a similar $q_{01,CJ}$ but a lower D_{CJ} . We find from the upper panel of figure 3 of Gamezo et al. (1999) that $u_{CJ} \approx 0.68 \times 10^4 \text{ km/s}$ and that $c_{s,CJ} \approx 0.75 \times 10^4 \text{ km/s}$. With these u_{CJ} and D_{CJ} figures, we get from Equation (2) that $\rho_{CJ,7} \approx 1.79$. We can now use our EOS (without the Coulomb correction) to find T_{CJ} in two ways. For the value of $c_{s,CJ}$, we find that $T_{CJ,9} \approx 5.31$, and for the value of u_{CJ} , we find that $T_{CJ,9} \approx 5.10$. This discrepancy demonstrates that the calculation of Gamezo et al. (1999) is inconsistent.

¹⁶ Ironically, Khokhlov (1988) claims that the discrepancy between his results and the results of Bruenn (1972) at low densities is because of the approximate EOS used by Bruenn (1972), while, in fact, the EOS used by Bruenn (1972) is accurate and the one used by Khokhlov (1988) is erroneous.

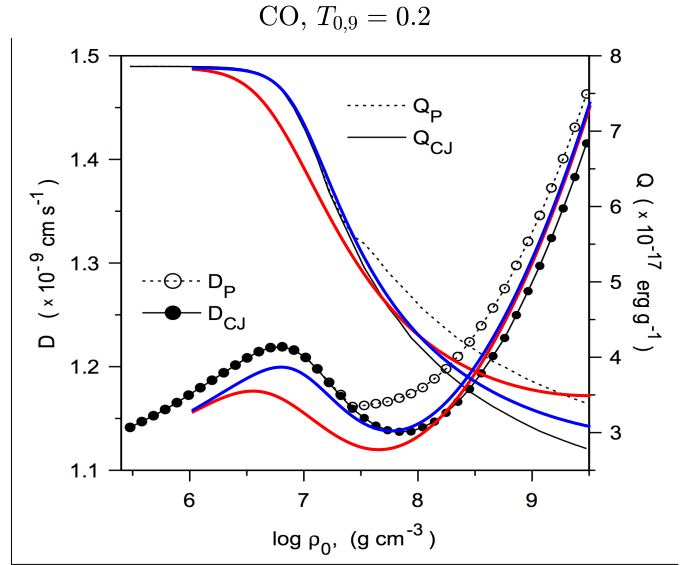


Figure 5. Figure 2 from Gamezo et al. (1999) (© AAS. Reproduced with permission). D_{CJ} and $q_{01,CJ}$ for CO and $T_{0,9} = 0.2$ as a function of the upstream density. Black lines represent the results of Gamezo et al. (1999), blue lines are our results with the input physics of Gamezo et al. (1999), and red lines reflect results with our default input physics.

Because of these unresolved discrepancies, we did not try to reproduce the results of Gamezo et al. (1999) for the pathological case. We will just mention here that the $q_{01,*}$ values presented in figure 2 of Gamezo et al. (1999) seem to be erroneous. Our calculations always yield a $q_{01,*} < q_{01,CJ}$. This is because at higher detonation speeds the temperature of the NSE state is higher and, therefore, more ^4He nuclei are present, which decreases q_{01} . The results of Gamezo et al. (1999) are the complete opposite, $q_{01,*} > q_{01,CJ}$, which is hard to understand. Moreover, from figure 2 of Gamezo et al. (1999) we can extract $q_{01,*} \approx 4.70 \times 10^{17} \text{ erg/g}$ for $\rho_{0,7} = 10$, while from the bottom panel of figure 3 of Gamezo et al. (1999) we find that $q_{01,*} \approx 3.57 \times 10^{17} \text{ erg/g}$ for the same ρ_0 .

Let us go back now to Table 7 and compare the results obtained with the input physics of Gamezo et al. (1999) to the calculation with our default input physics (the row ‘Default’; compare also the blue and the red lines in Figure 5). The $q_{01,CJ}$ values for the input physics of Gamezo et al. (1999) deviate from the default input physics values by up to $\approx 9\%$. The Coulomb terms and the nuclear level excitations terms change the values of $q_{01,CJ}$ by up to a few percent each. Finally, extending the isotope list to our default list changes the values of $q_{01,CJ}$ by $\approx 2 - 9\%$. The reason for this alteration is that α -nuclei cannot correctly represent the NSE state, as a significant fraction of the mass can be stored in different isotopes (see bottom panel of Figure 4). This inability is compensated for by artificially increasing the mass fractions of all the elements with a $Z_i \geq 14$, especially ^{56}Ni and ^{52}Fe . For this reason, calculations with α -nuclei are inadequate for the accurate analysis that we aim for in this work.

4.2 CJ detonations of pure Helium

The calculated D_{CJ} for He is presented in the upper panel of Figure 6 for an upstream temperature of $T_{0,9} = 0.2$ and an upstream density in the relevant range for supernovae of $[10^4, 10^8] \text{ g/cm}^3$.

Table 5. Parameters of CJ detonations for CO and an upstream temperature of $T_{0,9} = 0.2$ for a few upstream densities. For each upstream density, we present the results of [Khokhlov \(1988\)](#) (K88), the results of our calculations with the same input physics as that used by [Khokhlov \(1988\)](#) (K88 setup) and by adding the Coulomb correction term for the NSE (K88 setup + Coul. NSE). The upper rows for each upstream density are the results obtained with our default input physics.

ρ_0 [g/cm ³]	Case	P_{CJ}/P_0	ρ_0/ρ_{CJ}	T_{CJ} [10 ⁹ K]	$q_{01,\text{CJ}}$ [10 ¹⁷ erg/g]	γ_{CJ}^e	D_{CJ} [10 ⁴ km/s]
1×10^7	Default	7.668	0.5760	5.058	6.478	1.1844	1.1545
	K88 setup + Coul. NSE	7.675	0.5756	5.059	6.477	1.1843	1.1546
	K88 setup	7.656	0.5749	5.049	6.430	1.1810	1.1518
	K88	7.95	0.59	4.73	7.10	1.23	1.19
3×10^7	Default	4.782	0.5973	5.866	5.197	1.1747	1.1231
	K88 setup + Coul. NSE	4.782	0.5973	5.866	5.197	1.1747	1.1232
	K88 setup	4.756	0.5970	5.838	5.131	1.1731	1.1190
	K88	5.15	0.59	5.60	5.84	1.18	1.16
1×10^8	Default	3.169	0.6409	6.637	4.291	1.2230	1.1345
	K88 setup + Coul. NSE	3.168	0.6412	6.637	4.292	1.2230	1.1345
	K88 setup	3.146	0.6415	6.578	4.214	1.2224	1.1294
	K88	3.33	0.63	6.47	4.67	1.21	1.16
3×10^8	Default	2.434	0.6814	7.362	3.833	1.2621	1.1933
	K88 setup + Coul. NSE	2.435	0.6813	7.362	3.833	1.2621	1.1934
	K88 setup	2.415	0.6825	7.261	3.740	1.2617	1.1873
	K88	2.49	0.68	7.18	4.02	1.25	1.21
1×10^9	Default	1.987	0.7219	8.265	3.578	1.2898	1.3049
	K88 setup + Coul. NSE	1.987	0.7218	8.264	3.578	1.2899	1.3051
	K88 setup	1.970	0.7233	8.093	3.454	1.2895	1.2974
	K88	2.01	0.72	8.05	3.59	1.28	1.31
3×10^9	Default	1.739	0.7542	9.247	3.505	1.3055	1.4475
	K88 setup + Coul. NSE	1.740	0.7541	9.246	3.505	1.3056	1.4479
	K88 setup	1.723	0.7566	8.972	3.338	1.3053	1.4384
	K88	1.75	0.75	8.95	3.59	1.30	1.45
5×10^9	Default	1.654	0.7680	9.769	3.518	1.3107	1.5273
	K88 setup + Coul. NSE	1.654	0.7681	9.768	3.518	1.3108	1.5279
	K88 setup	1.639	0.7704	9.430	3.322	1.3106	1.5175
	K88	1.66	0.77	9.45	3.35	1.30	1.53

Similarly to [Dunkley et al. \(2013\)](#), we find that D_{CJ} is not a monotonic function of ρ_0 and that it has a minimum at $\rho_{0,7} \approx 4.5 \times 10^{-3}$ and a maximum at $\rho_{0,7} \approx 0.16$. There is another minimum at $\rho_{0,7} \approx 7$, which can also be extracted from table IV of [Khokhlov \(1988\)](#). Key isotopes at the CJ NSE state are presented in the bottom panel of Figure 6 for the same upstream values. We only present the mass fraction of isotopes that have a mass fraction larger than 5×10^{-2} at some ρ_0 within the inspected range. At low densities, the NSE state is dominated by ^{56}Ni (with $\bar{A} \approx \tilde{A} \approx 56$ at $\rho_{0,7} = 10^{-3}$), while at higher densities the NSE state is mainly a mixture of ^4He , ^{54}Fe , ^{55}Fe and ^{56}Fe (with $\bar{A} \approx 6.5$, $\tilde{A} \approx 53$ at $\rho_{0,7} = 10$). A few key parameters of these CJ detonations are given in Table 8. The temperature at the CJ NSE state increases monotonically with ρ_0 , which decreases both the \bar{A} at these states and the released thermonuclear energy compared with the initial states, $q_{01,\text{CJ}}$. It is also demonstrated that the nuclear excitation energy contribution to the energy at the NSE state can reach one percent for the high densities, and becomes much larger in magnitude than the Coulomb correction.

The results do not depend much on the initial upstream tem-

perature. The D_{CJ} values for $T_{0,9} = 0.01^{17}$ deviate from the results for $T_{0,9} = 0.2$ by less than 2×10^{-3} , and the key parameters of Table 2 deviate by less than 8.5×10^{-3} , where the largest deviation is obtained for $q_{01,\text{CJ}}$ at $\rho_{0,7} = 10$.

The results calculated with the NSE4 (NSE5, NSE7Si) isotope list deviate from the results presented above by less than 2.5×10^{-3} (2×10^{-4} , 3×10^{-8}), which suggests that our isotope list is converged to $\sim 10^{-3}$. The most uncertain input physics in this calculation is the Coulomb corrections. The contribution of the Coulomb energy to the initial state energy is of the order of a few percent (highest contribution for the lowest densities), with a smaller contribution obtained at the NSE state (see Table 8). The Coulomb interaction terms change the NSE composition in the order of a few percent as well (see Section 4.2.2). We, therefore, estimate the uncertainty of the results to be on the sub-percent level (see Section 3.4).

4.2.1 Comparing He CJ detonations to [Mazurek \(1973b\)](#)

[Mazurek \(1973b\)](#) calculated CJ detonations for He, an upstream

¹⁷ The electron-electron term is neglected here, and the correction is in the range of a few percent for $\rho_{0,7} \lesssim 0.027$, $T_{0,9} = 0.01$.

Table 6. The pressure and $q_{01,CJ}$ at the NSE state for the values of ρ_{CJ} and T_{CJ} as given by [Khokhlov \(1988\)](#) for CO. For each case, we present the results of [Khokhlov \(1988\)](#) (K88), the results of our calculations with the same input physics of [Khokhlov \(1988\)](#) (K88 setup), and the results of recalculating the pressure with twice the radiation pressure (K88 setup + twice p_{rad}).

ρ_0 [g/cm ³]	Case	P_{CJ}/P_0^{K88}	$q_{01,CJ}$ [10 ¹⁷ erg/g]
1×10^7	K88 setup	6.46	7.08
	K88 setup + twice p_{rad}	7.95	
	K88	7.95	7.10
3×10^7	K88 setup	4.46	5.90
	K88 setup + twice p_{rad}	5.08	
	K88	5.15	5.84
1×10^8	K88 setup	3.14	4.64
	K88 setup + twice p_{rad}	3.34	
	K88	3.33	4.67
3×10^8	K88 setup	2.40	4.03
	K88 setup + twice p_{rad}	2.47	
	K88	2.49	4.02
1×10^9	K88 setup	1.97	3.60
	K88 setup + twice p_{rad}	1.99	
	K88	2.01	3.59
3×10^9	K88 setup	1.74	3.41
	K88 setup + twice p_{rad}	1.75	
	K88	1.75	3.59
5×10^9	K88 setup	1.64	3.28
	K88 setup + twice p_{rad}	1.65	
	K88	1.66	3.35

Table 7. Parameters of CJ detonations for CO and upstream temperature of $T_{0,9} = 0.2$ for a few upstream densities. For each upstream density we present the results of [Gamezo et al. \(1999\)](#) (G99), the results of our calculations with the same input physics of [Gamezo et al. \(1999\)](#) (G99 setup), the G99 setup with the addition of the Coulomb correction term for the NSE (G99 setup + Coul. NSE), and the additional inclusion of the Coulomb correction term for the EOS (G99 setup + Coul. NSE + Coul. EOS), and also the addition of the nuclear level excitations (G99 setup + Coul. NSE + Coul. EOS + ϵ_{ex}). The upper rows for each upstream density are the results with our default input physics.

ρ_0 [g/cm ³]	Case	$q_{01,CJ}$ [10 ¹⁷ erg/g]	D_{CJ} [10 ⁴ km/s]
1×10^7	Default	6.478	1.155
	G99 setup + Coul. NSE + Coul. EOS + ϵ_{ex}	7.118	1.192
	G99 setup + Coul. NSE + Coul. EOS	7.113	1.193
	G99 setup + Coul. NSE	7.120	1.195
	G99 setup	7.059	1.192
	G99	7.03	1.21
1×10^8	Default	4.291	1.134
	G99 setup + Coul. NSE + Coul. EOS + ϵ_{ex}	4.467	1.151
	G99 setup + Coul. NSE + Coul. EOS	4.427	1.153
	G99 setup + Coul. NSE	4.396	1.154
	G99 setup	4.290	1.146
	G99	4.17	1.14
1×10^9	Default	3.578	1.305
	G99 setup + Coul. NSE + Coul. EOS + ϵ_{ex}	3.650	1.315
	G99 setup + Coul. NSE + Coul. EOS	3.542	1.319
	G99 setup + Coul. NSE	3.459	1.320
	G99 setup	3.310	1.309
	G99	3.08	1.28

Table 8. Key parameters of CJ detonations for He and upstream temperature of $T_{0,9} = 0.2$.

ρ_0 [g/cm ³]	P_0/ρ_0 [MeV/ m_p]	γ_0^a	D_{CJ} [10 ⁴ km/s]	P_{CJ}/ρ_0 [MeV/ m_p]	ρ_{CJ}/ρ_0	T_{CJ} [10 ⁹ K]	$\gamma_{\text{CJ}}^e{}^b$	$q_{01,\text{CJ}}$ [MeV/ m_p]	\bar{A}_{CJ}	\tilde{A}_{CJ}	f_{coul}^c	f_{ex}^d
1×10^4	0.01373	1.5967	1.4948	1.0459	1.7937	1.341	1.2448	1.5803	56.00	56.00	-3.2	-10.5
3×10^4	0.01404	1.6178	1.4731	1.0070	1.7804	1.689	1.2659	1.5803	56.00	56.00	-3.1	-8.4
1×10^5	0.01590	1.6211	1.4776	0.9977	1.7566	2.180	1.3006	1.5803	55.99	56.00	-2.9	-6.6
3×10^5	0.02075	1.6082	1.5018	1.0222	1.7400	2.776	1.3255	1.5797	55.77	55.98	-2.7	-5.3
1×10^6	0.03312	1.5718	1.5342	1.0737	1.7346	3.653	1.3213	1.5656	50.12	55.81	-2.6	-4.0
3×10^6	0.05443	1.5201	1.5251	1.1194	1.7812	4.684	1.2203	1.4462	26.54	54.80	-2.7	-2.9
1×10^7	0.09261	1.4585	1.4304	1.0650	1.8357	5.860	1.0939	1.1083	11.44	53.75	-2.9	-2.3
3×10^7	0.1449	1.4116	1.3430	0.9588	1.7614	6.753	1.1151	0.8232	7.78	53.58	-2.9	-2.1
1×10^8	0.2279	1.3764	1.3269	0.9421	1.6356	7.666	1.1932	0.6564	6.57	53.35	-2.8	-2.0

$$^a \gamma_0 = c_{s,0}^2 \rho_0 / P_0$$

$$^b \gamma_{\text{CJ}}^e = \left(c_{s,\text{CJ}}^e \right)^2 \rho_{\text{CJ}} / P_{\text{CJ}}$$

$$^c f_{\text{coul}} = \log_{10} \left(-\frac{\epsilon_{\text{coul}}}{\epsilon} \right) \text{ at the CJ state}$$

$$^d f_{\text{ex}} = \log_{10} \left(\frac{\epsilon_{\text{ex}}}{\epsilon} \right) \text{ at the CJ state}$$

temperature of $T_0 = 0.05$ and a few values of the upstream density in the range of $[10^6, 5 \times 10^9] \text{ g/cm}^3$. The details of the input physics used by Mazurek (1973b) are given in Mazurek (1973a) and includes a list of 155 isotopes without Coulomb correction terms nor the nuclear-level excitation. The source for the values of the binding energies and partition functions is not given, so we use the modern values. We calculate the CJ NSE states for the same initial conditions of Mazurek (1973b) by following the input physics described above (M73 setup hereafter). The results of our calculations are compared to the results of Mazurek (1973b) in Table 9 (compare rows ‘M73 setup’ to rows ‘M73’). Large deviations are obtained at low densities (up to 11% in ρ_{CJ}/ρ_0 , for example). In these cases ($0.1 \leq \rho_{0,7} \leq 1$), our calculated D_{CJ} is significantly lower (by up to 10%) than the values of Mazurek (1973b).

In order to analyse the reason for the discrepancy, we calculate the pressure, $q_{01,\text{CJ}}$, the electron-positron pressure and the electron-positron energy at the NSE state for the values of ρ_{CJ} and T_{CJ} as given by Mazurek (1973b). The results of our calculations with the M73 setup are compared to the results of Mazurek (1973b) in Table 10 (compare rows ‘M73 setup’ to rows ‘M73’). In order to calculate the electron-positron terms for M73, we assume that the CJ conditions hold and we use the analytical terms for the radiation and the ions (with the M73 setup values for \bar{A}). The values of $q_{01,\text{CJ}}$ deviate by less than $\approx 5\%$, which suggests that the compositions of the NSE states are similar, and the difference between the pressure levels is below $\approx 1\%$, which suggests that our pressure calculation is consistent with the one used by Mazurek (1973b). Indeed, when we directly compare the electron-positron pressures, the deviation is smaller than 1.5%, which also suggests that the deviation in \bar{A} is small. However, the electron-positron energies deviate by up to 33%, with the largest deviation obtained for $\rho_{0,7} = 0.1$. We believe that this is because of inaccuracies in the EOS used by Mazurek (1973b) for the high positron-to-proton ratio, n_+/n_p . Mazurek (1973a) admits that his EOS becomes less accurate in higher n_+/n_p , although the error is estimated to be $\sim 10^{-4}$ for $n_+/n_p \approx 10$, where even for $\rho_{0,7} = 0.1$ we only have $n_+/n_p \approx 0.68$ (see Table 10). Mazurek (1973a) estimated the level of accuracy of his EOS by comparing it to Table A.4.1 in Appendix A.4 of Cox & Giuli (1968), and he claimed that his results match exactly the results there, except for regions with $n_+/n_p > 50$ (there are re-

ally only 3 entries with $n_+/n_p > 50$ in the tables of Cox & Giuli (1968)). We can verify almost directly in the case $\rho_{0,7} = 1$ that the results of Mazurek (1973b) are not accurate. This is done by using the following values; $\rho_{\text{CJ},7}/\mu_e = 0.82$ ($\mu_e = 2$) and $T_{\text{CJ},9} = 5.81$ as given by Mazurek (1973b) with similar values to the entries $\eta = 0$, $\beta = 0$ ($T_9 \approx 5.93$) and $\rho_m/\mu_e = 9.243 \times 10^6 \text{ g/cm}^3$ in the tables of Cox & Giuli (1968). There we find $p_{ep}/\epsilon_{ep}\rho = 0.3787$, which does not seem to change too much for $\sim 10\%$ changes in T and ρ . Comparing this to the M73 setup value (≈ 0.38) and to the M73 value (≈ 0.46) suggests that the electron-positron energy terms are not accurately calculated by Mazurek (1973b).

We also compare the results obtained with the M73 setup to the calculation of the same initial conditions but with our default input physics (the row ‘Default’ in Table 9). The $q_{01,\text{CJ}}$ values for the M73 setup deviate from the default input physics value at high densities by up to $\approx 7\%$. The Coulomb correction term for the NSE reduces the deviation to less than 4%, and the Coulomb correction term for the EOS reduces it further to below 3%.

4.2.2 Comparing He CJ detonations to Khokhlov (1988)

Khokhlov (1988) calculated CJ detonations for He, an upstream temperature of $T_0 = 0.1$ and a few values of the upstream density in the range of $[10^6, 10^9] \text{ g/cm}^3$. We calculated the CJ NSE states for the same initial conditions by following the input physics of Khokhlov (1988). The results of our calculations with the same input physics of Khokhlov (1988) are compared to the results of Khokhlov (1988) in Table 11 (compare rows ‘K88 setup’ to rows ‘K88’). Large deviations are obtained (up to 15% in $q_{01,\text{CJ}}$, for example). We showed in Section 4.1.2 that the EOS used by Khokhlov (1988) is erroneous, to which we attribute the differences between the results. We verified this again by calculating the pressure and $q_{01,\text{CJ}}$ at the NSE state for the values of ρ_{CJ} and T_{CJ} as given by Khokhlov (1988). The results of our calculations with the same input physics of Khokhlov (1988) are compared to the results of Khokhlov (1988) in Table 12 (compare rows ‘K88 setup’ to rows ‘K88’). The values of $q_{01,\text{CJ}}$ deviate by less than $\approx 1\%$, which suggests that the compositions of the NSE states are similar. However, the deviation in the pressure levels are large for low densities and reach $\approx 37\%$ for $\rho_{0,7} = 0.1$. Once again, the difference between the

Table 9. Parameters of CJ detonations for He and upstream temperature of $T_{0,9} = 0.05$ for a few upstream densities. For each upstream density, we present the results of Mazurek (1973b) (M73), the results of our calculations with the M73 setup (M73 setup), M73 setup with the addition of the Coulomb correction term to the NSE (M73 setup + Coul. NSE) and with the further addition of the Coulomb correction term to the EOS (M73 setup + Coul. NSE + Coul. EOS). The upper rows for each upstream density are the results obtained with our default input physics.

ρ_0 [g/cm ³]	Case	P_{CJ}/P_0	ρ_{CJ}/ρ_0	T_{CJ} [10 ⁹ K]	$q_{01,\text{CJ}}$ [10 ¹⁷ erg/g]	D_{CJ} [10 ⁴ km/s]
1×10^6	Default	37.786	1.7385	3.651	14.998	1.5339
	M73 setup + Coul. NSE + Coul. EOS	37.780	1.7381	3.651	14.998	1.5340
	M73 setup + Coul. NSE	37.476	1.7379	3.649	14.999	1.5344
	M73 setup	37.459	1.7376	3.649	14.994	1.5342
	M73	39.00	1.56	3.69	15.01	1.70
5×10^6	Default	17.191	1.8145	5.193	12.671	1.4936
	M73 setup + Coul. NSE + Coul. EOS	17.200	1.8120	5.194	12.664	1.4953
	M73 setup + Coul. NSE	17.090	1.8115	5.193	12.667	1.4958
	M73 setup	17.074	1.8156	5.190	12.596	1.4931
	M73	16.90	1.64	5.22	12.95	1.59
1×10^7	Default	11.979	1.8387	5.857	10.639	1.4310
	M73 setup + Coul. NSE + Coul. EOS	11.987	1.8346	5.860	10.616	1.4335
	M73 setup + Coul. NSE	11.935	1.8367	5.861	10.609	1.4340
	M73 setup	11.898	1.8415	5.849	10.499	1.4293
	M73	11.10	1.64	5.81	10.84	1.49
5×10^7	Default	5.423	1.7101	7.135	7.095	1.3270
	M73 setup + Coul. NSE + Coul. EOS	5.439	1.7095	7.145	7.024	1.3298
	M73 setup + Coul. NSE	5.414	1.7097	7.146	7.011	1.3303
	M73 setup	5.365	1.7084	7.096	6.893	1.3235
	M73	5.16	1.64	7.07	6.95	1.33
1×10^8	Default	4.206	1.6394	7.661	6.327	1.3287
	M73 setup + Coul. NSE + Coul. EOS	4.221	1.6394	7.675	6.241	1.3317
	M73 setup + Coul. NSE	4.198	1.6381	7.677	6.226	1.3321
	M73 setup	4.162	1.6374	7.604	6.104	1.3250
	M73	4.16	1.63	7.60	6.07	1.33
5×10^8	Default	2.788	1.5095	9.017	5.478	1.4210
	M73 setup + Coul. NSE + Coul. EOS	2.802	1.5111	9.044	5.344	1.4252
	M73 setup + Coul. NSE	2.788	1.5096	9.048	5.314	1.4257
	M73 setup	2.761	1.5069	8.899	5.177	1.4171
	M73	2.75	1.50	8.87	5.16	1.42
1×10^9	Default	2.459	1.4652	9.698	5.342	1.4913
	M73 setup + Coul. NSE + Coul. EOS	2.471	1.4663	9.732	5.179	1.4964
	M73 setup + Coul. NSE	2.460	1.4652	9.739	5.140	1.4969
	M73 setup	2.435	1.4621	9.542	4.988	1.4875
	M73	2.42	1.46	9.50	4.98	1.49

pressure levels is almost exactly the radiation pressure (compare rows ‘K88 setup + twice p_{rad} ’ to rows ‘K88’), which suggests that Khokhlov (1988) erroneously used the radiation term twice.

We also compare the results obtained with the input physics of Khokhlov (1988) to the calculation of the same initial conditions but with our default input physics (the row ‘Default’ in Table 11). The $q_{01,\text{CJ}}$ values for the input physics of Khokhlov (1988) deviate from the default input physics value by up to $\approx 3\%$. The Coulomb correction term for the NSE reduces the deviation to below 2.5×10^{-3} .

It is interesting to note that Townsley et al. (2012) calculated the D_{CJ} for He, $\rho_{0,7} = 0.5$, $T_{0,9} = 0.2$, by using the *Helmholtz* EOS and the 13 α -element network. They claim that their value, 1.54×10^4 km/s, is consistent with the results of Khokhlov (1988), as they interpolate between the entries $\rho_{0,7} = 0.3$ and $\rho_{0,7} = 1$ of Table 11. We verified that this is in fact a coincidence, because

the erroneous EOS of Khokhlov (1988) compensates for the difference between the input physics of Townsley et al. (2012) and of Khokhlov (1988).

5 THE STRUCTURE OF THE DETONATION WAVE

In this section, we present our calculation of the structure of the (possibly pathological) detonation waves. For a given detonation speed, in which the final state is NSE (and the solution does not cross the sonic point), the end state is known in advance and is independent of the reaction rates. We use this fact to monitor the numerical accuracy of the integration. Another useful method is to monitor the energy conservation during the integration, which allows us to estimate that our numerical accuracy is better than 10^{-3} . The numerical integration is performed with a 4th-order implicit

Table 10. The pressure, $q_{01,\text{CJ}}$, the electron-positron pressure and the electron-positron energy at the NSE state for the values of ρ_{CJ} and T_{CJ} as given by Mazurek (1973b). In order to calculate the electron-positron terms for M73, we assume that the CJ conditions hold and we use the analytical terms for the radiation and the ions (with M73 setup values for \bar{A}). For each case, we present the results of Mazurek (1973b) (M73), and the results of our calculations with the M73 setup. We also present the positron-to-proton ratio, n_+/n_p , as calculated for the M73 setup.

ρ_0 [g/cm ³]	Case	$P_{\text{CJ}}/P_0^{\text{M73}}$	$q_{01,\text{CJ}}$ [10 ¹⁷ erg/g]	$p_{ep,\text{CJ}}$ [MeV/ m_p]	$\varepsilon_{ep,\text{CJ}}$ [MeV/ m_p]	$(n_+/n_p)_{\text{CJ}}$
1×10^6	M73 setup	38.67	14.96	0.39	1.21	6.82×10^{-1}
	M73	39.00	15.01	0.40	0.87	
5×10^6	M73 setup	17.00	12.33	0.41	1.13	3.56×10^{-1}
	M73	16.90	12.95	0.40	0.94	
1×10^7	M73 setup	11.13	10.45	0.38	1.00	2.02×10^{-1}
	M73	11.10	10.84	0.38	0.90	
5×10^7	M73 setup	5.16	6.88	0.38	0.95	2.90×10^{-2}
	M73	5.16	6.95	0.38	0.93	
1×10^8	M73 setup	4.15	6.08	0.42	1.06	1.01×10^{-2}
	M73	4.16	6.07	0.42	1.05	
5×10^8	M73 setup	2.74	5.26	0.58	1.53	6.81×10^{-4}
	M73	2.75	5.16	0.58	1.53	
1×10^9	M73 setup	2.42	5.12	0.69	1.85	1.79×10^{-4}
	M73	2.42	4.98	0.69	1.86	

Table 11. Parameters of CJ detonations for He and an upstream temperature of $T_{0,9} = 0.1$ for a few upstream densities. For each upstream density we present the results of Khokhlov (1988) (K88), the results of our calculations with the same input physics of Khokhlov (1988) (K88 setup), and K88 setup with the addition of the Coulomb correction term to the NSE (K88 setup + Coul. NSE). The upper rows for each upstream density are the results obtained with our default input physics.

ρ_0 [g/cm ³]	Case	P_{CJ}/P_0	ρ_0/ρ_{CJ}	T_{CJ} [10 ⁹ K]	$q_{01,\text{CJ}}$ [10 ¹⁷ erg/g]	γ_{CJ}^e	D_{CJ} [10 ⁴ km/s]
1×10^6	Default	35.989	0.5759	3.651	14.997	1.3214	1.5340
	K88 setup + Coul. NSE	35.996	0.5758	3.651	14.997	1.3214	1.5340
	K88 setup	36.005	0.5756	3.652	14.993	1.3208	1.5338
	K88	36.80	0.58	3.33	15.10	1.31	1.56
3×10^6	Default	21.671	0.5606	4.682	13.858	1.2204	1.5251
	K88 setup + Coul. NSE	21.659	0.5609	4.682	13.860	1.2204	1.5251
	K88 setup	21.658	0.5600	4.681	13.818	1.2175	1.5235
	K88	22.60	0.57	4.34	14.50	1.26	1.57
1×10^7	Default	11.815	0.5443	5.857	10.633	1.0942	1.4308
	K88 setup + Coul. NSE	11.819	0.5441	5.858	10.632	1.0944	1.4308
	K88 setup	11.769	0.5433	5.844	10.527	1.0906	1.4262
	K88	12.80	0.55	5.56	12.00	1.14	1.50
3×10^7	Default	6.735	0.5668	6.751	7.906	1.1154	1.3438
	K88 setup + Coul. NSE	6.733	0.5671	6.752	7.913	1.1162	1.3441
	K88 setup	6.682	0.5670	6.716	7.791	1.1148	1.3378
	K88	7.34	0.57	6.53	9.09	1.11	1.41
1×10^8	Default	4.182	0.6105	7.663	6.314	1.1933	1.3281
	K88 setup + Coul. NSE	4.184	0.6106	7.668	6.325	1.1943	1.3287
	K88 setup	4.146	0.6112	7.596	6.200	1.1942	1.3217
	K88	4.47	0.60	7.50	6.95	1.17	1.37
3×10^8	Default	3.097	0.6473	8.560	5.635	1.2433	1.3795
	K88 setup + Coul. NSE	3.099	0.6475	8.571	5.649	1.2438	1.3805
	K88 setup	3.071	0.6482	8.451	5.510	1.2442	1.3727
	K88	3.15	0.65	8.37	5.93	1.23	1.40
1×10^9	Default	2.451	0.6831	9.700	5.326	1.2761	1.4905
	K88 setup + Coul. NSE	2.454	0.6828	9.717	5.340	1.2764	1.4917
	K88 setup	2.431	0.6842	9.522	5.171	1.2771	1.4827
	K88	2.48	0.68	9.50	5.28	1.27	1.50

Table 12. The pressure and $q_{01,CJ}$ at the NSE state for the values of ρ_{CJ} and T_{CJ} as given by [Khokhlov \(1988\)](#) for He. For each case, we present the results of [Khokhlov \(1988\)](#) (K88), the results of our calculations with the same input physics of [Khokhlov \(1988\)](#) (K88 setup), and the results of recalculating the pressure with twice the radiation pressure (K88 setup + twice p_{rad}).

ρ_0 [g/cm ³]	Case	P_{CJ}/P_0^{K88}	$q_{01,CJ}$ [10 ¹⁷ erg/g]
1×10^6	K88 setup	25.31	15.09
	K88 setup + twice p_{rad}	36.19	
	K88	36.80	15.10
3×10^6	K88 setup	16.51	14.53
	K88 setup + twice p_{rad}	22.56	
	K88	22.60	14.50
1×10^7	K88 setup	10.02	12.00
	K88 setup + twice p_{rad}	12.81	
	K88	12.80	12.00
3×10^7	K88 setup	6.20	9.05
	K88 setup + twice p_{rad}	7.32	
	K88	7.34	9.09
1×10^8	K88 setup	4.11	6.88
	K88 setup + twice p_{rad}	4.48	
	K88	4.47	6.95
3×10^8	K88 setup	3.02	5.94
	K88 setup + twice p_{rad}	3.14	
	K88	3.15	5.93
1×10^9	K88 setup	2.44	5.30
	K88 setup + twice p_{rad}	2.48	
	K88	2.48	5.28

Rosenbrock method (option RODAS4_SOLVER of MESA) with the parameters $rtol = 10^{-7}$ and $atol = 10^{-8}$. In Section 5.1, we consider the initial composition of CO, and in Section 5.2 we consider the initial composition of He.

5.1 The structure of the detonation wave in CO

In this section, we present the structure of the detonation wave in CO. In Section 5.1.1, we present an example of the structure of a detonation wave for some specific initial conditions. In Sections 5.1.2 and 5.1.3, we calculate the pathological detonation speed, D_* , and the structure of the detonation wave, respectively, as a function of the upstream density. We comment on the uncertainty of the results in Section 5.1.4. Finally, we compare our results to [Khokhlov \(1989\)](#) and to [Townsend et al. \(2016\)](#) in Sections 5.1.5 and 5.1.6, respectively.

5.1.1 An example for CO: $\rho_{0,7} = 1$, $T_{0,9} = 0.2$

We first present in Figure 7, as an example, the structure of a detonation wave as a function of the distance behind the shock, x , for CO, $\rho_{0,7} = 1$, $T_{0,9} = 0.2$ and a detonation speed of $D = 1.157 \times 10^4$ km/s ($> D_* \approx 1.1560 \times 10^4$ km/s for these upstream conditions, see below). Following some induction time, the ^{12}C is consumed and its mass fraction reaches 0.05 at $x \approx 1.9$ cm (red point in the lower panel), where ≈ 0.26 MeV/ m_p are released. This is followed by ^{16}O burning, which synthesises heavier elements, most notably ^{28}Si . It is convenient to mark the end of this process as the state in which the mass fraction of ^{28}Si is maximal ($x \approx 2.1 \times 10^3$ cm, orange point in the lower panel). This burning releases additional ≈ 0.36 MeV/ m_p . As the Carbon and Oxygen continue to burn, the number of heavy nuclei decreases (\bar{A} decreases)

while the average mass number \bar{A} increases. During this stage only a minute amount of ^4He is synthesised, such that $\bar{A} \lesssim \bar{A} \approx 30$, as ^{28}Si is maximal.

At this stage, the material is in a state of NSQE. Following the approach of [Khokhlov \(1989\)](#), we monitor this by calculating $\delta_{56}(x) - \delta_{28}(x)$, where¹⁸

$$\delta_i(x) = \ln(X_i(x)/X_i^*(x)), \quad (18)$$

$X_i^*(x)$ is calculated according to Eq. (9) with $\rho(x)$, $T(x)$, $X_n(x)$, $X_p(x)$; to simplify the notation, we used $i = 28, 56$ for ^{28}Si , ^{56}Ni , respectively. The middle panel shows that $|\delta_{56}(x) - \delta_{28}(x)| = 0.1$ slightly after the point in time when the mass fraction of ^{28}Si is at a maximum, and it decreases as the solution approaches NSE ($|\delta_{56}(x) - \delta_{28}(x)| = 0.01$ at $x \approx 1.7 \times 10^5$ cm, orange point). The middle panel shows that \bar{Y} slowly decreases towards the NSE value, and we verified that the decrease is controlled by the inverse triple- α reaction, $^{12}\text{C} \rightarrow 3^4\text{He}$. During this slow burning, not much energy is released, with the heavy elements approaching $\bar{A} \approx 55$ while a significant amount of ^4He is synthesised, leaving $\bar{A} \approx 25$.

The approach to NSE is monitored with $\delta_{56}(x)$. The middle panel shows that $|\delta_{56}| = 0.1$ at $x \approx 2 \times 10^8$ cm. From that position, $|\delta_{56}|$ decreases exponentially with an e -folding distance of $l_{56} \approx 5.5 \times 10^7$ cm. The brown point marks the location where $|\delta_{56}| = 10^{-3}$. We stop the integration when $\delta_{\max} = 10^{-3}$, where

$$\delta_{\max} = \max_i(|\delta_i|), \quad (19)$$

and we do not go over isotopes with either an $X_i < 10^{-20}$ or an

¹⁸ Note that there is probably a typo in the definition of δ_i in [Khokhlov \(1989\)](#).

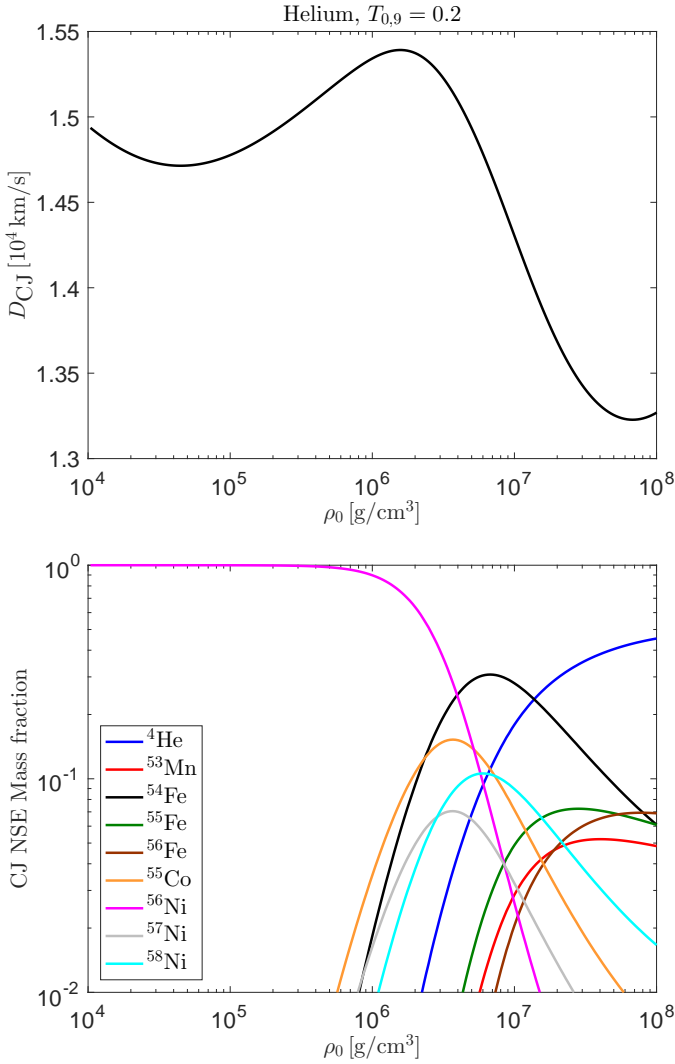


Figure 6. Upper panel: D_{CJ} for He and upstream temperature of $T_{0,9} = 0.2$ as a function of the upstream density. Bottom panel: Mass fractions of key isotopes at the CJ NSE state for the same upstream conditions. We only present the mass fraction of isotopes that have a mass fraction larger than 5×10^{-2} at some ρ_0 within the inspected range.

$X_i^* < 10^{-20}$. It should be realised that the NSE state is only approached asymptotically at infinity, and there is no finite position in which the NSE state is obtained. The deviation of the solution parameters at the end of the integration from the NSE values (points at the right edges of the panels), which are calculated only from the conservation laws, is smaller than 10^{-4} . This demonstrates the high accuracy of our integration.

We mentioned in Section 3.2 that ^{10}C is not included in the isotope list NSE7Si. This isotope approaches its NSE value through the slow reaction $^{10}\text{C}(\alpha, n)^{13}\text{O}$. While this has a negligible effect on the solution, we would have to integrate it over long time periods in order to make sure that $\delta_{\max} = 10^{-3}$. We, therefore, exclude this isotope. This example demonstrates that the distance needed to reach some prescribed deviation from the NSE state is sensitive to the list of isotopes. This is the reason why we monitor the approach to NSE with δ_{56} , which is much less sensitive to the isotope list.

Energy conservation during the integration is monitored by the parameter δ_E , which is the deviation of the conserved quantity

$\varepsilon - q + P/\rho + u^2/2$ (Bernoulli's law) from its initial value¹⁹. The middle panel shows that the value of δ_E increases towards the NSE and is smaller than 10^{-5} at the end of the integration. The loss of accuracy is caused by the detailed balance of fast reactions. The time derivative of the mass fraction of each isotope is a sum over all the reactions that involve that isotope. This sum is actually of the difference of forward and backward reactions, which should be equal at a detailed balance state. Consider such a difference between two fast reactions as the solution approaches a detailed balance. The accuracy in which this difference is calculated decreases since it is the difference between two large numbers with many identical significant digits. For most cases, we are able to maintain a high enough numerical accuracy ($\delta_E < 10^{-3}$) up to the time when $\delta_{\max} = 10^{-3}$. This is enough to fully describe the approach to NSE, since at this stage all the solution parameters are approaching their NSE values exponentially, at an e -folding distance of l_{NSE} . However, for a few cases we were unable to maintain the high accuracy up to the time when $\delta_{\max} = 10^{-3}$. It may be possible to find a specialised algorithm to calculate accurately the approach to NSE, but this is outside the scope of this paper.

At a distance of $x \approx 2.0 \times 10^7$ cm, the heat release becomes endothermic. This is connected with the minimum of the density ($\phi = 0$ in Equations (4)) at $x \approx 2.2 \times 10^7$ cm and with the fact that the detonation speed of this solution is slightly above D_* . For a detonation speed that equals D_* , the position of the point where $\phi = 0$ coincides with the sonic point ($u = c_s$). We numerically determine D_* as the detonation speed for which integration with $D < D_*$ hits the sonic point, $(u^2 - c_s^2)/u^2 < 10^{-3}$, while integration with $D > D_*$ reaches $\delta_{\max} = 10^{-3}$. Therefore, the numerical accuracy of the determined D_* is $\sim 10^{-3}$. The sonic point location was determined as the sonic point of the integration with the highest detonation speed that is still smaller than D_* . However, because of the rapid change of the sonic point location as D approaches D_* (Sharpe 1999), the numerical accuracy of the sonic point location is of the order of a few tens of percent. Other properties of the pathological detonation, which are far from the sonic point, are determined to a numerical accuracy that is similar to the numerical accuracy of D_* determination, i.e. $\sim 10^{-3}$.

5.1.2 The dependance of D_* on the upstream density

The calculated D_* for CO is presented in the upper panel of Figure 4 for an upstream temperature of $T_{0,9} = 0.2$. The deviation between D_{CJ} and D_* is always smaller than $\approx 1.4\%$ (blue line). We are unable to integrate for densities above $\rho_{0,7} = 340$ with a high enough accuracy, i.e., $\delta_E < 10^{-3}$. Furthermore, at these high densities the deviation between D_{CJ} and D_* approaches our numerical accuracy for D_* . Nevertheless, the decrease in the deviation as a function of the upstream density is smaller than exponential, which suggests that even at larger upstream densities the detonation remains pathological. At low densities, the deviation between D_{CJ} and D_* approaches 10^{-3} at $\rho_{0,7} \approx 0.9$. Nevertheless, we present our results even at lower densities, $\rho_{0,7} \gtrsim 0.47$, as long as we were able to integrate with high accuracy. Figure 8 shows that the deviation between D_{CJ} and D_* decreases exponentially with $1/\rho_0$, which suggests that the detonation remains pathological even at lower upstream densities. There could be a change in this behaviour at lower densities (maybe connected with the maximum of D_{CJ} at

¹⁹ We thank Dean Townsley for pointing us to this method.

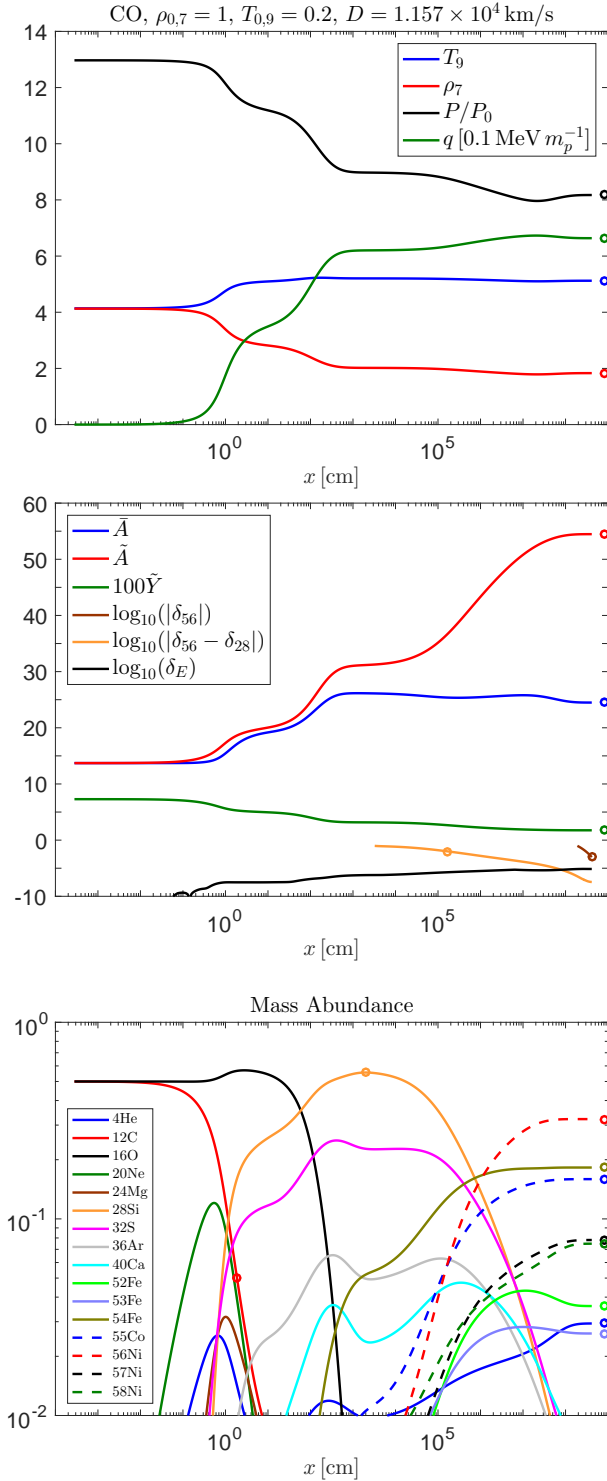


Figure 7. The structure of an overdriven detonation wave as a function of the distance behind the shock. Upper panel: Temperature (blue), density (red), pressure (black) and thermonuclear energy release (green). middle panel: \tilde{A} (blue), \tilde{A} (red), \tilde{Y} (green), δ_{56} (see text, brown), $\delta_{56}(x) - \delta_{28}(x)$ (which monitors the NSQE state, orange) and δ_E (which monitors energy conservation, black). The orange point marks the location where $|\delta_{56} - \delta_{28}| = 10^{-2}$, and the brown point marks the location where $|\delta_{56}| = 10^{-3}$. Bottom panel: Mass fractions of a few key isotopes. The red (orange) point marks the location where the mass fraction of ^{12}C (^{28}Si) reaches 0.05 (is maximal). At a distance of $x \approx 2.0 \times 10^7$ cm, the heat release becomes endothermic. This is connected with the minimum of the density at $x \approx 2.2 \times 10^7$ cm.

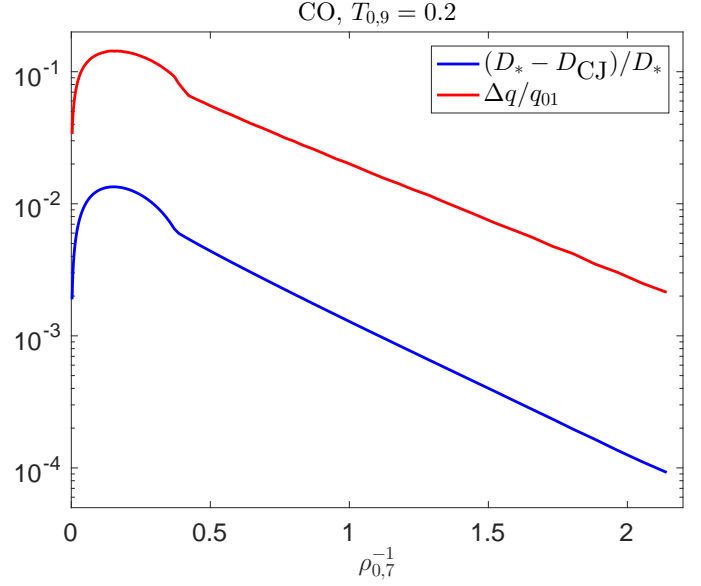


Figure 8. The deviation between D_{CJ} and D_* (blue line) and the difference between the maximal value of q along the integration and q_{01} at the end of the integration, Δq (red line), as a function of $1/\rho_0$. $(D_* - D_{\text{CJ}})/D_*$ decreases exponentially with $1/\rho_0$, which suggests that the detonation remains pathological even at lower upstream densities. $\Delta q/q_{01}$ decreases exponentially with $1/\rho_0$, which shows that higher and higher numerical accuracy is required for lower and lower upstream densities in order to determine whether a detonation is CJ based on $q(x)$ inspection.

$\rho_{0,7} \approx 0.35$), but we are unable to find evidence for CJ detonations at low upstream densities.

The claim that at low upstream densities, $\rho_{0,7} \lesssim 1$, the detonation is CJ was made by [Imshennik & Khokhlov \(1984\)](#) for a pure ^{12}C initial composition and an upstream temperature of $T_{0,9} = 0.2$. Their claim is based on inspecting whether $q(x)$ monotonically increases during CJ detonations. However, it is not clear at which point they stopped the integration, and whether the accuracy of the integration is sufficient for meaningful results close to the NSE state. We find that in order to determine the position at which $q(x)$ begins to decrease, higher and higher numerical accuracy is required for lower and lower upstream densities. This is demonstrated in [Figure 8](#), which shows that the difference between the maximal value of q along the integration and q_{01} at the end of the integration, Δq , normalised by q_{01} , decreases exponentially with $1/\rho_0$. It is, therefore, likely that the numerical accuracy of [Imshennik & Khokhlov \(1984\)](#) did not reach the level needed to identify the point at which $q(x)$ begins to decrease for $\rho_{0,7} \lesssim 1$. [Sharpe \(1999\)](#), who calculated CO with an upstream temperature of $T_{0,9} = 0.1$, claims that at low upstream densities, $\rho_{0,7} < 2$, the detonation is CJ. He determined $D > D_*$ for solutions that reach $\phi = 0$ (and do not hit the sonic point). Although our calculations include a $\phi = 0$ point well below $\rho_{0,7} = 1$, we note that the location of the sonic point changes position in a discontinuous manner from $x \sim 100$ cm to $x \sim 10^4$ cm around $\rho_{0,7} \approx 2.7$ (see detailed discussion below). This rapid change may be the reason for the erroneous claim of [Sharpe \(1999\)](#). In fact, [Dunkley et al. \(2013\)](#) associate this rapid change with the transition from a pathological to a CJ detonation. However, as long as the position of the sonic point is finite, the detonation must be of the pathological type, as the NSE conditions are only obtained in infinity. In this respect, the bottom panel

of figure 1 of Dunkley et al. (2013), which shows the (finite) position of the sonic point for CJ detonations, has no clear meaning. Gamezo et al. (1999) claim that for CO the detonation is CJ at low densities, based on inspecting whether the flow hits a sonic point and is subsonic downstream and upstream of that point. From their demonstration of this method (bottom panel of their figure 3), it is clear that in their integration they actually did not hit the sonic point, as u deviates from c_s by $\approx 1.5\%$. This procedure depends on numerical accuracy as well, and it seems that Gamezo et al. (1999) did not have the required numerical accuracy to detect pathological detonations at low densities (compare their 1.5% accuracy with the red line in Figure 8). This lack of numerical accuracy also makes their figure 7 erroneous.

A few key parameters of these pathological detonations are given in Table 2 for $T_{0,9} = 0.2$. The results are similar to the CJ results, demonstrating that the final CJ NSE conditions provide a good approximation of the pathological NSE conditions.

Similarly to the CJ case, these results do not depend much on the initial upstream temperature. For $T_{0,9} = 0.04$, we are able to integrate within the same range of upstream densities with high enough accuracy. Within this range, the D_* values for $T_{0,9} = 0.04$ deviate from the results for $T_{0,9} = 0.2$ by less than 8×10^{-4} , and the key parameters of Table 2 deviate by less than $\approx 0.6\%$, with the largest deviation obtained for $q_{01,*}$ at $\rho_{0,7} = 300$.

The results calculated with the NSE4 (NSE5) isotope list deviate from the results presented above by less than 7.6×10^{-3} (1.2×10^{-3}), which suggests that our isotope list is converged to at least $\sim 10^{-3}$. For a given D_* , the uncertainty of the results is similar to the CJ case (dominated by the uncertainty of the Coulomb correction terms for the EOS and the Coulomb correction terms for the NSE state), and we estimate it to be on the sub-percent level (see detailed discussion in Section 3.4). However, the values of D_* itself depend also on the reaction rates and are influenced by uncertainties in these rates. The study of this uncertainty is beyond the scope of this paper, but because of the slight deviation ($\lesssim 1.4\%$) of D_* from D_{CJ} (that does not depend on the reaction rates), we speculate that this uncertainty is smaller than a few percent.

5.1.3 The dependance of the burning scales on the upstream density for CO

In Figure 9, different scales of the CO pathological detonation are compared with a typical dynamical scale of $v/\sqrt{G\rho_0}$ with $v = 10^4$ km/s. All scales, except for the sonic point location, are determined from the profiles with the lowest detonation speed that is still larger than D_* (slightly overdriven). For low densities, $\rho_{0,7} \lesssim 0.47$, where we are unable to determine D_* we estimate the scales by integrating with $D = D_{CJ}$. Since at these densities D_* (if exists) probably deviates from D_{CJ} by less than 10^{-4} and we are able to integrate with high accuracy up to the presented scales, our results should be an excellent estimate. The location where $|\delta_{56}| = 10^{-3}$ and l_{56} are shown as well, which allows to estimate the position of a smaller deviation from NSE. Note that many works present a finite position for NSE that does not have a clear meaning (Khokhlov 1989; Townsley et al. 2016; Dunkley et al. 2013), since the NSE is only obtained asymptotically at infinity. The numerical accuracy of all the scales in Figure 9 is $\lesssim 10^{-3}$, except for the sonic point location with a numerical accuracy of the order of a few tens of percent (see discussion above), which is also the reason for the noisy appearance of this curve.

The ordering of the different scales as a function of the up-

stream density is similar to the case $\rho_{0,7} = 1$, described in detail in Section 5.1.1. Following some induction time, the ^{12}C is consumed and ≈ 0.3 MeV/ m_p are released. This is followed by ^{16}O burning that synthesises heavier elements, $\tilde{A} \approx 30$, roughly when the mass fraction of ^{28}Si is maximal. Slightly later, the material is in NSQE ($|\delta_{56}(x) - \delta_{28}(x)| = 0.01$), and it approaches NSE while heavier elements are synthesised with $\tilde{A} \gtrsim 50$ without releasing much energy.

In order to determine which reactions control the approach to NSE (where \tilde{Y} approaches its NSE value), we inspect at $|\delta_{56}| = 10^{-3}$ all the reactions that can change the value of \tilde{Y} . Of those reactions, the ones that are not in a detailed balance with their reverse reactions dominate the net change in \tilde{Y} , so we sort the reactions according to the absolute value of the difference between them and their reverse reactions. The reactions with the largest differences, which control the approach to NSE, are shown in Figure 10. The approach to NSE is controlled at low upstream densities, $\rho_{0,7} \lesssim 10$, by the inverse triple- α reaction, $^{12}\text{C} \rightarrow 3^4\text{He}$, and to some extent by $^2\text{H} \rightarrow n + p$, while at high densities $^2\text{H} \rightarrow n + p$ is the dominant process with an additional contribution from $^{11}\text{B} + p \rightarrow 3^4\text{He}$. At very high densities, $\rho_{0,7} \gtrsim 200$, $^{11}\text{B} + p \rightarrow 3^4\text{He}$ and $p + ^2\text{H} \rightarrow n + 2p$ are dominant and comparable. Except for the inverse triple- α reaction that was known to determine the length scale of the detonation wave at low densities, the importance of the other reactions was not identified in the past.

The scales themselves shorten significantly as the upstream density increases, due to the increase in the post-shock temperature. Furthermore, the temperature at the NSE state increases monotonically with ρ_0 , which decreases both \tilde{A} and q_{01} at these states (see Table 2). At large upstream densities, the released energy is not much larger than the contribution from Carbon burning. Usually the detonated material will later cool and ^4He will recombine to release more energy without a large change in \tilde{A} . The upstream densities in which some values of q_{01} are obtained at the NSE state are marked with dashed lines at the bottom panel of Figure 9. Note that for CJ detonations the scale at which these q_{01} values are obtained should diverge as the upstream density decreases. However, since for pathological detonations the energy release is not monotonic, these q_{01} values are obtained after a finite distance behind the shock wave. Figure 9 allows to estimate for a given upstream density and physical scale the amount of guaranteed energy release and the obtained value of \tilde{A} (for example, whether iron group elements can be synthesized).

The sonic point location is always above the locations where the mass fraction of ^{28}Si is maximal and where $\tilde{A} = 30$. This observation differs from the claims of Gamezo et al. (1999).

A discontinuous behaviour of the sonic point location, from $x \sim 100$ cm to $x \sim 10^4$ cm around $\rho_{0,7} \approx 2.7$, is seen in the bottom panel of Figure 9 (it was observed but misinterpreted by Dunkley et al. (2013), and there is a hint for this transition in figure 1 of Townsley et al. (2016)). This is also seen as a minimum of D_* at this upstream density in the upper panel of Figure 4. The reason for this behaviour is explained in Figure 11, which shows the slightly overdriven density profiles for $T_{0,9} = 0.2$ and an upstream density in the range of $[2.5, 2.9] \times 10^7$ g/cm 3 . For the low upstream densities there are 3 locations where $\phi = 0$ (x_1 , x_2 , and x_3). Each of those points is an extremum point of the density (there is another such point at infinity). The sonic point location for these upstream densities is near $x_3 \sim 10^4$ cm. As the upstream density increases, there remains only a single location where $\phi = 0$, which is close to $x_1 \sim 10^2$ cm. Around this transition, the sonic point changes loca-

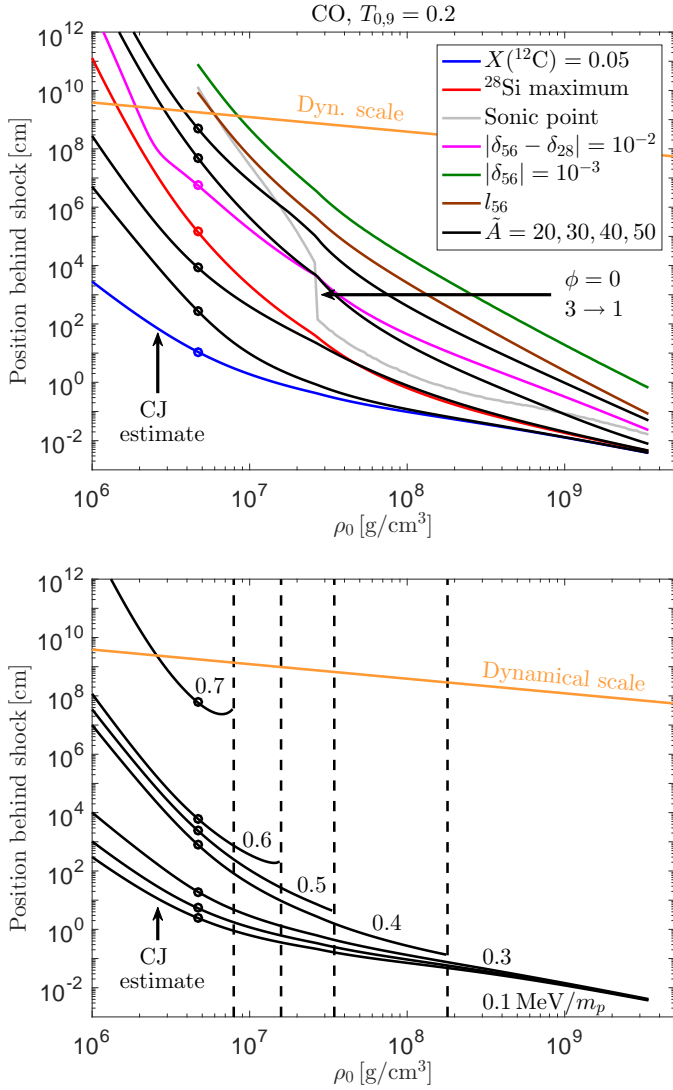


Figure 9. Different scales of the CO pathological detonation in comparison with a typical dynamical scale of $v/\sqrt{G\rho_0}$ with $v = 10^4$ km/s (orange). Top panel: The ^{12}C consumption scale (blue), ^{28}Si maximum (red), the location where $\tilde{A} = 20, 30, 40,$ and 50 (bottom to top, black), the location where $|\delta_{56} - \delta_{28}| = 10^{-2}$ (magenta), and the location where $|\delta_{56}| = 10^{-3}$ (green) and l_{56} (brown). Bottom panel: The locations where the energy release is $0.1, 0.2, \dots, 0.7$ MeV/ m_p (bottom to top, black). These scales are determined from the profiles with the lowest detonation speed that is still larger than D_* (slightly overdriven). The sonic point location (gray, top panel) is determined from the profiles with the highest detonation speed that is still lower than D_* . For low densities, $\rho_{0,7} \lesssim 0.47$, where we are unable to determine D_* we estimate the position of the scales (except the location of the sonic point, $|\delta_{56}| = 10^{-3}$ and l_{56}) by integrating with $D = D_{CJ}$. Dashed lines in the bottom panel mark the upstream densities in which some values of q_{01} are obtained at the NSE state. A discontinuous behaviour of the sonic point location, from $x \sim 100$ cm to $x \sim 10^4$ cm, is obtained around $\rho_{0,7} \approx 2.7$.

tion to x_1 . We mark this transition as $\phi = 0, 3 \rightarrow 1$ in the upper panels of Figures 4 and 9. The slight jittering of the sonic point location as the density changes is a consequence of the rapid shift in the sonic point location as D approaches D_* .

Our analysis indicates some minor dependance of the scales on the upstream temperature (see dotted lines in Figure 12). The

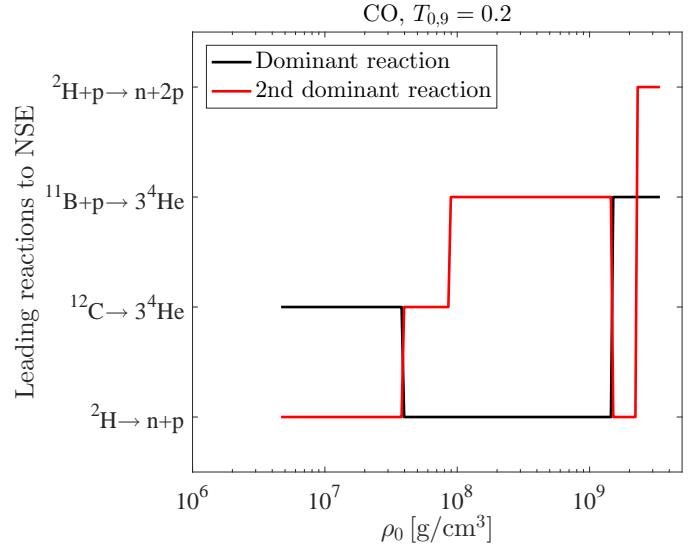


Figure 10. The reactions that dominate the net change of \tilde{Y} at $|\delta_{56}| = 10^{-3}$, as a function of the upstream density for CO.

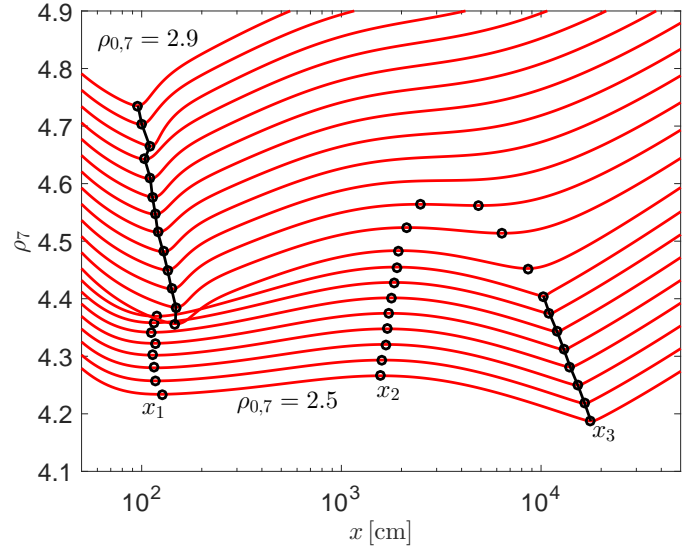


Figure 11. The slightly overdriven density profiles for CO, $T_{0,9} = 0.2$ and an upstream density in the range of $[2.5, 2.9] \times 10^7$ g/cm 3 . For the low upstream densities, there are 3 locations where $\phi = 0$ (x_1 , x_2 , and x_3 , black points). Each of these points is an extremum point of the density. The sonic point location (black line) for these upstream densities is near $x_3 \sim 10^4$ cm. As the upstream density increases, there remains only a single location where $\phi = 0$, which is close to $x_1 \sim 10^2$ cm. Around this transition, the sonic point changes location to x_1 .

largest one is for the Carbon burning scale at high densities. The Carbon burning scale is shown as a function of the upstream density in Figure 13 for $\rho_{0,7} = 300$. The burning scale decreases as the upstream temperature increases. This is because the post-shock temperature, T_s , depends slightly on the upstream temperature. This effect is obtained at high densities, where the post-shock plasma is slightly degenerate, making the temperature a sensitive function of the pressure. We note that the ion coupling parameter, Γ , of the upstream plasma is larger than 200 for $T_{0,9} \lesssim 0.032$, where the fit

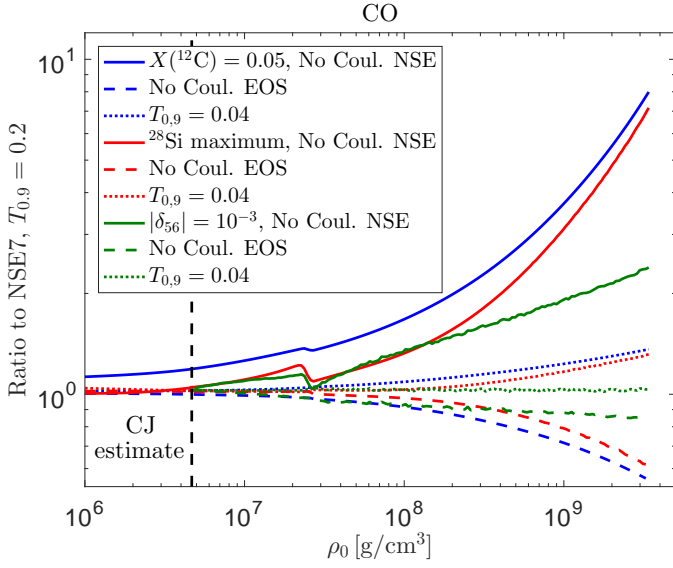


Figure 12. The ratio between the Carbon burning scale (blue), the positions where ^{28}Si is maximal (red) and where $|\delta_{56}| = 10^{-3}$ (green) obtained under various assumptions and these scales obtained with our default input physics and $T_{0,9} = 0.2$. The solid lines are without the addition of the Coulomb correction term of the EOS, dashed lines are without the addition of the Coulomb correction term to the NSE state and the dotted lines are for $T_{0,9} = 0.04$.

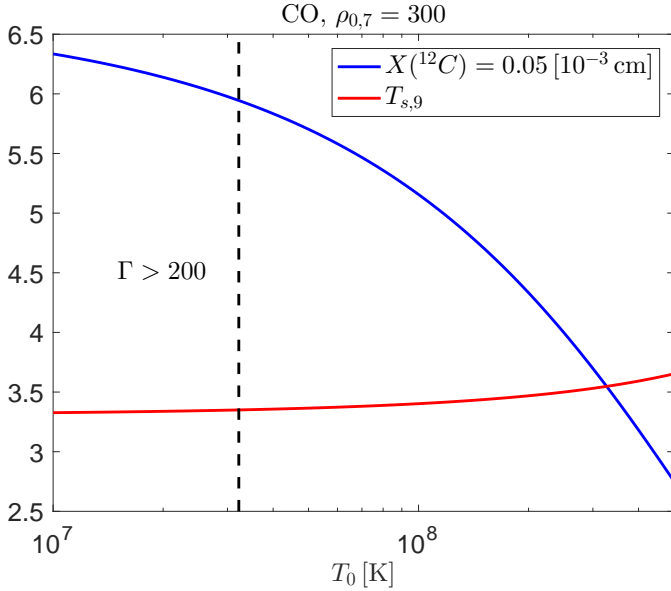


Figure 13. The Carbon burning scale (blue) and the post-shock temperature (red) as a function of the upstream density for CO and $\rho_{0,7} = 300$. The ion coupling parameter, Γ , of the upstream plasma is larger than 200 for $T_{0,9} \lesssim 0.032$, where the fit for $f(\Gamma)$ is not valid.

for $f(\Gamma)$ is not valid. This is the reason that we choose $T_{0,9} = 0.04$ for the temperature sensitivity tests in the previous CO sections.

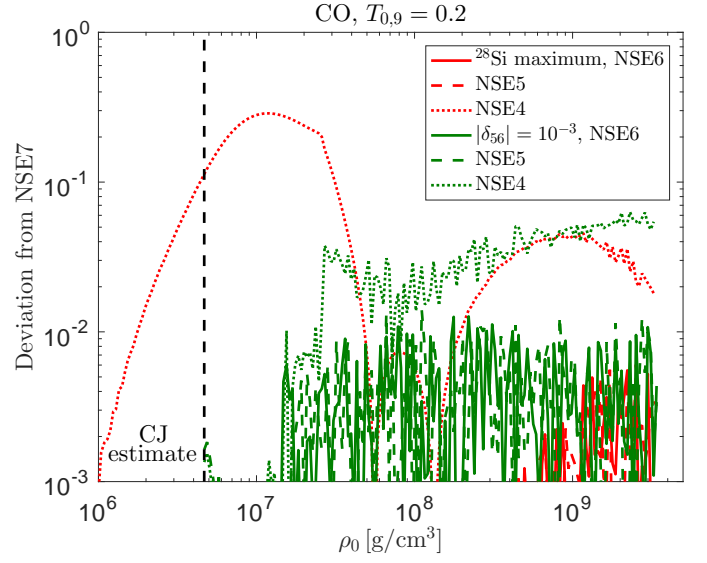


Figure 14. The deviations of the positions where ^{28}Si is maximal (red) and where $|\delta_{56}| = 10^{-3}$ (green), calculated with the NSE4 (dotted lines), NSE5 (dashed lines) and NSE6 (solid lines) isotope lists, from the results calculated with the NSE7 isotope list, for CO at $T_{0,9} = 0.2$ as a function of the upstream density.

5.1.4 The uncertainty of the CO results

The deviations of the positions where ^{28}Si is maximal and where $|\delta_{56}| = 10^{-3}$, calculated with the NSE4, NSE5 and NSE6 isotope lists, from the results calculated with the NSE7 isotope list are presented in Figure 14. Deviations as high as $\approx 30\%$ are obtained for NSE4, while the deviations of NSE5 and NSE6 are smaller than the percent level. The other scales shown in Figure 9 have smaller deviations. We verified that the deviations of the results obtained with the NSE7Si list deviate by less than a percent from the results obtained with the NSE7 list. This suggests that our calculation of the length scales is converged to the percent level. The effect of the Coulomb correction is examined in Figure 12. The Coulomb corrections to the EOS are only important at high densities, and they change at most the Carbon burning scale by a factor of ~ 2 . The Coulomb correction terms to the NSE have a significant effect at high densities, where they can decrease the length scales by up to one order of magnitude, as they increase the reaction rates. Uncertainty in the reaction rates can be at the same level or even higher, making the length scales uncertain to a factor of a few. However, a detailed study of the sensitivity to uncertainty in the reaction rates is beyond the scope of this paper.

5.1.5 Comparing the detonation wave structure in CO to Khokhlov (1989)

Khokhlov (1989) calculated the detonation wave structure for CO, an upstream temperature of $T_{0,9} = 0.2$ and a few values of the upstream density in the range of $[10^7, 3 \times 10^9] \text{ g/cm}^3$. The EOS used by Khokhlov (1989) is the same as the EOS used by Khokhlov (1988)²⁰. Since Khokhlov (1989) does not mention that the EOS

²⁰ Although the nuclear level excitations are missing from the description of the EOS in Khokhlov (1989).

used by [Khokhlov \(1988\)](#) is erroneous, as we showed in Section 4.1.2, and is citing erroneous D_{CJ} values from [Khokhlov \(1988\)](#), we assume that the EOS used by [Khokhlov \(1989\)](#) is erroneous as well. The list of isotopes included 114 isotopes, and used the modern values of the binding energies and partition functions.

We concentrate on the $\rho_{0,7} = 30$, for which [Khokhlov \(1999\)](#) provides detailed results. [Khokhlov \(1989\)](#) reports that $D_* = 1.218 \times 10^4$ km/s, while we find that $D_* = 1.2107 \times 10^4$ km/s for same input physics (similar deviation was found in Section 4.1.2 D_{CJ}). It is apparent from our comparison of the structure of an α driven detonation with $D = 1.233 \times 10^4$ km/s (Figure 15, note different units of the x -axes of the two panels) that the NSE is different between the two calculations (especially in the up panel). This difference is similar in magnitude to the one we found in Section 4.1.2 for the CJ state, suggesting that it is connected to the erroneous EOS used by [Khokhlov \(1989\)](#). This could also be the reason for the higher (lower) temperatures (pressures) that we get around 1 mm. For the δ_{NSQE} , it seems that [Khokhlov \(1989\)](#) plotted $\delta_{28} - \delta_{56}$ (and not $\delta_{56} - \delta_{28}$, as claimed by [Khokhlov \(1989\)](#) so we plot this as well. Note that the scale of δ_{NSE} and δ_{NSQE} is linear. The abundance of the isotopes, shown in the bottom panel of Figure 15, is similar in the two calculations, except for the much faster consumption of ^{16}O around 1 mm in our calculation, which is because of the higher temperatures we get there.

We next compare in Figure 16 our results with the input physics of [Khokhlov \(1989\)](#) (solid lines) to the results with the default input physics (dotted lines). The Carbon and Silicon burning length scales are smaller by a factor of ~ 2 in the default case, $|\delta(56)| = 10^{-3}$ at a distance that is smaller by a factor of ~ 2 . The inclusion of the Coulomb correction term for the NSE (dashed lines) decreases the Carbon burning length scale to the default value (see also Figure 12). The remaining discrepancies are because of the isotope list used by [Khokhlov \(1989\)](#). We verified that the default results are reproduced by adding the missing isotopes from NSE7 with $Z \leq 14$ and from the α -ext lists to the list used by [Khokhlov \(1989\)](#), which increases the number of isotopes to 137. In fact, the results from NSE4 deviate by less than 10% for upstream density (see Figure 14), which shows that with 137 isotopes (although somewhat different from the 114 used by [Khokhlov \(1989\)](#)) much better results could have been obtained.

5.1.6 Comparison to [Townsend et al. \(2016\)](#)

[Townsend et al. \(2016\)](#) calculated the detonation wave structure for an initial composition of $X(^{12}\text{C}) = 0.5$, $X(^{16}\text{O}) = 0.48$, $X(^{22}\text{Ne}) = 0.02$ (CONE), an upstream temperature of $T_{0,9} = 0.4$ and a few values of the upstream density in the range of $[5 \times 10^6, 2 \times 10^8]$ g/cm³. The calculation was performed with TORCH ([Timmes 1999](#)), which uses the *Helmholtz* EOS. The list of isotopes included 200 isotopes²¹, and screening was applied for the reaction rates. We concentrate on the overdriven detonation in which $\rho_{0,7} = 1$ and $D = 1.166 \times 10^4$ km/s, for which [Townsend et al. \(2016\)](#) provide detailed results. We calculate the detonation wave structure for this case by using the (corrected, see Appendix B) *Helmholtz* EOS, the TORCH200 isotope list (without ^8Be and ^9B , see Section 3.2, which sums up to 203 isotopes), and using the option of the EXTENDED SCREENING of MESA. As the other input physics, we use our usual

²¹ [Townsend et al. \(2016\)](#) probably used the TORCH200 net, which actually contains 205 isotopes.

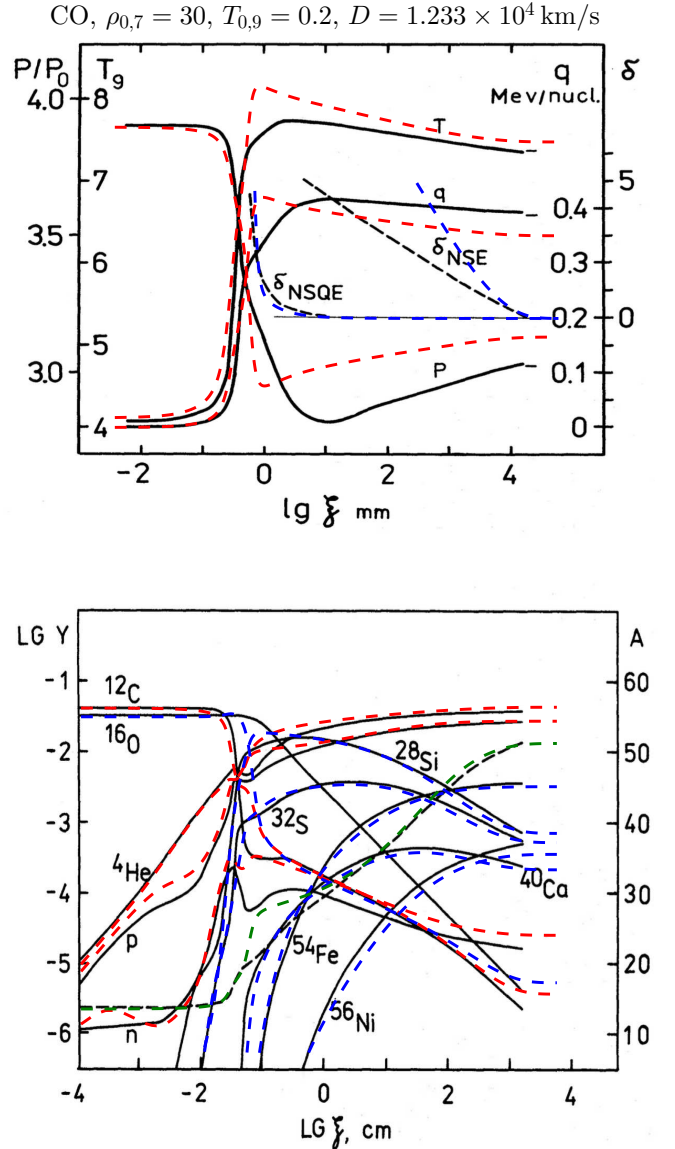


Figure 15. Figures 7 and 8 from [Khokhlov \(1989\)](#). The structure of an overdriven detonation wave for CO, $T_{0,9} = 0.2$, $\rho_{0,7} = 30$ and $D = 1.233 \times 10^4$ km/s, as a function of the distance behind the shock. Black lines are the results of [Khokhlov \(1989\)](#), while the coloured lines are our results with the input physics of [Khokhlov \(1989\)](#). Here, $\delta_{NSQE} = \delta_{56} - \delta_{28}$ (but we actually plot $\delta_{28} - \delta_{56}$, since it seems that [Khokhlov \(1989\)](#) plotted this as well) and $\delta_{NSE} = \delta_{56}$. The green dashed line in the bottom panel is \bar{A} (note that the right y-axis label, A , is probably a typo, and should be $\langle A \rangle$ with the definitions of [Khokhlov \(1989\)](#)). Note that the x -axes units in the two panels are different.

default values. Since neither the EXTENDED SCREENING nor the screening used by TORCH respect a detailed balance, the integration does not terminate at NSE, but rather at some other steady-state configuration. We integrate up to $t = 10$ s, at which point this steady state was obtained.

The deviation of our results (Figure 17, dashed lines) from those of [Townsend et al. \(2016\)](#) (solid lines) is quite small²². For

²² We thank Dean Townsend for sharing their results with us.

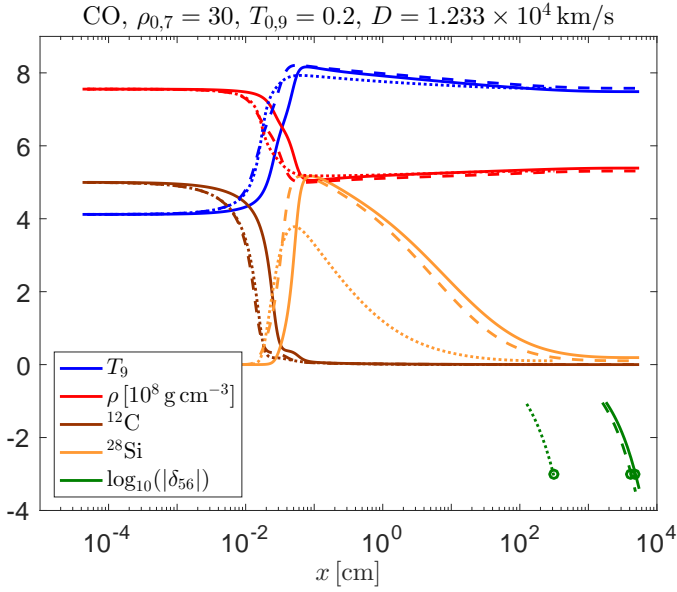


Figure 16. The structure of an overdriven detonation wave for CO, $T_{0,9} = 0.2$, $\rho_{0,7} = 30$ and $D = 1.233 \times 10^4$ km/s, as a function of the distance behind the shock. We show the temperature (blue), density (red), ^{12}C mass fraction (brown), ^{28}Si mass fraction (orange), and δ_{56} (green). The solid lines present the results with the input physics of Khokhlov (1989), the dashed lines are with the addition of the Coulomb correction terms to the NSE, and the dotted lines are the results with the default input physics. The green points mark the locations where $|\delta_{56}| = 10^{-3}$.

example, the deviation in the pressures is smaller than 2%. This difference is probably because of the somewhat different reaction rates and screening factors incorporated into each of the two calculations. A calculation with our default input physics is presented as well in Figure 17 (dotted lines). As usual, the integration is performed up to $\delta_{\max} = 10^{-3}$. Larger deviations are obtained between the default calculation and the results of Townsley et al. (2016). For example, a deviation of $\approx 7\%$ is obtained in the pressure at a distance of $x \sim 10^7$ cm. It is evident that the NSE values obtained with our default input physics deviate by a few percent from the steady-state configuration obtained by Townsley et al. (2016). The easiest way to analyse these differences is to compare their NSE states (which are independent of reaction rates), but since Townsley et al. (2016) used non physical screening factors, such a state does not exist for their input physics.

With respect to figure 1 of Townsley et al. (2016), since there the pathological detonation speed was not calibrated to high accuracy and the sonic point location was determined by the location of the density minimum²³, the position of the ^{28}Si abundance maximum and the sonic point location are not adequate for an accurate comparison. The position of the NSE state, reported there, has no clear physical meaning, since the NSE state is only approached asymptotically at infinity, and because of the screening factors used by Townsley et al. (2016), the simulations actually converge to a different state.

²³ Dean Townsley, private communication.

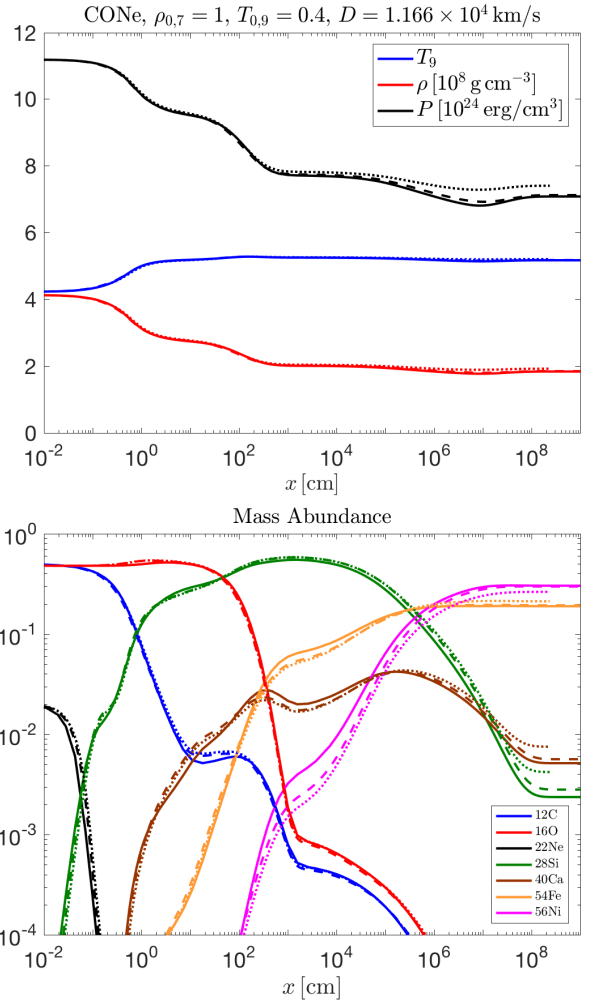


Figure 17. The structure of an overdriven detonation wave for $X(^{12}\text{C}) = 0.5$, $X(^{16}\text{O}) = 0.48$, $X(^{22}\text{Ne}) = 0.02$, $T_{0,9} = 0.4$, $\rho_{0,7} = 1$ and $D = 1.166 \times 10^4$ km/s, as a function of the distance behind the shock. Solid lines are the results from Townsley et al. (2016), dashed lines are our results with the input physics of Townsley et al. (2016) and the EXTENDED SCREENING option of MESA, and dotted lines are the results with our default input physics. Upper panel: Temperature (blue), density (red) and pressure (black). Bottom panel: The mass fraction of key isotopes. Note that since the EXTENDED SCREENING option does not respect a detailed balance, the integration does not terminate at NSE, so we integrate up to $t = 10$ s.

5.2 The structure of the detonation wave in He

In this section, we present the structure of the detonation wave in He. In Section 5.2.1, we present an example of the structure of a detonation wave for some specific initial conditions. In Section 5.2.2, we calculate the structure of the detonation wave as a function of the upstream density. We then comment on the uncertainty of the results in Section 5.2.3. Finally, we compare our results to Khokhlov (1989) in Section 5.2.4.

5.2.1 An example for He: $\rho_{0,7} = 1$, $T_{0,9} = 0.2$

We present in Figure 18, as an example, the structure of a detonation wave for He, $\rho_{0,7} = 1$, $T_{0,9} = 0.2$ and a detonation speed of $D = 1.432 \times 10^4$ km/s ($> D_{\text{CJ}} \approx 1.4304 \times 10^4$ km/s for these

upstream conditions, see Table 8). The structure of this detonation wave is very different from the structure of a detonation wave in CO. The burning of ${}^4\text{He}$ immediately synthesises heavy elements with $\bar{A} \approx 55$ (see detailed discussion in Khokhlov (1984) and a somewhat more accurate description in Khokhlov & Ergma (1985)). This mode of burning depletes the ${}^4\text{He}$ by 10(50)% at $x \approx 1.4 \times 10^3 (4.0 \times 10^4)$ cm (blue points in the lower panel), while increasing \tilde{Y} and \bar{A} , almost without changing \bar{A} , and releasing ≈ 1.1 MeV/ m_p . Most of the energy is being release with the plasma not in NSQE, as $|\delta_{56}(x) - \delta_{28}(x)| = 0.01$ at $x \approx 7.8 \times 10^4$ cm (orange point in the middle panel), where already ≈ 0.77 MeV/ m_p have been released.

The middle panel shows that \tilde{Y} increases towards the NSE value (compare with Figure 7, in which \tilde{Y} decreases towards the NSE value), and we verified that the increase is controlled by the triple- α reaction, $3{}^4\text{He} \rightarrow {}^{12}\text{C}$. The middle panel shows that $|\delta_{56}| = 0.1$ at $x \approx 2.4 \times 10^6$ cm. From that position, $|\delta_{56}|$ decreases exponentially with an e -folding distance of $l_{56} \approx 2.6 \times 10^6$ cm. The brown point marks the location where $|\delta_{56}| = 10^{-3}$. As usual, we stop the integration when $\delta_{\max} = 10^{-3}$. The deviation of the solution parameters at the end of the integration from the NSE values (points at the right edges of the panels), which are calculated only from conservation laws, is smaller than 10^{-3} . The middle panel shows that the value of δ_E increases towards NSE and is $\approx 10^{-5}$ at the end of the integration. This demonstrates the high accuracy of our integration.

5.2.2 The dependance of the burning scales on the upstream density for He

For He, the detonation is of the CJ type (see detailed discussion in Section 6). Different scales of the He CJ detonation are shown in Figure 19. For low densities, $\rho_{0,7} \lesssim 0.30$, we are unable to integrate with high accuracy up to the location where $|\delta_{56}| = 10^{-3}$, so this location and l_{56} are not shown for these densities. The numerical accuracy of all scales in Figure 19 is $\lesssim 10^{-3}$.

For high upstream densities, $\rho_{0,7} \gtrsim 0.015$, the ordering of the different scales as a function of the upstream density is similar to the case of $\rho_{0,7} = 1$ that was described in detail in Section 5.2.1. The burning of ${}^4\text{He}$ synthesises heavy elements with $\bar{A} \approx 55$ much faster than the rate in which ${}^4\text{He}$ is depleted. At lower upstream densities, the depletion rate of ${}^4\text{He}$ is faster than the rate at which heavy elements are synthesised. The energy release roughly follows the ${}^4\text{He}$ depletion, and most of the energy is being release with the plasma not in NSQE. The reactions that dominate the approach to NSE are shown in Figure 19. The approach to NSE is controlled at low upstream densities, $0.3 \lesssim \rho_{0,7} \lesssim 10$, by the triple- α reaction, $3{}^4\text{He} \rightarrow {}^{12}\text{C}$, and to some extent by $n + p \rightarrow {}^2\text{H}$, while at high densities $n + p \rightarrow {}^2\text{H}$ is the dominant process with an additional contribution from $3{}^4\text{He} \rightarrow {}^{11}\text{B} + p$.

The scales themselves shorten significantly as the upstream density increases, due to the rise in the the post-shock temperature. Furthermore, the temperature at the CJ NSE state increases monotonically with ρ_0 , which decreases both \bar{A} and q_{01} at these states (see Table 8). We mark with dashed lines in the bottom panel of Figure 19 the upstream densities in which some values of q_{01} are obtained at the CJ NSE state.

Some minor dependance of the scales on the upstream temperature are obtained (see dotted lines in Figure 21, the electron-electron term is neglected here, and it is a few percent correction for $\rho_{0,7} \lesssim 0.027$, $T_{0,9} = 0.01$). The largest one is for the scale

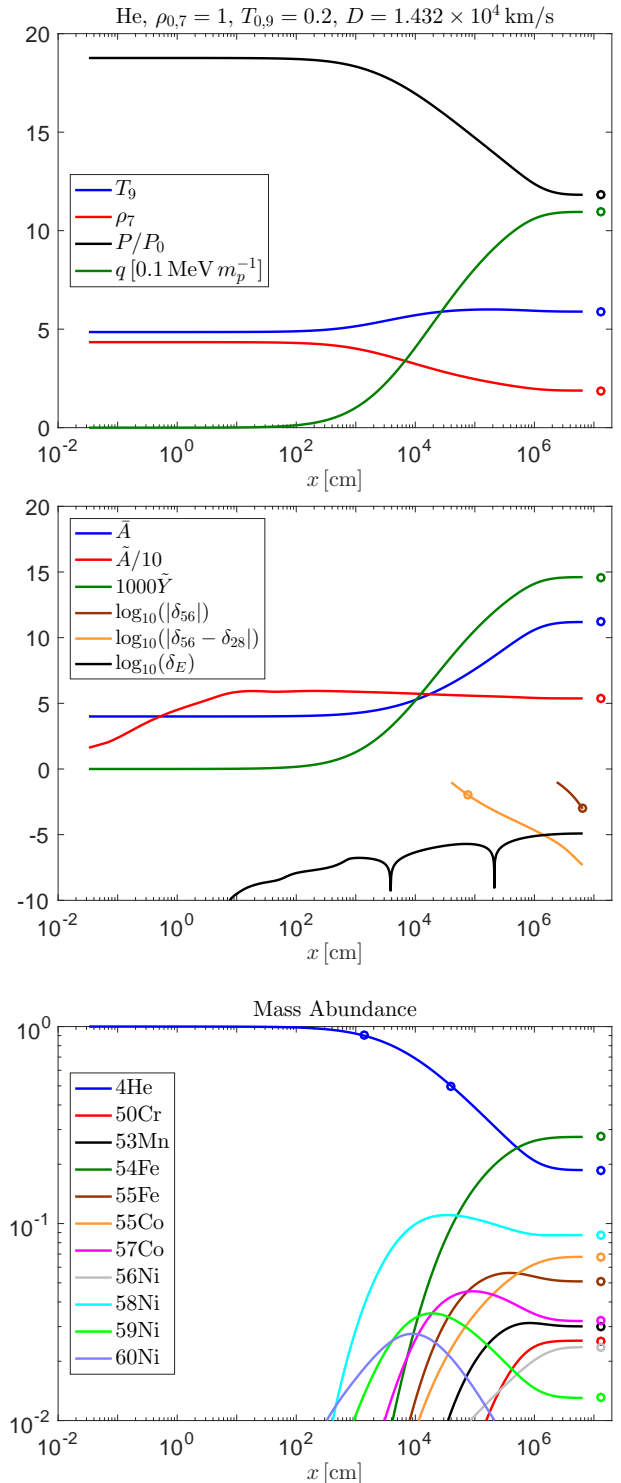


Figure 18. The structure of an overdriven detonation wave as a function of the distance behind the shock. Upper panel: Temperature (blue), density (red), pressure (black) and thermonuclear energy release (green). Middle panel: \bar{A} (blue), $\bar{A}/10$ (red), \tilde{Y} (green), δ_{56} (see text, brown), $\delta_{56}(x) - \delta_{28}(x)$ (which monitors the NSQE state, orange) and δ_E (which monitors energy conservation, black). The orange point marks the location where $|\delta_{56} - \delta_{28}| = 10^{-2}$, and the brown point marks the location where $|\delta_{56}| = 10^{-3}$. Bottom panel: Mass fractions of a few key isotopes. The blue points mark the locations where the mass fraction of ${}^4\text{He}$ reaches 0.9, 0.5.

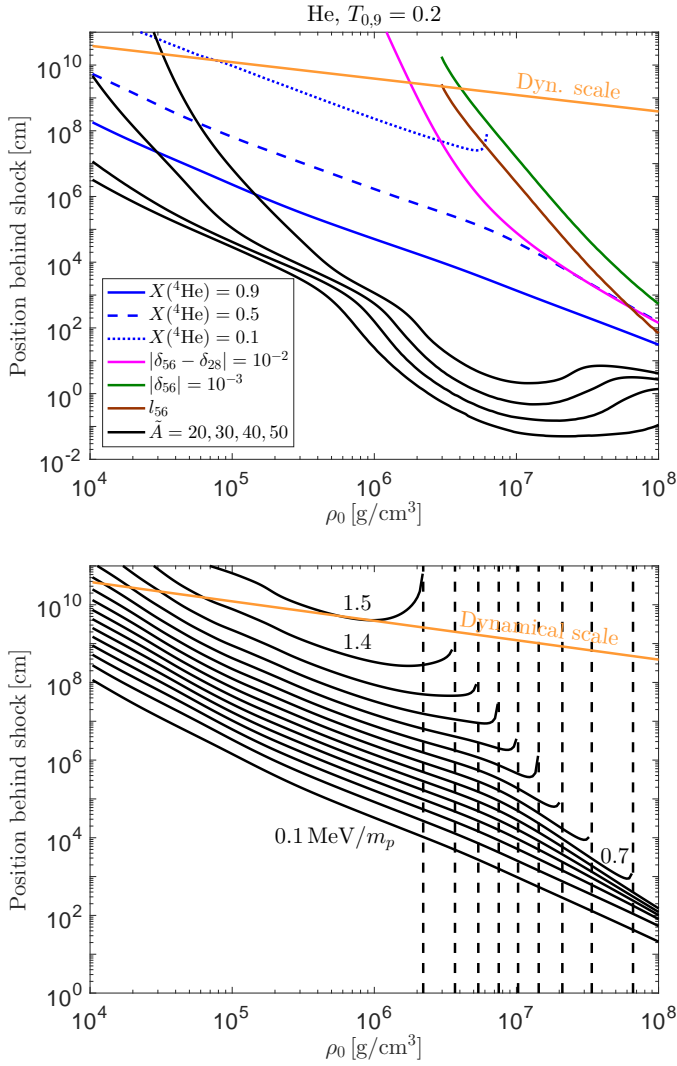


Figure 19. Different scales of the He CJ detonation in comparison with a typical dynamical scale of $v/\sqrt{G\rho_0}$ with $v = 10^4$ km/s (orange). Top panel: The ${}^4\text{He}$ consumption scale (blue, $X({}^4\text{He}) = 0.9, 0.5, 0.1$ solid, dashed, dotted, respectively), the location where $\tilde{A} = 20, 30, 40, 50$ (bottom to top, black), the location where $|\delta_{56} - \delta_{28}| = 10^{-2}$ (magenta) the location where $|\delta_{56}| = 10^{-3}$ (green) and l_{56} (brown). Bottom panel: The locations where the energy release is 0.1, 0.2, ..., 1.5 MeV/ m_p (bottom to top, black). Dashed lines in the bottom panel mark the upstream densities in which some values of $q_{01,\text{CJ}}$ are obtained at the NSE state.

at which $\tilde{A} = 20$ at high densities. This scale is shown as a function of the upstream density in Figure 22 for $\rho_{0,7} = 10$. The scale decreases as the upstream temperature increases, because the post-shock temperature, T_s , depends slightly on the upstream temperature. This effect is obtained at high densities, where the post-shock plasma is slightly degenerate, making the temperature a sensitive function of the pressure.

5.2.3 The uncertainty of the He results

The deviations of the positions where $\tilde{A} = 20$, where half of the ${}^4\text{He}$ is consumed and where $|\delta_{56}| = 10^{-3}$, calculated with the NSE4, NSE5 and NSE6 isotope lists, from the results calculated with the NSE7 isotope list are presented in Figure 23. Deviations as

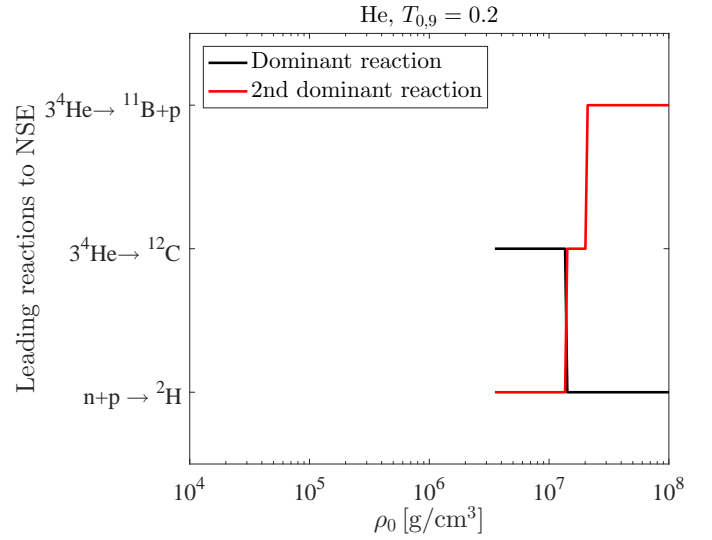


Figure 20. The reactions that dominate the net change of \tilde{Y} at $|\delta_{56}| = 10^{-3}$, as a function of the upstream density for He.

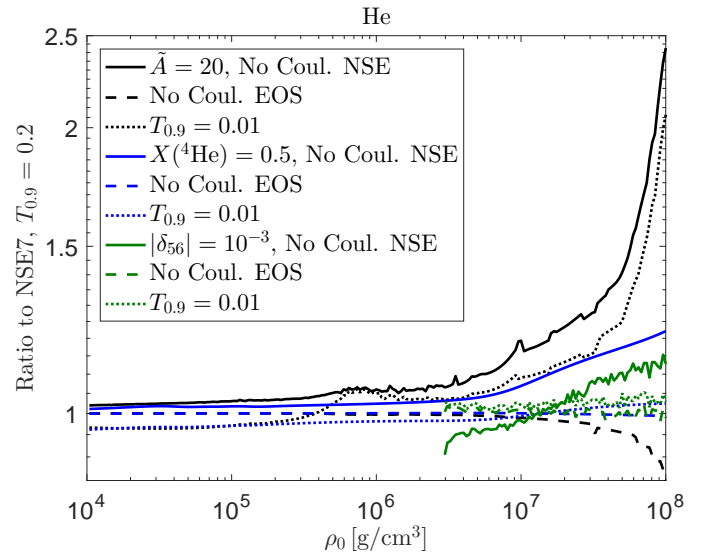


Figure 21. The ratio between the positions at which $\tilde{A} = 20$ (black), where half of the ${}^4\text{He}$ is consumed (blue) and where $|\delta_{56}| = 10^{-3}$ (green) is obtained under various assumptions and the scales that are obtained with our default input physics and $T_{0,9} = 0.2$. The solid lines are without the Coulomb correction term of the EOS, dashed lines are without the Coulomb correction term to the NSE state and dotted lines are for $T_{0,9} = 0.01$. The electron-electron term is neglected here, and it is a few percent correction for $\rho_{0,7} \lesssim 0.027$, $T_{0,9} = 0.01$.

high as an order unity are obtained for NSE4, while the deviations of NSE5 and NSE6 are smaller than a few percent (not including $|\delta_{56}| = 10^{-3}$ near $\rho_{0,7} \lesssim 0.30$, where we are unable to integrate with high accuracy up to this location). The other scales shown in Figure 19 have smaller deviations. We verified that the deviations of the results obtained with the NSE7Si list deviate by less than a few percent from the results obtained with the NSE7 list. This suggests that our calculation of the length scales is converged to a few percent. The effect of the Coulomb correction is examined in

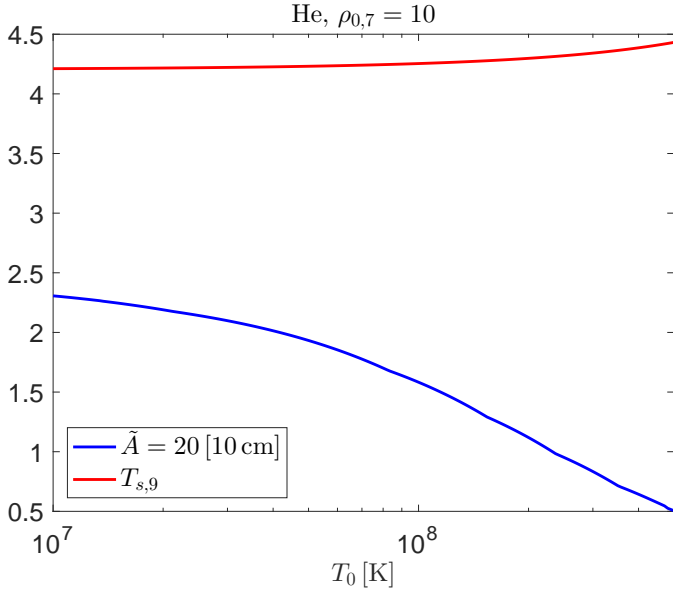


Figure 22. The scale at which $\tilde{A} = 20$ (blue) and the post-shock temperature (red) as a function of the upstream density for He and $\rho_{0,7} = 10$.

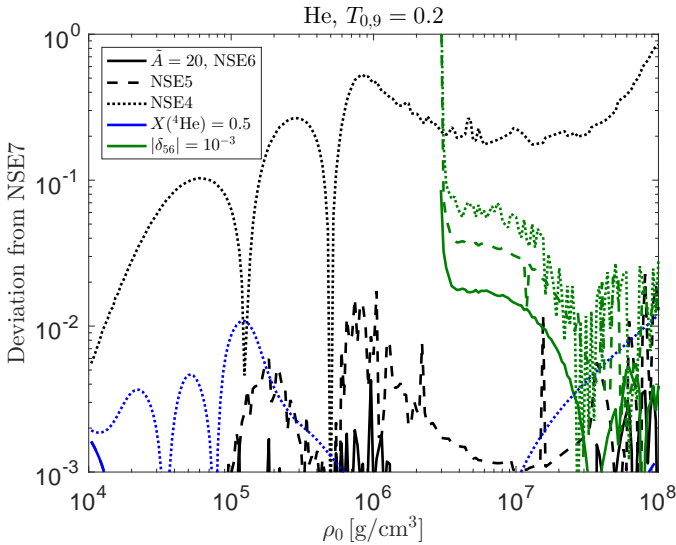


Figure 23. The deviations of the positions where $\tilde{A} = 20$ (black), where half of the ^4He is consumed (blue) and where $|\delta_{56}| = 10^{-3}$ (green), calculated with the NSE4 (dotted lines), NSE5 (dashed lines) and NSE6 (solid lines) isotope lists, from the results calculated with the NSE7 isotope list, for He with $T_{0,9} = 0.2$, as a function of the upstream density.

Figure 21. The Coulomb correction terms to the EOS are only important at high densities, and they change at most the $\tilde{A} = 20$ scale by $\approx 15\%$. The Coulomb correction terms to the NSE have an effect at high densities, where they can decrease the length scales by up to a factor of 2, as they increase the reaction rates. Uncertainty in the reaction rates can be at the same magnitude or even higher, making the length scales uncertain to a factor of a few. However, a detailed study of the sensitivity to uncertain reaction rates is beyond the scope of this paper.

5.2.4 Comparing the detonation wave structure in He to Khokhlov (1989)

Khokhlov (1989) calculated the CJ detonation wave structure for He, an upstream temperature of (probably) $T_{0,9} = 0.2$ and a few values of the upstream density in the range of $[\text{few} \times 10^5, \text{few} \times 10^9] \text{ g/cm}^3$. The value of D_{CJ} used by Khokhlov (1989) is probably different from our value of $D_{\text{CJ}} \approx 1.4906 \times 10^4 \text{ km/s}$, calculated with the input physics of Khokhlov (1989), due to the erroneous EOS used by Khokhlov (1989). We compare in Figure 24 the structure of the CJ detonation. It is apparent from the upper panel of Figure 24 that the NSE state is different in the two calculations. This difference is similar in magnitude to the one we found in Section 4.2.2, suggesting that it is due to the erroneous EOS used by Khokhlov (1989). Note, however, that in Table 11 we consistently get for CJ detonations a higher T_{CJ} and lower $q_{01,\text{CJ}}$ than the results of Khokhlov (1988), which is not the case for the NSE state in Figure 24. This could suggest that the results of Khokhlov (1988) are inconsistent with the results of Khokhlov (1989). The abundance of the isotopes shown in the bottom panel of Figure 24 are similar in the two calculations.

We next compare in Figure 25 our results with the input physics of Khokhlov (1989) (solid lines) to the results with our default input physics (dotted lines). The synthesis of heavy elements is significantly faster in the default case (compare the profile of \tilde{A}). The inclusion of the Coulomb correction term for the NSE (dashed lines) changes the profiles by $\lesssim 10\%$ (see also Figure 21). The main discrepancy is because of the isotope list used by Khokhlov (1989). We verified that the default results are reproduced by adding the missing isotopes from NSE7 with $Z \leq 14$ and from the α -ext lists to the list used by Khokhlov (1989), which increases the number of isotopes to 161. In fact, the results from NSE4 deviate by less than 30% for this upstream density (see Figure 23), which shows that with 137 isotopes (although somewhat different than the 114 used by Khokhlov (1989)) much better results could have been obtained.

6 AN APPROXIMATE CONDITION FOR CJ DETONATIONS

In Section 5.1.2, we found that CO detonations are pathological for all upstream densities values, as far as our numerical accuracy allowed us to test this. In Section 5.2.2, we claimed, without justifying it, that He detonations are of the CJ type. In this section, we show that He detonations are indeed of the CJ type, and we further provide an approximate condition, independent of reaction rates, that allows to estimate whether arbitrary upstream values (including composition) will support a detonation of the CJ type.

For each upstream value, we can calculate the \tilde{Y}_0 of the initial conditions and the \tilde{Y}_{CJ} of the NSE state for a CJ detonation. The assumption we make now is that along the detonation wave, \tilde{Y} is monotonic between \tilde{Y}_0 and \tilde{Y}_{CJ} . This behaviour holds for CO and He (see, for example, Figures 7 and 18), but certainly breaks down when $\tilde{Y}_0 \approx \tilde{Y}_{\text{CJ}}$. Our analysis is, therefore, approximate in the sense that it applies only when \tilde{Y}_0 and \tilde{Y}_{CJ} are significantly different. Under our assumption there are two cases – either \tilde{Y} is monotonically decreasing (as in CO detonations) or it is monotonically increasing (as in He detonations). We can, therefore, inspect the solution of the CJ detonation wave near the NSE state by solving for NSQE with \tilde{Y} slightly larger or smaller than \tilde{Y}_{CJ} . It should be realised that for NSQE, the value of \tilde{Y} completely defines the state of the plasma for a given D_{CJ} . This allows us to calculate $\delta q = q(\tilde{Y}_{\text{CJ}}) - q(\tilde{Y}_{\text{CJ}} + \delta\tilde{Y})$

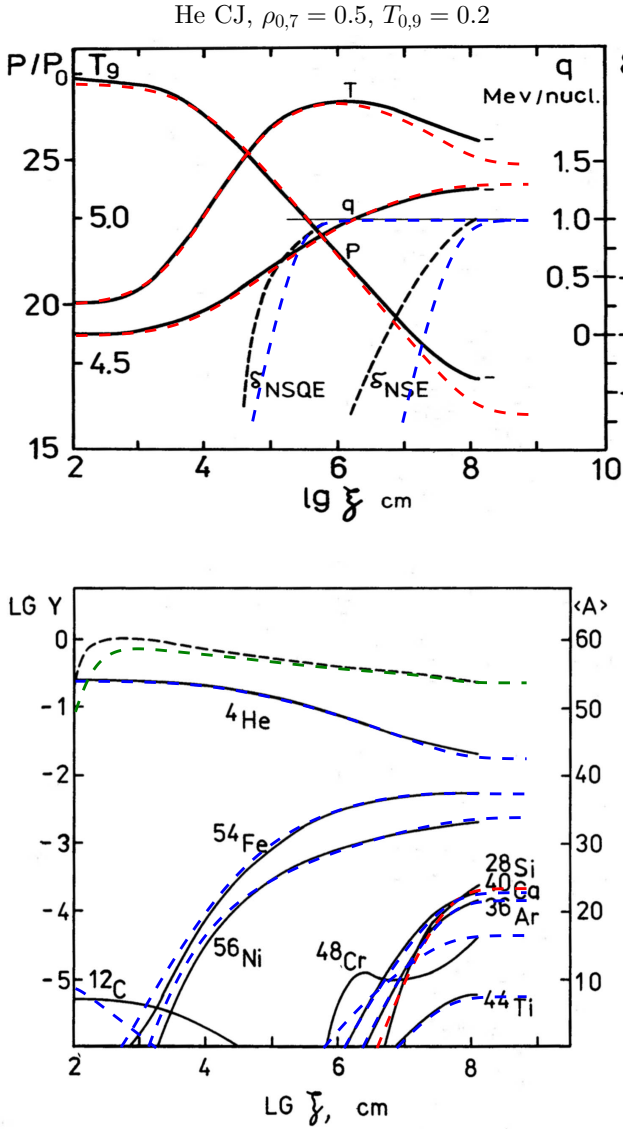


Figure 24. Figures 10 and 11 of Khokhlov (1989). The structure of a CJ detonation wave for He, $T_{0,9} = 0.2$, $\rho_{0,7} = 0.5$ and $D = 1.233 \times 10^4$ km/s, as a function of the distance behind the shock. Black lines are the results of Khokhlov (1989), while the coloured lines are our results with the input physics of Khokhlov (1989). The value of D_{CJ} used by Khokhlov (1989) is probably different from our value of $D_{\text{CJ}} \approx 1.4906 \times 10^4$ km/s due to the erroneous EOS used by Khokhlov (1989). The green dashed line in the bottom panel is \bar{A} .

near the NSE state. In the case that $\delta q > 0$ (< 0), the energy release increases (decreases) towards the NSE state, which is the signature of a CJ (pathological) detonation. For all the cases that we examined, we find that

$$\left(\frac{dq}{dY}\right)_{\text{CJ,NSE}} > 0, \quad (20)$$

but we are unable to provide a proof for it. If Equation (20) always holds, then we get the following simple condition for a CJ detonation:

$$\tilde{Y}_0 < \tilde{Y}_{\text{CJ}}. \quad (21)$$

To test the approximate condition (21), we calculate D_{CJ} and

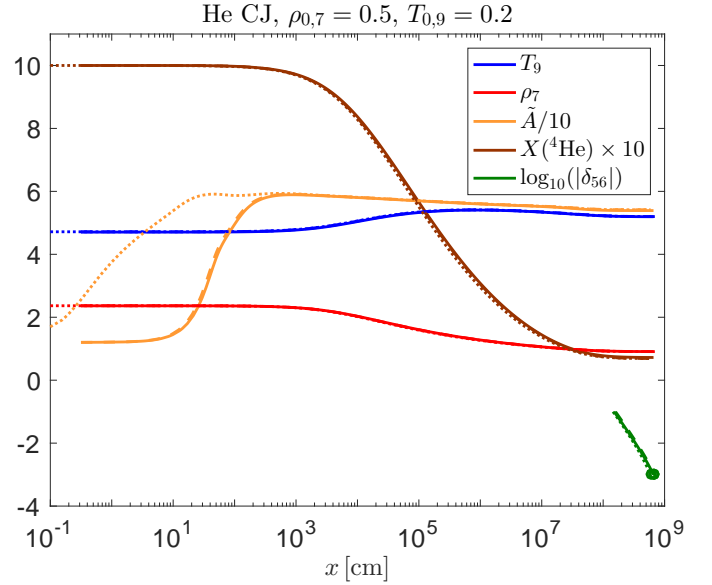


Figure 25. The structure of a CJ detonation wave for He, $T_{0,9} = 0.2$ and $\rho_{0,7} = 0.5$ as a function of the distance behind the shock. We show the temperature (blue), density (red), \bar{A} (orange), ${}^4\text{He}$ mass fraction (brown) and δ_{56} (green). The solid lines are the results with the input physics of Khokhlov (1989), the dashed lines are with the addition of Coulomb correction terms to the NSE, and the dotted lines are the results with the default input physics. Green points mark the location where $|\delta_{56}| = 10^{-3}$.

D_* for $\rho_{0,7} = 10$, $T_{0,9} = 0.2$ and for a ${}^4\text{He}$, ${}^{12}\text{C}$, ${}^{16}\text{O}$ mixture with $X({}^{12}\text{C}) = X({}^{16}\text{O})$ (and varying amounts of ${}^4\text{He}$). The results are presented in Figure 26. For $X({}^4\text{He}) \lesssim 0.81$, we are able to resolve $D_* > D_{\text{CJ}}$. However, the deviation between D_* and D_{CJ} decreases abruptly with higher mass fractions of ${}^4\text{He}$, which our numerical accuracy does not allow us to resolve. The abrupt decrease suggests that for $X({}^4\text{He}) \gtrsim 0.81$ the detonation is of the CJ type, which supports the claim that He detonations are of the CJ type. Furthermore, the approximate condition (21) predicts the transition to happen at $X({}^4\text{He}) \approx 0.85$, which is in excellent agreement with the detailed calculations. Similar results were obtained for different values of ρ_0 as well. We, therefore, conclude that the approximate condition of Equation (21) is valid.

7 THE EFFECT OF WEAK REACTION ON THE RESULTS

In this section, we justify the assumption of the absence of weak reactions throughout the paper. Physically, since neutrinos are lost from the system, energy constantly leaves the system and a steady-state solution cannot be obtained. However, this effect can be smaller than the numerical accuracy of the integration, allowing, for example, the condition $\delta_{\text{max}} = 10^{-3}$ to be fulfilled. We test the effects of weak reactions separately for thermal neutrino emission (NEU module of MESA) and for weak nuclear reactions (WEAKLIB module of MESA). We calculate overdriven detonations for the cases in Tables 2 with $D = D_* + 10$ km/s (and for the cases in Table 8 with $D = D_{\text{CJ}} + 10$ km/s) with and without weak reactions. For CO, the deviation in the Carbon burning length scale is completely negligible. The deviation in the position of the ${}^{28}\text{Si}$ maximum is not negligible only for $\rho_0 = 10^6$ g/cm 3 (where there is enough time for the neutrino losses to be significant); however, in

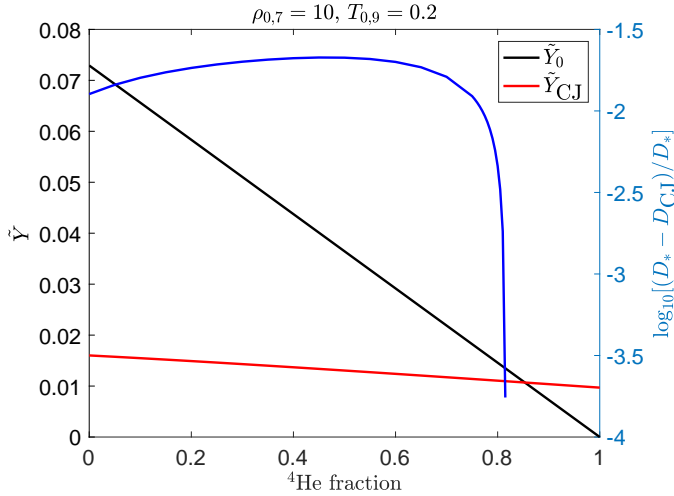


Figure 26. \tilde{Y}_0 (black) and \tilde{Y}_{CJ} (red) for $\rho_{0,7} = 10$, $T_{0,9} = 0.2$, and a ${}^4\text{He}$, ${}^{12}\text{C}$, ${}^{16}\text{O}$ mixture with $X({}^{12}\text{C}) = X({}^{16}\text{O})$ as a function of $X({}^4\text{He})$. The right y-axis shows the deviation between D_{CJ} and D_* (blue). For $X({}^4\text{He}) \lesssim 0.81$ we are able to resolve $D_* > D_{CJ}$. However, the deviation between D_* and D_{CJ} decreases abruptly with higher mass fractions of ${}^4\text{He}$, which our numerical accuracy does not allow us to resolve. The abrupt decrease suggests that for $X({}^4\text{He}) \gtrsim 0.81$ the detonation is of the CJ type, which supports the claim that He detonations are of the CJ type. Furthermore, the approximate condition of Equation (21) predicts the transition to happen at $X({}^4\text{He}) \approx 0.85$, which is in excellent agreement with the detailed calculations.

this case the maximum position is much larger than the dynamical scale. For He, the deviation in the positions where $\tilde{A} = 20$ and where half of the ${}^4\text{He}$ is consumed is negligible. We further compare the position in which the density profile deviates by more than 1% from the default case. It is either that the condition $\delta_{\max} = 10^{-3}$ is fulfilled and there is no deviation larger than 1%, or that the deviation happens at scales comparable to (or much larger than) the dynamical scale. We, therefore, conclude that the assumption of absence of weak reactions is justified.

8 SUMMARY

In this work, we revisited the problem of thermonuclear detonation waves. We constructed lists of isotopes that allow the calculation of a thermonuclear detonation wave (Section 3.2) with some prescribed accuracy. For all isotopes, we used the most updated (measured) values of their mass and ground-state spin, and we provide fit parameters to the nuclear partition functions for all isotopes (Section 3.1). We examined in detail the EOS and constructed an EOS with an uncertainty in the range of one percent (Section 3.3). For this level of uncertainty, the nuclear level excitations (Section 3.3.1) and the ion-ion interaction terms (Section 3.4) must be included. It seems possible to construct an EOS with a $\sim 0.1\%$ level of uncertainty (Potekhin & Chabrier 2010), but this accuracy is not required for current applications of supernovae. The EOS we constructed allows us to calculate CJ detonations with a degree of uncertainty in the percent level. We further provide the parameters of CJ detonations for initial compositions of CO (Section 4.1) and He (Section 4.2) over a wide range of upstream plasma conditions that are relevant for supernovae. By comparing to previous works, we demonstrate that this is the first time that such a level of accuracy

is obtained for the calculation of CJ detonations. Our results have a numerical accuracy of $\sim 0.1\%$, which allows an efficient benchmarking for future studies. We provide all the relevant information needed to fully reproduce our results.

Our calculation of the structure of a detonation wave for both CO (Section 5.1) and He (Section 5.2) over a wide range of upstream plasma conditions, demonstrates that we are able to perform such a calculation to a numerical accuracy of $\sim 0.1\%$. Our determination of the pathological detonation speed for CO, as well as the NSE state for these detonations, is with a degree of uncertainty in the percent level. By comparing to previous works, we demonstrate that this is the first time that such a degree of accuracy have been reached. The uncertainty of different physical scales within the detonation waves are uncertain to a factor of a few, because the uncertainty is dominated by uncertain reaction rates. A detailed study of this uncertainty is beyond the scope of this work, but we demonstrate that modern reaction-rate libraries can have erroneous rates by up to a factor of 2 (Section 3.2). The calculation of the physical scales is done with a numerical accuracy that is in the percent level, except for the location of the sonic point for pathological detonations, which is calculated with a numerical accuracy of a few tens of percent.

Besides providing accurate results and highlighting a few errors and inaccuracies in previous works, we report here a few new insights into the structure of thermonuclear detonation waves. We show that CO detonations are pathological for all upstream density values, as far as our numerical accuracy allowed us to test this (Section 5.1.2). This is different from previous studies, which concluded that for low upstream densities CO detonations are of the CJ type. These claims were probably due to low numerical accuracy. We further provide an approximate condition, independent of reaction rates, that allows to estimate whether arbitrary upstream values (including composition) will support a detonation of the CJ type (Section 6). Using this argument, we were able to show that CO detonations are pathological for all upstream densities and to verify that He detonations are of the CJ type, as was previously claimed for He. We also show that for CO detonations the location of the sonic point changes position in a discontinuous manner from $x \sim 100$ cm to $x \sim 10^4$ cm around $\rho_{0,7} \approx 2.7$.

Our analysis of the reactions that control the approach to NSE, which determines the length scale of this stage, revealed that at high densities, the reaction ${}^{11}\text{B} + p \leftrightarrow 3{}^4\text{He}$ plays a significant role, which was previously unknown. This will help to focus the effort of improving reaction-rate measurements.

The implications of the various improvements introduced in this work to supernova modelling will be studied in the future. Nevertheless, we demonstrate here that the study of thermonuclear detonation waves is a highly efficient means of exposing numerical bugs, as is evident from the dozens of numerical bugs we found in the *Helmholtz* EOS (Appendix B) and in the MESA code (Appendix C), some of them quite severe.

ACKNOWLEDGEMENTS

We thank Boaz Katz, Eli Waxman, Dean Townsley and Frank Timmes for useful discussions. DK is supported by the Israel Atomic Energy Commission - The Council for Higher Education - Pazi Foundation - and by a research grant from The Abramson Family Center for Young Scientists.

REFERENCES

- Abe, R. 1959, *Progress of Theoretical Physics*, 21, 475
- Bodansky, D., Clayton, D. D., & Fowler, W. A. 1968, *ApJS*, 16, 299
- Bruenn, S. W. 1971, *ApJ*, 168, 203
- Bruenn, S. W. 1971, *ApJS*, 207, 283
- Bruenn, S. W., & Marroquin, A. 1975, *ApJ*, 195, 567
- Calder, A. C., Townsley, D. M., Seitzzahl, I. R., et al. 2007, *ApJ*, 656, 313
- Cameron, A. G. W., & Elkin, R. M. 1965, *Canadian Journal of Physics*, 43, 1288
- Caughlan, G. R., & Fowler, W. A. 1988, *Atomic Data and Nuclear Data Tables*, 40, 283
- Chabrier, G., & Potekhin, A. Y. 1998, *Phys. Rev. E*, 58, 4941
- Clifford, F. E., & Tayler, R. J. 1965, *Mem. RAS*, 69, 21
- Cox, J. P., & Giuli, R. T. 1968, *Principles of stellar structure*, by J.P. Cox and R. T. Giuli. New York: Gordon and Breach, 1968
- Cyburt, R. H., Amthor, A. M., Ferguson, R., et al. 2010, *ApJS*, 189, 240
- Dewitt, H. E., Graboske, H. C., & Cooper, M. S. 1973, *ApJ*, 181, 439
- Domínguez, I., & Khokhlov, A. 2011, *ApJ*, 730, 87
- Döring, W. 1943, *Ann. Phys.*, 435, 421
- Dunkley, S. D., Sharpe, G. J., & Falle, S. A. E. G. 2013, *MNRAS*, 431, 3429
- Dursi, L. J., & Timmes, F. X. 2006, *ApJ*, 641, 1071
- Fickett, W., & Davis, C. 1979, *Los Alamos Series in Basic and Applied Sciences*, Berkeley: University of California Press, 1979
- Fields, C. E., Timmes, F. X., Farmer, R., et al. 2017, *arXiv:1712.06057*
- Fowler, W. A., & Hoyle, F. 1964, *ApJS*, 9, 201
- Fryxell, B., Olson, K., Ricker, P., et al. 2000, *ApJS*, 131, 273
- Gamezo, V. N., Wheeler, J. C., Khokhlov, A. M., & Oran, E. S. 1999, *ApJ*, 512, 827
- Hansen, J. P., Torrie, G. M., & Vieillefosse, P. 1977, *Phys. Rev. A*, 16, 2153
- Hoyle, F., & Fowler, W. A. 1960, *ApJ*, 132, 565
- Ichimaru, S., Iyetomi, H., & Tanaka, S. 1987, *Phys. Rep.*, 149, 91
- Imshennik, V. S., & Khokhlov, A. M. 1984, *Soviet Astronomy Letters*, 10, 262
- Jancovici, B. 1962, *Il Nuovo Cimento*, 25, 428
- Khokhlov, A. M. 1984, *Soviet Astronomy Letters*, 10, 123
- Khokhlov, A. M., & Ergma, E. V. 1985, *Astrofizika*, 23, 605
- Khokhlov, A. M. 1988, *Ap&SS*, 149, 91
- Khokhlov, A. M. 1989, *MNRAS*, 239, 785
- Kushnir, D., Katz, B., Dong, S., Livne, E., & Fernández, R. 2013, *ApJ*, 778, L37
- Kushnir, D., & Waxman, E. 2018, *arXiv:1805.08788*
- Landau, L. D., & Lifshitz, E. M. 1980, *Course of theoretical physics*, Pergamon International Library of Science, Technology, Engineering and Social Studies, Oxford: Pergamon Press, 1980/c1980, 3rd rev. and enlarg. ed.,
- Mattauch, J. H. E., Thiele, W., & Wapstra, A. H. 1965, *Nuclear Phys. A*, 67, 1
- Mazurek, T. 1973a, Ph.D. Thesis,
- Mazurek, T. J. 1973b, *Ap&SS*, 23, 365
- Nadyozhin, D. K. 1974, *Nauchnye Informatsii*, 32, 3
- Nadyozhin, D. K., & Yudin, A. V. 2005, *Astronomy Letters*, 31, 271
- Noël, C., Busegnies, Y., Papalexandris, M. V., Deledicque, V., & El Mesoudi, A. 2007, *A&A*, 470, 653
- Paxton, B., Bildsten, L., Dotter, A., et al. 2011, *ApJS*, 192, 3
- Paxton, B., Cantiello, M., Arras, P., et al. 2013, *ApJS*, 208, 4
- Paxton, B., Marchant, P., Schwab, J., et al. 2015, *ApJS*, 220, 15
- Potekhin, A. Y., & Chabrier, G. 2000, *Phys. Rev. E*, 62, 8554
- Potekhin, A. Y., Chabrier, G., & Rogers, F. J. 2009a, *Phys. Rev. E*, 79, 016411
- Potekhin, A. Y., Chabrier, G., Chugunov, A. I., Dewitt, H. E., & Rogers, F. J. 2009b, *Phys. Rev. E*, 80, 047401
- Potekhin, A. Y., & Chabrier, G. 2010, *Contributions to Plasma Physics*, 50, 82
- Sallaska, A. L., Iliadis, C., Champagne, A. E., et al. 2013, *ApJS*, 207, 18
- Seitzzahl, I. R., & Townsley, D. M. 2017, *arXiv:1704.00415*
- Shapiro, S. L., & Teukolsky, S. A. 1983, *Research supported by the National*

- Science Foundation. New York, Wiley-Interscience, 1983, 663 p.
- Sharpe, G. J. 1999, *MNRAS*, 310, 1039
- Shen, K. J., Kasen, D., Miles, B. J., & Townsley, D. M. 2017, *arXiv:1706.01898*
- Stolzmann, W., & Blöcker, T. 2000, *A&A*, 361, 1152
- Timmes, F. X. 1999, *ApJS*, 124, 241
- Timmes, F. X., & Arnett, D. 1999, *ApJS*, 125, 277
- Timmes, F. X., & Niemeyer, J. C. 2000, *ApJ*, 537, 993
- Timmes, F. X., & Swesty, F. D. 2000, *ApJS*, 126, 501
- Townsley, D. M., Moore, K., & Bildsten, L. 2012, *ApJ*, 755, 4
- Townsley, D. M., Miles, B. J., Timmes, F. X., Calder, A. C., & Brown, E. F. 2016, *ApJS*, 225, 3
- von Neumann, J. 1947, *Los Alamos Sci. Lab. Tech. Series*, Vol. 7
- Woolsey, S. E., Fowler, W. A., Holmes, J. A., & Zimmerman, B. A. 1978, *Atomic Data and Nuclear Data Tables*, 22, 371
- Yakovlev, D. G., & Shalybkov, D. A. 1989, *Astrophysics and Space Physics Reviews*, 7, 311
- Zel'Dovich, Y.B. 1940, *Sov. J. Exp. Theor. Phys*, 10, 542

APPENDIX A: DIFFERENCES BETWEEN WINVNV_2.0.DAT AND ENSDF

For some isotopes, the values of the nuclear masses, m_i , included in WINVNV_2.0.DAT differ from the most updated values given in the ENSDF database, \bar{m}_i . The list of isotopes for which m_i and \bar{m}_i differ is given in Table A1, together with their mass values. For some isotopes, the values of $J_{i,0}$ included in WINVNV_2.0.DAT differ from the most updated values given in the ENSDF database, $\bar{J}_{i,0}$. The list of isotopes for which $J_{i,0}$ and $\bar{J}_{i,0}$ differ is given in Table A2, together with their spin values.

APPENDIX B: NUMERICAL BUGS IN HELMHOLTZ EOS

We here report on the numerical bugs that we found in the *Helmholtz* EOS that is distributed together with the MESA version r7624.

(i) file `helm_coulomb2.dek`. This file implements the treatment of *Yakovlev & Shalybkov* (1989) for the ion-ion interaction term, which should be obsolete (see discussion in Section 3.4).

(a) line 39 – wrong second derivative: $dsddz = y * dxniddz \rightarrow dsddz = y * dxniddz + forthpi * dxnidd$

(b) line 42 – wrong second derivative: $dsdtz = y * dxnidtz \rightarrow dsdtz = y * dxnidtz + forthpi * dxnidt$

(c) line 44 – wrong second derivative: $dsdaz = y * dxnidaz \rightarrow dsdaz = y * dxnidaz + forthpi * dxnida$

(d) line 45 – wrong second derivative: $dsdzz = y * dxnidzz + 2.0d0 * forthpi * dxnidz \rightarrow dsdzz = y * dxnidzz + forthpi * dxnidz$

(e) line 91 – wrong second derivative: $+ (2.0d0 * z * daeledt + 2.0d0 * eplasz * tempinv) * tempinv \rightarrow + (-2.0d0 * z * daeledt + 2.0d0 * eplasz * tempinv) * tempinv$

(f) line 259 – wrong second derivative: $dscoulda = x * dplaszda * dplaszdd + ww * dplaszgda - x * ytot1 * dplaszdd \rightarrow dscoulda = x * dplaszda * dplaszdd + ww * dplaszgda - ww * ytot1 * dplaszdd$

(g) line 262 – wrong second derivative: $dscouldta = x * dplaszda * dplaszdt + ww * dplaszgda - x * ytot1 * dplaszdt \rightarrow dscouldta = x * dplaszda * dplaszdt + ww * dplaszgda - ww * ytot1 * dplaszdt$

(h) lines 264-265 – wrong second derivative: $dscouldaa = x * dplaszda * dplaszda + ww * dplaszgda - x * ytot1 * dplaszda - ww * dplaszda * ytot1 + 2.0d0 * scoul * ytot1 * ytot1 \rightarrow$

Table A1. The list of isotopes for which the values of the nuclear masses, m_i , included in WIN-VNV_2.0.DAT differ from the most updated values given in the ENSDF database, \tilde{m}_i .

Isotope	m_i	\tilde{m}_i	Isotope	m_i	\tilde{m}_i	Isotope	m_i	\tilde{m}_i
¹³ Be	33.208	33.659	¹⁹ O	3.334	3.333	²² O	9.282	9.283
¹⁵ F	16.813	16.567	²³ F	3.310	3.285	²⁴ F	7.560	7.545
²⁵ F	11.364	11.334	²⁶ F	18.665	18.649	²⁷ F	24.630	25.450
²⁵ Ne	-2.060	-2.036	²⁶ Ne	0.479	0.481	²⁷ Ne	7.036	7.051
²⁸ Ne	11.292	11.300	³⁰ Ne	23.040	23.280	³¹ Ne	30.820	31.182
³² Ne	37.278	36.999	³⁴ Ne	53.121	52.842	¹⁹ Na	12.928	12.929
²⁹ Na	2.670	2.680	³⁰ Na	8.374	8.475	³¹ Na	12.540	12.246
³² Na	18.810	18.640	³³ Na	24.889	23.780	³⁴ Na	32.761	31.680
³⁵ Na	39.582	38.231	³⁶ Na	47.953	46.303	³⁷ Na	55.275	53.534
²⁰ Mg	17.559	17.478	²¹ Mg	10.913	10.904	³⁰ Mg	-8.892	-8.884
³¹ Mg	-3.190	-3.122	³² Mg	-0.912	-0.829	³³ Mg	4.947	4.962
³⁴ Mg	8.560	8.323	³⁷ Mg	29.249	28.211	³⁸ Mg	34.996	34.074
³⁹ Mg	43.568	42.275	⁴⁰ Mg	50.235	48.350	²² Al	18.183	18.201
²⁹ Al	-18.215	-18.208	³⁰ Al	-15.872	-15.865	³¹ Al	-14.955	-14.951
³² Al	-11.062	-11.099	³³ Al	-8.437	-8.497	³⁴ Al	-3.047	-3.000
³⁵ Al	-0.220	-0.224	³⁹ Al	21.396	20.650	⁴⁰ Al	29.295	27.590
⁴¹ Al	35.704	33.420	⁴² Al	43.678	40.100	⁴³ Al	48.428	47.020
²³ Si	23.772	23.697	²⁴ Si	10.755	10.745	³⁵ Si	-14.360	-14.391
³⁶ Si	-12.418	-12.436	³⁷ Si	-6.594	-6.571	⁴² Si	18.434	16.470
⁴³ Si	26.697	23.101	⁴⁴ Si	32.844	28.513	²⁷ P	-0.716	-0.722
²⁸ P	-7.149	-7.148	³⁸ P	-14.643	-14.622	³⁹ P	-12.795	-12.775
⁴⁰ P	-8.074	-8.114	²⁹ S	-3.157	-3.156	³⁰ S	-14.062	-14.059
⁴⁰ S	-22.930	-22.838	⁴¹ S	-19.089	-19.009	⁴² S	-17.678	-17.638
⁴³ S	-12.070	-12.195	⁴⁴ S	-9.100	-9.204	³¹ Cl	-7.066	-7.035
⁴² Cl	-24.913	-24.832	⁴³ Cl	-24.408	-24.159	⁴⁴ Cl	-20.605	-20.384
⁴⁵ Cl	-18.360	-18.262	⁴⁶ Cl	-13.810	-13.859	⁴⁶ Ar	-29.729	-29.773
⁴⁷ Ar	-25.210	-25.366	⁴⁸ Ar	-23.716	-23.281	⁴⁹ Ar	-18.146	-17.190
⁵⁰ K	-25.736	-25.728	⁵¹ K	-22.002	-22.516	⁵¹ Ca	-35.873	-36.332
⁵² Ca	-32.509	-34.266	⁵³ Ca	-27.898	-29.388	⁵⁴ Ca	-23.893	-25.161
⁵² Sc	-40.357	-40.443	⁵³ Sc	-37.623	-38.907	⁵⁴ Sc	-34.219	-33.891
⁵⁵ Sc	-29.581	-30.159	⁵⁶ Sc	-25.271	-24.852	⁴¹ Ti	-15.090	-15.697
⁵⁴ Ti	-45.594	-45.622	⁵⁶ Ti	-38.937	-39.320	⁵⁷ Ti	-33.544	-33.916
⁵⁸ Ti	-30.767	-31.110	⁴² V	-8.169	-7.620	⁴³ V	-17.814	-17.916
⁴⁵ V	-31.880	-31.886	⁵⁵ V	-49.153	-49.147	⁵⁶ V	-46.080	-46.155
⁵⁷ V	-44.189	-44.413	⁵⁸ V	-40.209	-40.402	⁴⁴ Cr	-13.461	-13.360
⁴⁵ Cr	-19.436	-19.515	⁴⁷ Cr	-34.559	-34.563	⁵⁸ Cr	-51.835	-51.992
⁵⁹ Cr	-47.891	-48.086	⁴⁶ Mn	-12.512	-12.570	⁴⁷ Mn	-22.661	-22.566
⁴⁸ Mn	-29.323	-29.296	⁴⁹ Mn	-37.615	-37.621	⁴⁸ Fe	-18.160	-18.000
⁴⁹ Fe	-24.766	-24.751	⁵⁰ Fe	-34.489	-34.476	⁵¹ Fe	-40.221	-40.203
⁵⁰ Co	-17.832	-17.630	⁵¹ Co	-27.542	-27.342	⁵² Co	-33.916	-34.361
⁶² Co	-61.431	-61.424	⁶³ Co	-61.840	-61.851	⁵² Ni	-22.654	-22.330
⁵³ Ni	-29.851	-29.631	⁵⁴ Ni	-39.223	-39.278	⁵⁴ Cu	-22.062	-21.410
⁵⁵ Cu	-31.994	-31.635	⁵⁶ Cu	-38.694	-38.643	⁵⁶ Zn	-26.137	-25.390
⁵⁷ Zn	-32.945	-32.550	⁶¹ Zn	-56.343	-56.349	⁵⁹ Ga	-34.087	-33.760
⁶⁰ Ga	-40.004	-39.590	⁶¹ Ga	-47.088	-47.135	⁶⁰ Ge	-27.858	-27.090
⁶¹ Ge	-34.065	-33.360	⁶² Ge	-42.377	-41.740	⁶³ As	-33.687	-33.500
⁶⁴ As	-39.518	-39.532	⁶⁹ As	-63.086	-63.112	⁸⁰ As	-72.172	-72.214
⁶⁴ Se	-27.504	-26.700	⁶⁵ Se	-33.325	-33.020	⁶⁶ Se	-41.832	-41.660
⁶⁹ Se	-56.301	-56.435	⁶⁹ Br	-46.265	-46.260			

dscouldaa = x*dplsgda*dplsgda + ww*dplsgdaa - 2d0*ww*dplsgda*ytot1 + 2.0d0*scol*ytot1*ytot1

(i) line 393 – the Coulomb correction term (pressure, energy and entropy) is limited to be some fraction of the gas term. We suggest to limit only the pressure and the energy, since the Coulomb entropy contribution can be quite significant even when the correction terms of the pressure and of the energy are a few percent: coulfrac = max(pcoulfrac, ecoulfrac, scoulfrac) → coulfrac = max(pcoulfrac, ecoulfrac)

(ii) file helm_electron_positron.dek

(a) line 421 – wrong second derivative: dpepdda = (zz*dindd + ww)*dindda → dpepdda = zz*dindd*dinda + ww*dindda

(b) line 422 – wrong second derivative: dpepddz = (zz*dindd + ww)*dinddz → dpepddz = zz*dindd*dindz + ww*dinddz

(c) line 426 – wrong second derivative: dpepdaa = (zz*dinda + ww)*dindaa → dpepdaa = zz*dinda**2 + ww*dindaa

(d) line 427 – wrong second derivative: dpepdaz = (zz*dinda + ww)*dindaz → dpepdaz = zz*dinda*dindz + ww*dindaz

Table A2. The list of isotopes for which the values of $J_{i,0}$ included in WIN-VNV_2.0.DAT differ from the most updated values given in the ENSDF database, $\tilde{J}_{i,0}$.

Isotope	$J_{i,0}$	$\tilde{J}_{i,0}$	Isotope	$J_{i,0}$	$\tilde{J}_{i,0}$
¹³ Be	3/2	1/2	¹⁸ N	2	1
²¹ O	1/2	5/2	²³ O	3/2	1/2
¹⁴ F	0	2	²³ F	3/2	5/2
²⁴ F	0	3	²⁵ F	1/2	5/2
²⁶ F	2	1	²⁷ F	3/2	5/2
²⁹ Ne	1/2	3/2	¹⁹ Na	3/2	5/2
³¹ Na	5/2	3/2	³² Na	0	3
²¹ Mg	3/2	5/2	³¹ Mg	3/2	1/2
³³ Mg	5/2	3/2	³⁵ Mg	3/2	5/2
²² Al	3	4	³¹ Al	3/2	5/2
³³ Al	3/2	5/2	³⁴ Al	2	4
³⁵ Si	5/2	7/2	³⁷ Si	3/2	5/2
³⁶ P	2	4	³⁸ P	2	0
³⁹ S	3/2	7/2	⁴³ S	7/2	3/2
⁴⁴ Cl	4	2	⁴⁵ Cl	3/2	1/2
⁴⁶ Cl	0	2	⁴³ Ar	3/2	5/2
⁴⁵ Ar	1/2	5/2	⁴⁹ K	3/2	1/2
⁵¹ K	1/2	3/2	⁵³ Ca	3/2	1/2
⁵⁴ Sc	1	3	⁵⁶ Sc	3	1
⁵⁷ Ti	3/2	5/2	⁴⁴ V	3	2
⁵⁶ V	2	1	⁵⁷ V	3/2	7/2
⁵⁸ V	2	1	⁴⁵ Cr	5/2	7/2
⁵⁹ Cr	3/2	1/2	⁵⁸ Mn	3	1
⁵⁹ Mn	3/2	5/2	⁶⁰ Mn	3	1
⁵⁰ Co	4	6	⁵² Co	1	6
⁷¹ Ni	1/2	9/2	⁵⁵ Cu	1/2	3/2
⁵⁶ Cu	3	4	⁷⁰ Cu	1	6
⁷² Cu	1	2	⁶⁰ Ga	1	2
⁶³ Ge	1/2	3/2	⁶⁶ As	2	0
⁷⁰ As	0	4	⁶⁵ Se	1/2	3/2
⁶⁹ Se	3/2	1/2	⁷¹ Se	3/2	5/2
⁶⁹ Br	9/2	5/2	⁷⁰ Br	5	0
⁷² Br	3	1	⁸⁶ Br	2	1
⁷¹ Kr	9/2	5/2	⁷³ Kr	5/2	3/2

(e) lines 451-453 – wrong second derivative: dsepd_{aa} = -df_{ddt}*dinda*dinda*ye - df_{dt}*(dinda*ye - dinda*ye*ytot1 + dinda*dindda) - df_t*dinddaa → dsepd_{aa} = -df_{ddt}*dinda*dinda*ye - df_{dt}*(dinda*ye - 2d0*dinda*ye*ytot1) - 2d0*df_t*ytot1

(f) lines 454-456 – wrong second derivative: dsepd_{az} = -df_{ddt}*dindz*dinda*ye - df_{dt}*(dindaz*ye + dinda*ytot1 + dindz*dindda) - df_t*dinddaz → dsepd_{az} = -df_{ddt}*dindz*dinda*ye - df_{dt}*(dindaz*ye + dinda*ytot1 - dindz*ye) + df_t*ytot1*ytot1

(g) lines 457-458 – wrong second derivative: dsepd_{zz} = -df_{ddt}*dindz*dindz*ye - df_{dt}*(dindzz*ye + dindz*ytot1 + dindz*dinddz) → dsepd_{zz} = -df_{ddt}*dindz*dindz*ye - df_{dt}*(dindzz*ye + dindz*ytot1 + dindz*ytot1)

(h) lines 481-482 – wrong second derivative: deepdaa = 2.0d0*y*(ytot1*free - df_d*dinda) + ye*df_d*dinda + temp*dsepd_{aa} → deepdaa = 2.0d0*y*(ytot1*free - df_d*dinda) + ye*(d_d*dindaa + df_{dd}*dinda**2) + temp*dsepd_{aa}

(iii) file helm_gamma.d

(a) lines 92-93 – wrong derivative: dcs_{gasdd} = yy*((dgam1_{gasdd} - dfk)*xx* (degasdd*den - ww*dpgasdd +

x)*presinv) → dcs_{gasdd} = yy*((dgam1_{gasdd}*xx - dfk*xx* (degasdd*den - ww*dpgasdd + x)*presinv)

(b) lines 94-95 – wrong derivative: dcs_{gasdt} = yy*((dgam1_{gasdt} - dfk)*xx* (degasdt*den - ww*dpgasdt)*presinv) → dcs_{gasdt} = yy*((dgam1_{gasdt}*xx - dfk*xx* (degasdt*den - ww*dpgasdt)*presinv)

(c) lines 96-97 – wrong derivative: dcs_{gasda} = yy*((dgam1_{gasda} - dfk)*xx* (degasda*den - ww*dpgasda)*presinv) → dcs_{gasda} = yy*((dgam1_{gasda}*xx - dfk*xx* (degasda*den - ww*dpgasda)*presinv)

(d) lines 98-99 – wrong derivative: dcs_{gasdz} = yy*((dgam1_{gasdz} - dfk)*xx* (degasdz*den - ww*dpgasdz)*presinv) → dcs_{gasdz} = yy*((dgam1_{gasdz}*xx - dfk*xx* (degasdz*den - ww*dpgasdz)*presinv)

(e) lines 185-186 – wrong derivative: dcs_d = yy*((dgam1_{dd} - dfk)*xx* (denerdd*den - ww*dpresdd + x)*presinv) → dcs_d = yy*((dgam1_{dd}*xx - dfk*xx* (denerdd*den - ww*dpresdd + x)*presinv)

(f) lines 187-188 – wrong derivative: dcs_{dt} = yy*((dgam1_{dt} - dfk)*xx* (denerdt*den - ww*dpresdt)*presinv) → dcs_{dt} = yy*((dgam1_{dt}*xx - dfk*xx* (denerdt*den - ww*dpresdt)*presinv)

(g) lines 189-190 – wrong derivative: dcs_{da} = yy*((dgam1_{da} - dfk)*xx* (denerda*den - ww*dpresda)*presinv) → dcs_{da} = yy*((dgam1_{da}*xx - dfk*xx* (denerda*den - ww*dpresda)*presinv)

(h) lines 191-192 – wrong derivative: dcs_{dz} = yy*((dgam1_{dz} - dfk)*xx* (denerdz*den - ww*dpresdz)*presinv) → dcs_{dz} = yy*((dgam1_{dz}*xx - dfk*xx* (denerdz*den - ww*dpresdz)*presinv)

APPENDIX C: NUMERICAL BUGS IN MESA

We here report on the numerical bugs that we found in MESA version r7624.

(i) file mod_neu.f90.

(a) line 913 – wrong derivative: dumdd = z*rmdd + 0.656d0*c02*pow_{cr}(den,-0.454d0) → dumdd = z*rmdd + 0.656d0*c02*pow_{cr}(den,-0.344d0)

(b) The following should be added after line 1120

(1) at=pow_{cr}(den6*ye,two_thirds)

(2) tfermid= 5.9302d9/2d0 / sqrt(1.0d0+1.018d0*at) * two_thirds*at/den

(3) tfermidz= 5.9302d9/2d0 / sqrt(1.0d0+1.018d0*at) * two_thirds*at/zbar

(4) tfermida=-5.9302d9/2d0 / sqrt(1.0d0+1.018d0*at) * two_thirds*at/abar

(c) The following should be added after line 1143

(1) alfadt=0.5d0*sinpi_{cr}((temp/tfermi-tflo)/(tfhi-tflo))/(tfermi*(tfhi - tflo))

(2) alfadd=-0.5d0*sinpi_{cr}((temp/tfermi-tflo)/(tfhi-tflo))*temp/tfermi**2/(tfhi-tflo)*tfermid

(3) alfada=-0.5d0*sinpi_{cr}((temp/tfermi-tflo)/(tfhi-tflo))*temp/tfermi**2/(tfhi-tflo)*tfermida

(4) alfadz=-0.5d0*sinpi_{cr}((temp/tfermi-tflo)/(tfhi-tflo))*temp/tfermi**2/(tfhi-tflo)*tfermidz

(5) `betadt=-alfadt`

(6) `betadd=-alfadd`

(7) `betada=-alfada`

(8) `betadz=-alfadz`

(d) line 1146 – wrong derivative: $\text{sbremdt} = \text{alfa} * \text{sbd} + \text{beta} * \text{sbremdt} \rightarrow \text{sbremdt} = \text{alfa} * \text{sbd} + \text{alfadt} * \text{sb} + \text{beta} * \text{sbremdt} + \text{betadt} * \text{sbrem}$

(e) line 1147 – wrong derivative: $\text{sbremdd} = \text{alfa} * \text{sbdd} + \text{beta} * \text{sbremdd} \rightarrow \text{sbremdd} = \text{alfa} * \text{sbdd} + \text{alfadd} * \text{sb} + \text{beta} * \text{sbremdd} + \text{betadd} * \text{sbrem}$

(f) line 1148 – wrong derivative: $\text{sbremda} = \text{alfa} * \text{sbda} + \text{beta} * \text{sbremda} \rightarrow \text{sbremda} = \text{alfa} * \text{sbda} + \text{alfada} * \text{sb} + \text{beta} * \text{sbremda} + \text{betada} * \text{sbrem}$

(g) line 1149 – wrong derivative: $\text{sbremdz} = \text{alfa} * \text{sbdz} + \text{beta} * \text{sbremdz} \rightarrow \text{sbremdz} = \text{alfa} * \text{sbdz} + \text{alfadz} * \text{sb} + \text{beta} * \text{sbremdz} + \text{betadz} * \text{sbrem}$

(h) line 1219 – wrong derivative: $c01 = f1 + f2*2.0d0*nu + f3*3.0d0*nu2 \rightarrow c01 = -c00*c00*(f1 + f2*2.0d0*nu + f3*3.0d0*nu2)$

(ii) file `rates_initialize.f90`

(a) line 350 – wrong exponent for the reaction rate: `reaction_je_rho_exponents(2,ir) = 1` \rightarrow `reaction_je_rho_exponents(2,ir) = particles_in-1`

(iii) file `reaclib_eval.f90`

(a) lines 183-184 – wrong interpolation of the partition function for reverse rates (regardless of this bug, we suggest to fit the partition functions rather than interpolate, see Section 3.1): $A(j) = (\text{rates}\% \text{inverse_part}(\text{indx},i)) * (\text{rates}\% \text{inverse_part}(\text{indxp},i) / \text{rates}\% \text{inverse_part}(\text{indx},i)) \rightarrow A(j) = (\text{rates}\% \text{inverse_part}(\text{indxp},i) / \text{rates}\% \text{inverse_part}(\text{indx},i))$

(b) lines 185 – wrong interpolation of the partition function for reverse rates: $Qratio(j) = \text{pow_cr}(A(j), \text{tfac}) \rightarrow Qratio(j) = (\text{rates}\% \text{inverse_part}(\text{indx},i)) * \text{pow_cr}(A(j), \text{tfac})$

(iv) file `reaclib_support.f90`

(a) line 216 – wrong determination of the reverse rates: $\text{rates}\% \text{weight}(i) \rightarrow \text{rates}\% \text{weight}(i) / \text{rates}\% \text{weight_reverse}(i)$

APPENDIX D: CORRECTIONS TO THE EXPONENTIAL MASS FORMULA OF CAMERON & ELKIN (1965)

It seems that the exponential mass formula of [Cameron & Elkin \(1965\)](#) is erroneous and that the following correction are required:

(i) The pre-factors for E_c and E_{ex} (page 1291) should be $Z^2/A^{1/3}$ and $Z^{4/3}/A^{1/3}$ and not $Z^2/r_0A^{1/3}$ and $Z^{4/3}/r_0A^{1/3}$, respectively.

(ii) The 4th term inside the parentheses in the E_{ex} expression should include the factor r_0^3 and not r_0 .

(iii) The value for β (page 1292) should be -35.939 (given for γ by [Cameron & Elkin \(1965\)](#)).

(iv) The value for γ should be -26.587 (given for $-\beta$ by [Cameron & Elkin \(1965\)](#)).

(v) The mass excess is actually given in the ^{16}O scale (and not in the ^{12}C scale, as claimed by [Cameron & Elkin \(1965\)](#)).